Gesellschaft für Mikro- und Nanoelektronik

GMe Forum 2008

Proceedings of the Seminar at the
Vienna University Of Technology

Organized by the
Society for Micro- and Nanoelectronics
(Gesellschaft für Mikro- und Nanoelektronik – GMe)

November 13 and 14, 2008

Gesellschaft für Mikro- und Nanoelektronik

GMe Forum 2008

Proceedings of the Seminar at the
Vienna University Of Technology

Organized by the
Society for Micro- and Nanoelectronics
(Gesellschaft für Mikro- und Nanoelektronik – GMe)

November 13 and 14, 2008

Sponsored by:

Gesellschaft für Mikro- und Nanoelektronik
Bundesministerium für Verkehr, Innovation und Technologie

Program Committee:

Karl Riedling
Friedrich Schäffler
Karl Unterrainer
Michiel Vellekoop

Editor of the Proceedings:

Karl Riedling

Seminar Organization:
Claudia Benedela
Karl Riedling

Production of the Proceedings:
Karl Riedling
Claudia Benedela

ISBN: 978-3-901578-20-5

c/o Technische Universität Wien
Institut für Sensor- und Aktuatorsysteme
Gusshausstrasse 27-29/366, A-1040 Vienna

Preface

The GMe Forum continues a long series of seminars on microelectronics technology which have been organized by the Society for Micro- and Nanoelectronics (*Gesellschaft für Mikro- und Nanoelektronik* – GMe; originally "*Gesellschaft für Mikroelektronik*") since its foundation in the mid-1980s. The original seminars addressed a purely academic audience. The first GMe Forum in its current form had taken place at the Vienna University of Technology in 2001. The GMe Forum is designed to appeal to university researchers as well as to more application-oriented participants, particularly from Austrian industrial enterprises and governmental organizations. Most of the oral presentations are reviews presented by top-level speakers from international industry and research facilities. The university institutions supported by the GMe also present their results, partly as oral presentations but mostly as posters.

The Society for Micro- and Nanoelectronics is mainly financed by the Federal Ministry for Traffic, Innovation and Technology (*Bundesministerium für Verkehr, Innovation und Technologie*). Its goal is to promote micro- and nanoelectronics research and technology at Austrian universities with the main aim to stimulate the transfer of know-how to the Austrian industry and by carrying out pilot projects in the GMe supported cleanroom facilities. The relatively small budget of the GMe does not allow full sponsoring of research projects. Nevertheless, the GMe supplements other research funding sources by providing contributions for creating and maintaining state of the art laboratory infrastructure.

The main goal of the GMe in recent years was the support of the two cleanroom centers at the Vienna University of Technology and at the Johannes Kepler University Linz, respectively, where internationally competitive technological equipment has been made available to researchers, students, and industry customers.

We hope that the proceedings will promote the impact of the GMe Forum 2008, and that they will contribute to an even better international cooperation of the Austrian micro- and nanoelectronics research at academic institutions and in industry.

Univ.Prof. Dr. Karl UNTERRAINER
President of the GMe

Ao.Univ.Prof. Dr. Karl RIEDLING
Secretary General of the GMe

Forum Program

Thursday, November 13, 2008

10:00 – 10:30	Welcome, Coffee
10:30 – 11:00	Opening (E. BERTAGNOLLI, K. UNTERRAINER)
	Sensors:
11:00 – 11.45	B. JAKOBY: *Miniaturized Sensors and Sensing Systems for Liquid Media* – ***page 3***
11:45 – 12:30	H. BRÜCKL: *Magnetic Lab-on-a-Chip: Magnetic Nanoparticles for Biomedical Diagnostics* – ***page 13***
12:30 – 14:00	Lunch Break
	Nanostructures and Nanotechnology:
14:00 – 14:45	M. MÜHLBERGER: *Nanoimprint Lithography* – ***page 21***
14:45 – 15:30	T. PICHLER: *Tailoring Carbon Nanostructures: Unravelling the Electronic Properties of Low-Dimensional Quantum Solids* – ***page 29***
15:30 – 16:00	Coffee Break
16:00 – 16:45	D. GRÜTZMACHER: *Novel Device Concepts and Strategies Basing on SiGe Nanostructures* – ***page 31***
	Novel Materials and Devices:
16:45 – 17:30	P. HADLEY: *Solution-Processable Electronics* – ***page 35***
17:30 – 17:45	Break
17:45 – 18:30	L. FREY: *Engineering of Dielectric Materials for Silicon Technology* – ***page 37***
	The Society for Micro- and Nanoelectronics (GMe):
18:30 – 18:45	K. UNTERRAINER: *Presentation of the Activities of the GMe*

Friday, November 14, 2008

	Opto-Electronics and Photonics:
09:30 – 10:15	S. TASCH: *LEDs for General Purpose Lighting* – ***page 49***
10:15 – 10:45	Coffee Break
10:45 – 11:15	S. SCHARTNER: *Photonic Engineering of Intersubband Devices* – ***page 51***
	Sensors:
11:15 – 11:45	M. VELLEKOOP: *Integrated Cell Analysis Devices* – ***page 15***
	Spintronics:
11:45 – 12:15	A. BONANNI: *Origin and Control of Ferromagnetism in Magnetically Doped Nitrides. The Case of (Ga,Fe)N* – ***page 57***
12:15 – 14:00	Snacks and Poster Exhibition
	Novel Materials and Devices:
14:00 – 14:30	S. ABERMANN: *New Materials and Devices for Future Generation CMOS Technologies* – ***page 39***
14:30 – 15:00	M. BREHM: *Investigations on the Wetting Layer and the Island Nucleation in the SiGe System on Planar and Pre-Structured Si(001) Substrates* – ***page 43***

Poster Presentations

Photonics and Optoelectronics:

Nanostructures and Quantum Devices:

Novel Materials:

Sensors:

List of Participants

Dr. DI. Stephan ABERMANN
Technische Universität Wien
Institut für Festkörperelektronik
A-1040 Wien

MSc Deborah ALVARENGA
Technische Universität Wien
Leidesdorfgasse 7-4
A-1040 Wien

Dr. Aaron Maxwell ANDREWS
Technische Universität Wien
Institut für Festkörperelektronik
A-1040 Wien

DI Ibrahim ATASSI
ONKOTEC
A-1200 Wien

o.Univ.Prof. Dr. Günther BAUER
Johannes Kepler Universität Linz
Inst.f.Halbleiterphysik und
Festkörperphysik
A- 4040 Linz

Alexander BENZ
Technische Universität Wien
A-1040 Wien

o.Univ.Prof. Dr. Emmerich
BERTAGNOLLI
Technische Universität Wien
Institut für Festkörperelektronik
A-1040 Wien

Ole BETHGE
Technische Universität Wien
A-1040 Wien

Priv.-Doz. Mag. Dr. Alberta BONANNI
JKU Linz
Institut für Halbleiterphysik
A-4040 Linz

DI Moritz BREHM
JKU Linz
Institut für Halbleiterphysik
A-4040 Linz

Dr. Hubert BRÜCKL
Austrian Research Centers GmbH
Nano-Systemtechnologien
A-1220 Wien

Dipl.-Ing. Samir CERIMOVIC
Research Unit for Integrated Sensor
Systems
Austrian Academy of Sciences
A-2700 Wr. Neustadt

Dr. Gang CHEN
Linz University
Altenbergerstr. 69,
A- 4040 Linz

DI Hermann DETZ
Technische Universität Wien
ZMNS
A-1040 Wien

DI Christoph DEUTSCH
Technische Universität Wien
Gusshausstraße 27/387
A-1040 Wien

Dipl.-Phys. Daniel DIETZE
Technische Universität Wien
Institut für Photonik
A-1040 Wien

Dr. Ernest J. FANTNER
SCL-Sensor.Tech.GmbH
1220 Donau-City-Strasse 1

DI Georg FERCHER
Technische Universität Wien
Institut für Sensor- und
Aktuatorsysteme
A-1040 Wien

Prof. Dr. Lothar FREY
Fraunhofer Institut für Integrierte
Systeme
und Bauelementetechnologie FhG-IISB
D-91058 Erlangen

Dipl.-Ing. Dr. Thomas FROMHERZ
Johannes Kepler Universität Linz
Inst. f. Halbleiterphysik und Festkörperphysik
A- 4040 Linz

Dipl.-Ing. Thomas GEBHARD
Technische Universität Wien
Karolinengasse 12/35
A-1040 Wien

o.Univ.Prof. Dr. Erich GORNIK
Technische Universität Wien
Institut für Festkörperelektronik
A-1040 Wien

Prof. Dr. Detlev GRÜTZMACHER
Forschungszentrum Jülich GmbH - IBN-1
Inst. für Bio- und Nanosysteme (IBN)
Halbleiter-Nanoelektronik
D-52425 Jülich

Prof. Dr. Peter HADLEY
TU Graz
Institut für Festkörperphysik
A-8010 Graz

DI Gabriel HAIRER
Technische Universität Wien
Institut für Sensor- und Aktuatorsysteme
A-1040 Wien

DI Michael HEER
Technische Universität Wien
Institut für Festkörperelektronik
A-1040 Wien

Dipl.-Phys. Christoph HENKEL
Technische Universität Wien
Institut für Festkörperelektronik
A-1040 Wien

Dr. Kurt HINGERL
Johannes Kepler Universität Linz
ZONA (Zentrum f. Oberflächen- und Nanoanalytik)
A- 4040 Linz

Ao.Univ.Prof. Dr. Gerhard HOBLER
Technische Universität Wien
A-1040 Wien

Dipl.-Phys. Leonard HOFFMANN
Technische Universität Wien
Institut für Festkörperelektronik
A-1040 Wien

Dipl.-Ing Youn Joo HYUN
Technische Universität Wien
Institut für Festkörperelektronik
A-1040 Wien

Dr. Artur JACHIMOWICZ
Technische Universität Wien
Institut für Sensor- und Aktuatorsysteme
A-1040 Wien

Univ.Prof. Dr. Bernhard JAKOBY
JKU Linz
Institut für Mikroelektronik und Mikrosensoren
A-4040 Linz

Ao.Univ.Prof. Eugenijus KANIUSAS
Technische Universität Wien
E354
A-1040 Wien

Mario KEPLINGER

Dr. Pavel KLANG
Technische Universität Wien
A-1040 Wien

DI Christian KOLLER
Technische Universität Wien
Atominstitut-Quantenoptik
A-1020 Wien

Dipl.-Ing Stefan KOSTNER
Technische Universität Wien
Institut für Sensor und Aktuatorsysteme
A-1040 Wien

DI Dr. Günther LIENTSCHNIG
A-1020 Wien

Dipl.-Ing. Dr. Alois LUGSTEIN
Technische Universität Wien
Floragasse 7
A-1040 Wien

Wasinee MAMANEE
Technische Universität Wien
Institut für Festkörperelektronik
A-1040 Wien

DI Thomas MOLDASCHL
Technische Universität Wien
A-1040 Wien

Dr. Michael MÜHLBERGER
PROFACTOR GmbH
A-4407 Steyr-Gleink,

DI Clemens OSTERMAIER
Technische Universität Wien
Institut für Festkörperelektronik
A-1040 Wien

Dipl.-Ing. Dr. Wolfgang PARZ
Technische Universität Wien
Institut für Photonik
A-1040 Wien

DI Johannes PEHAM
Austrian Research Centers Gmbh - ARC
Molecular Diagnostics
A-2444 Seibersdorf

Dipl. Phys. ETH Oliver PFÄFFLI
Steinergasse 1/6
A-1170 Wien

Prof. Mag. Dr. Thomas PICHLER
Universität Wien
A-1090 Wien

Dr. Dionyz POGANY
Technische Universität Wien
Institut für Festkörperelektronik
A-1040 Wien

DI Gianmauro POZZOVIVO
Technische Universität Wien
Institute for Solid State Electronics
A-1040 Wien

Patrick RAUTER
Johannes Kepler Universität Linz
A- 4040 Linz

Ao.Univ.Prof. Dr. Karl RIEDLING
Technische Universität Wien
Institut für Sensor- und Aktuatorsysteme
A-1040 Wien

Dipl.-Ing. Michael ROSENAUER
Technische Universität Wien
Institut für Sensor- und Aktuatorsysteme
A-1040 Wien

o.Univ.Prof. Dr. Friedrich SCHÄFFLER
Johannes Kepler Universität Linz
Inst. f. Halbleiterphysik und Festkörperohysik
A- 4040 Linz

Dipl.-Ing. Stephan SCHARTNER
Technische Universität Wien
Institut für Festkörperelektronik
A-1040 Wien

Univ.Prof. Dr. Ulrich SCHMID
Technische Universität Wien
Institut für Sensor- und Aktuatorsysteme
A-1040 Wien

Univ.Prof. Dr. Jörg SCHMIEDMAIER
Technische Universität Wien
Atominstitut
A- 1020 Wien

Dipl.-Ing. Dr. Werner SCHRENK
Technische Universität Wien
ZMNS
A-1040 Wien

o.Univ.Prof. Dr. Siegfried SELBERHERR
Technische Universität Wien
Institut für Mikroelektronik
A-1040 Wien

Robert SEYRKAMMER
Johannes Kepler Universität Linz
A- 4040 Linz

DI Clemens SIMBRUNNER
Johannes Kepler Universität Linz
Inst. f. Halbleiterphysik und Festkörperphysik
A- 4040 Linz

Ao.Univ.Prof. Dr. Gunther SPRINGHOLZ
Johannes Kepler Universität Linz
Altenbergerstr. 69
A- 4040 Linz

DI Almir TALIC
Research Unit for Integrated Sensor Systems
Austrian Academy of Sciences
A-2700 Wr. Neustadt

Dr. Stefan TASCH
LEDON Lighting
Jennersdorf GmbH
A-8380 Jennersdorf

Univ.Prof. Dr. Karl UNTERRAINER
Technische Universität Wien
Institut für Photonik
A- 1040 Wien

Dipl.-Phys. Alexander URICH
Technische Universität Wien
Inst. 387
A-1040 Wien

Univ.Prof. Dr. Michael VELLEKOOP
Technische Universität Wien
Institut für Sensor- und
Aktuatorsysteme
A-1040 Wien

DI Jürgen WISSENWASSER
Austrian Research Centers GmbH
A-1220 Wien

Contents

Sensors (Talks)

Miniaturized Sensors and Sensing Systems for Liquid Media

B. Jakoby[1], E.K. Reichel[1], F. Lucklum[1], B. Weiss[2], C. Riesch[3], F. Keplinger[3], A. Niedermayer[1], R. Beigelbeck[4], J. Kasberger[5], W. Hilber[1]

[1] Institute for Microelectronics and Microsensors, Johannes Kepler University Linz, Linz
[2] Institute of Fluid Mechanics and Heat Transfer, Johannes Kepler University Linz, Linz
[3] Institute of Sensor and Actuator Systems, Vienna University of Technology, Vienna
[4] Research Unit for Integrated Sensor Systems, Austrian Acad. of Sciences, Wiener Neustadt
[5] Integrated Microsystems Austria, Wiener Neustadt

One of the major research targets in our recent research has been the sensing of physical liquid parameters by means of miniaturized sensors. Such sensors and sensor systems can be utilized in applications, where liquids in industrial processes are monitored in order to maintain the quality of a process or the associated product. Due to the adverse properties commonly associated with chemical interfaces (lacking reversibility, drift, etc.), we concentrate our research on physical parameters as indicators for the state of the liquid, in particularly density, viscosity (or more general rheological properties), and infrared absorption. The miniaturization of suitable sensor principles facilitates the implementation of these devices online. At the same time, scaling effects have to be taken into account, which, e.g., in case of viscosity sensors, lead to issues when it comes to applications in complex liquids such as suspensions.

In our paper we provide an overview on our recent work discussing the device design, the associated modeling, and the application of the devices.

Keywords: Viscosity sensing, resonating sensors

Introduction

In this contribution we report on recent research on miniaturized viscosity sensors, which can be used in industrial process control and related applications wherever process liquids and changes in the liquid's condition are of interest (e.g., in food industry and engine oil quality monitoring). The viscosity (more precisely the "shear viscosity") can be defined in terms of a simple experimental arrangement, where the liquid under test is sheared between two laterally moving plates. The viscosity η is then defined as the ratio between the applied shear stress τ (maintaining the movement) and the resulting gradient of the flow velocity v (i.e. the shear rate $\dot{\gamma}$) of the liquid sheared between the plates:

$$\eta = \frac{\tau}{\partial v_x / \partial y} = \frac{\tau}{\dot{\gamma}} \tag{1}$$

The such defined viscosity (as already proposed by Newton) can be measured in a straightforward manner by laboratory instruments, which in some way impress a shear deformation on the liquid and measure the required torque (or vice versa, i.e. impress torque and measure resulting shear deformation). Such devices typically either utilize

continuous rotational movements (avoiding extended translational movements required by the simple plate setup) or oscillatory rotational movements. Most often, the viscosity as defined by (1) crucially depends on the used process parameters, e.g., the impressed shear rate. For instance consider a simple schematic arrangement as shown in Fig. 1 for the measurement of viscosity: a pivoted cylinder is immersed in a viscous liquid. By means of some motor, the cylinder can be driven to perform a continuous rotational movement or rotational oscillation.

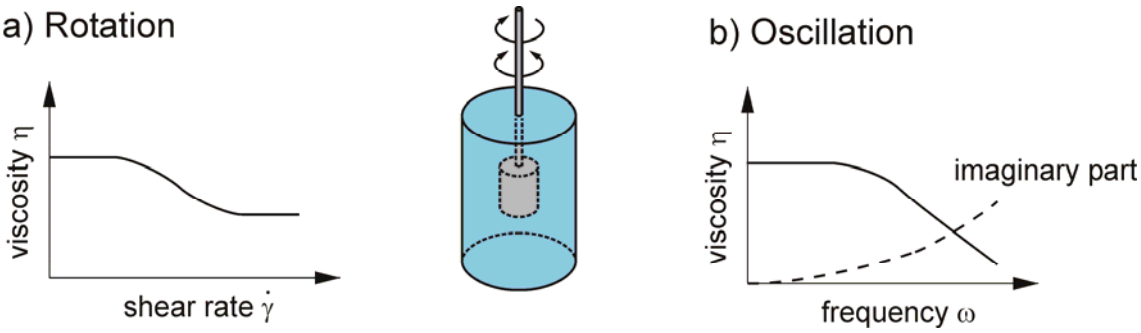

Fig. 1: Basic measurement approaches for viscosity: rotational and vibrational (oscillatory) method.

For the continuous rotation, the ratio between the applied torque and the rotational speed will be related to the viscosity of the liquid. Now for a so-called “Newtonian” liquid, this ratio yielding the viscosity would not depend on the actually applied rotational speed or, in terms of the definition (1), the viscosity would not depend on the shear rate. For real liquids, such a dependence can, however, occur if, e.g., (macro)-molecules in the liquid become disentangled by the shear movement, which would be an example for so-called “non-Newtonian” behavior. This behavior is known as shear-thinning behavior (the viscosity drops with increasing shear rate) and can be reversible or (also partly) non-reversible. This behavior represents a non-linear response, which can be accounted for by describing the viscosity a function of the shear rate. For oscillatory (vibrational) measurements, the cylinder would perform, e.g., sinusoidal oscillations, where, similarly as before, the ratio of the applied torque-amplitude and the amplitude in angular speed could be used as measures for the viscosity. The above-mentioned non-linear behavior here would lead to a dependence of the obtained viscosity on the amplitudes for angular speed and torque. Moreover, another kind of non-Newtonian behavior can appear: the measured viscosity can depend on the applied frequency. More specifically, a phase shift between the torque and the angular speed signals can appear, which represents the onset of elastic behavior. This phenomenon is often referred to as viscoelastic behavior and can be modeled by adopting the common complex notation, where an imaginary part in the viscosity accounts for the elastic part. (This is in analogy to an ohmic resistor supplemented by an additional capacitive part.) In terms of system theory, this kind of non-Newtonian behavior corresponds to a linear distortion in the system response. We note that also the reverse effect can appear at higher frequencies, i.e., dominantly elastic behavior such as the bulk compressibility of a liquid, can show viscous contributions such that the compressibility coefficient shows an imaginary part, which corresponds to the so-called bulk viscosity of a liquid. In contrast to the shear viscosity, the bulk viscosity is difficult to measure and plays a minor role in the analysis of liquid behavior such that it is often neglected.

In general both, linear and non-linear effects can occur, leading to sometimes complicated non-Newtonian behavior of liquids. In rheology, this behavior is a vibrant issue in research (see, e.g., [2] for a thorough account on this).

Considered Technologies for Miniaturized Viscosity-Sensors

As discussed above, the measurement of viscosity involves some kind of interaction of moving or vibrating parts with a liquid. In the following we discuss some fundamental principles underlying our work on miniaturized viscosity sensors.

Thickness Shear Mode Resonators and Related Devices

A very elegant and well defined way to achieve interaction of vibrating bodies with a viscous sample is that of a shear-vibrating plane being in contact with a viscous liquid. Consider an infinitely extended plane orthogonal to the *z*-axis performing a sinusoidal shear vibration (oriented in *x*-direction) with a radian frequency ω and being loaded with a viscous liquid occupying the half-space $z > 0$ above the plate. For this elementary problem, a simple solution for the flow field in the viscous liquid can be obtained in terms of an attenuated shear wave (using time-harmonic complex notation) [3]

$$v_x(z) = v_x(0) e^{j\omega t} e^{-jz/\delta} e^{-z/\delta} . \tag{2}$$

Here v_x denotes the velocity component in x direction and δ is the so-called penetration depth δ given by

$$\delta = \sqrt{\frac{2\eta}{\rho\omega}} . \tag{3}$$

This interaction can be utilized for viscosity sensing. Prominent examples are so-called thickness shear mode resonators, which are most often embodied by piezoelectric disks. The disks (most often quartz) feature electrodes on both faces. By applying an AC voltage, mechanical vibrations can be excited by means of the piezoelectric effect. Choosing an appropriate crystal cut, shear vibrations can be excited. If the disk is immersed in a viscous liquid, the interaction described above is enabled.

The impedance appearing between the electrodes features a piezoelectrically induced part, which represents the mechanical vibration. Close to the mechanical resonance frequency, this so-called motional arm can be represented as LC-resonance circuit in an equivalent circuit (see Fig. 2, see also [4]).

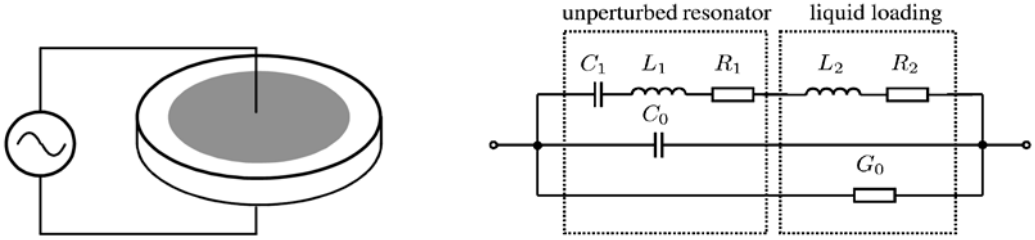

Fig. 2: TSM resonator: basic embodiment and equivalent circuit near mechanical resonance.

A straightforward analysis [4] yields that loading the resonator with a liquid leading to coupling of the shear-vibrating surfaces with the liquid as described above results in additional components L_2 and R_2 in the motional arm of the equivalent circuit. These components can be interpreted as the consequence of the additional mass loading by the entrained liquid layer resulting change in the resonance frequency and the losses

associated with the viscous dissipation in the liquid. Both parameters are approximately proportional to the viscosity-density product of the liquid

$$L_2, R_2 \propto \sqrt{\rho\eta} \tag{4}$$

There are other piezoelectric devices based on shear polarized surface bound modes such as, e.g., Love waves [5] and surface transverse waves [6], which yield similar interaction and sensitivities with respect to the viscosity-density product in terms of the wave's damping and wavenumber.

Piezoelectric excitation can be replaced by other excitation mechanisms such as excitation by Lorentz-forces. In [7] the excitation of modes in conducting (e.g., metallic) disks and membranes in terms of induced eddy currents in an external magnetic bias field is described. Here the excitation of dominantly shear-polarized modes is crucially influenced by the geometry of the excitation coil inducing the eddy currents.

Known issues in the design of shear-mode devices include spuriously excited compressional waves [8] – [10], which may lead to disturbing interferences upon reflections from nearby obstacles as, in contrast to shear waves, compressional waves are scarcely damped even in viscous liquids.

In terms of rheology, shear vibrating devices at higher frequencies show a comparatively small penetration depth δ as given by (3), e.g., for water and a frequency of 6 MHz, δ is in the order of 0.2 microns. Thus structural effects influencing the viscosity, which are related to microstructures with typical dimensions in the order of δ or above, will not be captured by the sensor. For instance, in emulsions featuring droplets in the dimensions 10 microns or above, the viscosity of the continuous phase rather than that of the entire mixture is sensed. This effect does not occur for microemulsions with droplet sizes below one micron [11]. Similar experiments have been reported with suspensions, see also the discussion for vibrating beams below [12].

Apart from the fact that kind of a "thin film viscosity" is determined, compared to oscillatory lab viscometers, the devices typically feature significantly higher vibration frequencies (some 10 kHz to some 100 MHz. At the same time the vibration amplitudes are very small (can be in the nm range). This yield shear rates in the range of $10^7 s^{-1}$ [13], where due to the sinusoidal vibration, we strictly have to speak about an averaged shear rate [14].

Non-Newtonian behavior can be detected in terms of deviations from the relation (4), which holds for Newtonian liquids only. Specifically, based on (4) a linear relation between L_2 and R_2 can be established. If a measured parameter pair yields a deviation from this linear relation this indicates non-Newtonian behavior as will be shown in an example (monitoring of zeolite synthesis) below.

Summarizing, compared to common lab instruments, shear vibrating miniaturized viscosity sensors excite the liquid under test in a significantly different rheological regime, which can be an issue for complex liquids, if the conventional "macroscopic" viscosity values have to be obtained. Still, these sensors can have benefits also for the monitoring of complex non-Newtonian liquids if a proper calibration routine or, more generally, a suitable interpretation scheme for the obtained data is worked out. The latter can be sufficient as in process control, it is often more important to detect changes in the process rather than measure absolute viscosity values. For broad application also in the laboratory, it will be essential, to standardize the method, similarly as it has been done with other novel viscosity measurement methods (e.g., the high-temperature-high-shear or HTHS method in lubrication technology (see, e.g., the standard ASTM D5481 - 04).

Vibrating Beam Devices and Membranes

Another simple vibrating structure that can be utilized to determine viscosity and density of liquids is that of a vibrating beam. Even though the structure is simple, its interaction with the liquid is more involved than that of a plane surface performing shear vibrations. However, in comparison to the thickness shear resonators discussed above, the vibrating beams described in the following feature the lower vibration frequencies and larger amplitudes such that the probed rheological regime can be expected to be more comparable to that of conventional lab viscometers, which indeed holds true in the experiment.

In our research, we considered beams implemented in silicon micromachining technology as well as beams implemented by means of thin vibrating polymer foils. The beams are excited by Lorentz forces stemming from an external magnetic field (provided by a permanent magnet) and AC-currents in conductive paths along the beam. For the readout, the induced voltage in a pickup coil (whose windings are partly on the beam and which is thus vibrating in the magnetic field) or an optical readout method can be utilized. Fig. 3 shows basic beam designs.

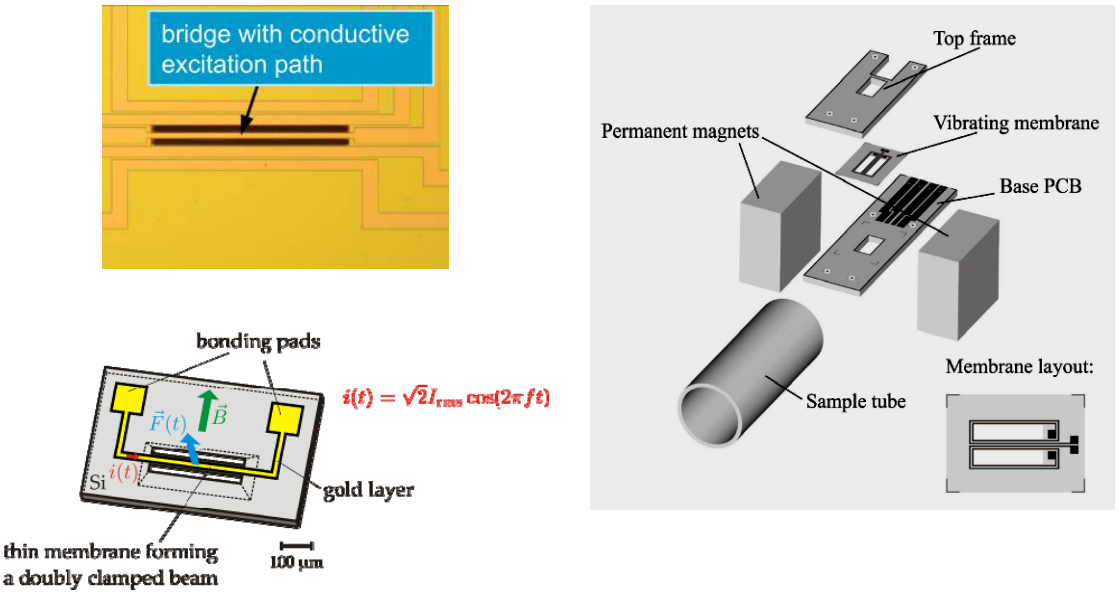

Fig. 3: Clamped-clamped beams in Si-micromachining technology (left, [15]) and polymer technology (right, [16]).

Modeling the interaction of the beam with the liquid is less straightforward. A suitable method considered is the implementation of Euler Bernoulli beam theory by introducing a distributed load along the beam, which represents the interaction with the liquid and thus depends on the transversal motion of the beam given by its lateral displacement $w(x,t)$ [17]. It can be shown [10] that for the calculation of the interaction between beam and liquid, the Navier-Stokes equations can be linearized if the displacement amplitudes in the liquid are sufficiently small. Using complex time-harmonic notation, the distributed load due to interaction with the liquid at some position x along the beam can be linearly related to the displacement amplitude at x by means of a complex-valued coefficient (”mechanical impedance”). In order to determine this coefficient, a 2D approximation can be made if it is assumed that the liquid movements in the direction of the beam axis are negligible. Thus, considering a vibrating cross section of the beam in a 2D model, the ratio between complex resistance force and associated displacement amplitudes can be determined to obtain said coefficient. In [17] the model involving a

spectral domain approach is described. Fig. 4 shows the problem and the plane of computation for the 2D problem as well as an example for the flow field around the vibrating beam cross section computed with the spectral method in 2D.

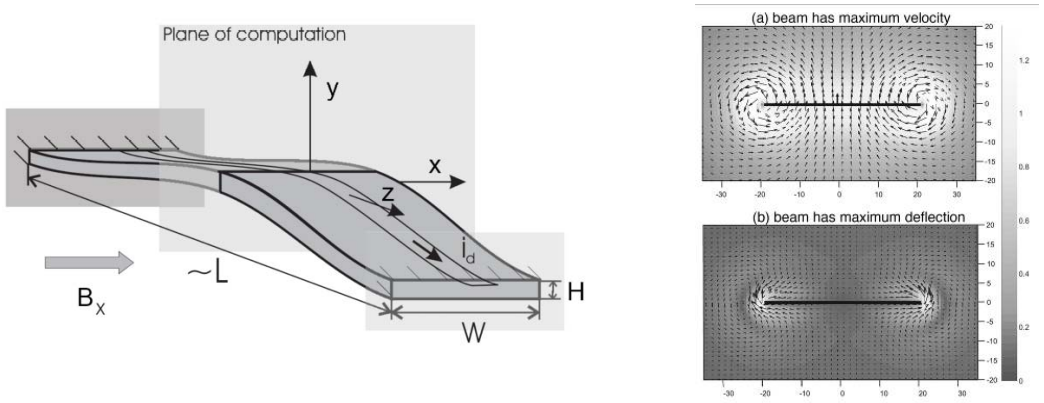

Fig. 4: Beam geometry and associated 2D plane of computation for the fluid resistance force (left) and example for the resulting flow field in the 2D problem (right).

The resulting effect on the beam's frequency response is involved but it can be roughly stated that the density mainly affects the resonance frequency while the viscosity dominantly determines the Q-factor (or damping coefficient *D*) of the resonances.

To compare the rheological behavior of beams and TSM resonators, suspensions and Newtonian liquid samples have been characterized with both devices [12]. A glimpse on the results is shown in Fig. 5. These results indicate that a TSM resonator is not suitable for the measurement of viscosity or concentration of the considered SiO_2–in–H_2O suspensions (Samples 1 to 8), whereas the results for Newtonian liquids (alcohols) follow the expected relation (4). For the vibrating bridge, all these liquids yield a damping coefficient nicely correlating with the liquid's viscosity as determined by a lab instrument [12].

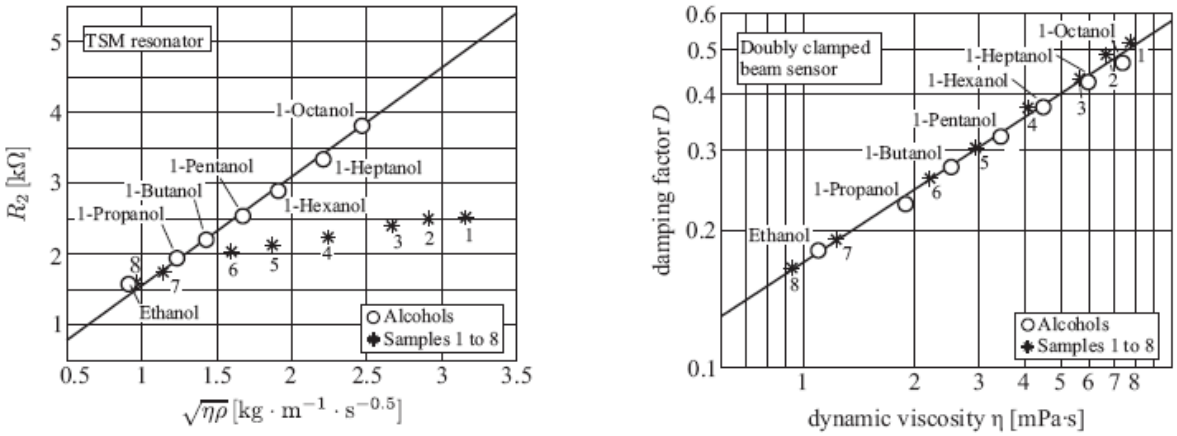

Fig. 5: Viscous loss resistance R2 of a 6 MHz quartz TSM resonator vs. square root of the viscosity-density product (left) showing deviations for non-Newtonian liquid samples. In contrast, the damping factor of a vibrating bridge shows a nice correlation with the viscosity also for complex liquids (right).

We finally note, that the concept of the beam devices is related to the concept of vibrating membranes. In [18] a device is described where the liquid under test is contained in a liquid cell featuring flexible bottom and top walls. Exciting vibrations in these walls, similarly as in the case of the vibrating bridges discussed above, the fluid properties of the liquid will influence the associated resonance properties. This device is suitable for integration in miniaturized fluidic systems. Figure 6 shows an associated device and typical results illustrating that the relation between the liquid parameters viscosity and density to the device parameters frequency and damping is more complex than for the devices described above (both liquid parameters influence both device parameters) [18].

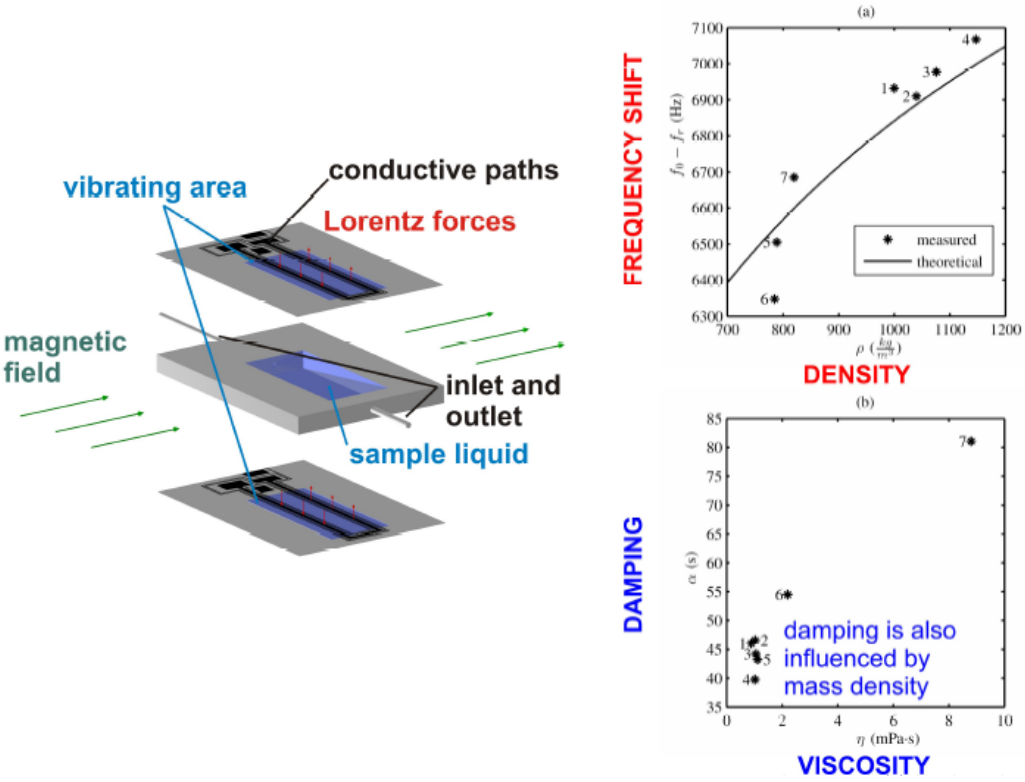

Fig. 6: Double membrane device where the liquid is contained in a cell with vibrating top and bottom walls. Measurements for liquids with various viscosity and density values show that both values influence damping as well as viscosity (right)

Other Technologies for Liquid Sensor Systems

A lot of monitoring applications involve liquids containing particles. Separating particles with respect to size and/or density is thus an interesting approach to gain knowledge about a liquid sample (suspension). A suitable technology for particle sorting is the utilization of the dielectrophoretic effect. At our lab we are particularly working on 3D AC electro-osmotic (3D-ACEO) pumps, utilizing periodic arrays of interdigitated, stepped electrodes at the channel boundary. These pumps have on the one hand the ability to achieve flow rates up to mm s^{-1} by application of an AC voltage in the range of only a few volts and can on the other hand be utilized for simultaneous particle separation in the microchannel with respect to size and density. This novel separation mechanism is based on the competitive interplay of the forces acting upon the particles in the microchannel during operation of the pump, namely dielectrophoretic, viscous drag as

well as gravitational and buoyancy forces. By varying amplitude and frequency of the driving voltage, the ratio of these forces is tunable, which provides an effective means for size and density dependent particle manipulation, which we have studied both experimentally [19] and theoretically [20]. Based on these findings we have developed pump designs, capable of pumping and separating particle mixtures in suspensions simultaneously.

Infrared absorption measurements are another powerful way to characterize liquid samples. In a joint strategic research activity with Integrated Microsystems Austria, we work on the design of a fully integrated infrared absorption sensor, which is capable to determine chemical properties by investigating infrared absorption at selected distinct wavelengths in the mid infrared region. For example, in order to reduce the frequency of scheduled maintenance of lubrication oil, e.g., in combustion engines, the quality of the deteriorated oil has to be determined, which has been selected as pilot application for our development (this has been investigated in a previous project with AC2T research). Based on results of transmission spectroscopy, it was shown that by means of a properly designed optical waveguide structure, a sensitivity similar to that obtained by transmission spectroscopy, as used in the laboratory, can be achieved by an integrated system. To achieve a highly sensitive absorption element, a planar monomode waveguide is utilized which requires an appropriate coupler to couple the infrared light into the waveguide. The employed grating couplers have been modeled in order to derive a design yielding the desired sensor performance. As the targeted wavelength is located in the mid-infrared region, a suitable infrared source or detector, respectively, can be fabricated by thermal components [21].

Conclusions

Microsensor technology facilitates the implementation of sensors for online applications in industrial processes and plants. Devices involving vibrating structures immersed in liquids can be used to determine mechanical and in particular, rheological properties. Due to the associated small vibration amplitudes and high frequencies, the rheological domain can be quite different to that probed by common lab equipment. In particular, this may be an issue for non-Newtonian liquids such as emulsions and suspensions. For the monitoring of changes in the liquid such as phase transitions, the specifically considered rheological domain plays a minor role and the sensor output signals can be subjected to a calibration procedure of some sort.

Acknowledgements

The work reported in this paper was partly supported by the Austrian funding agencies FFG (project ASAP-SERMER) and FWF (project L103-N07) and the Austrian K_{ind} program supporting Centers of Competence. The support of some of the mentioned activities by the JKU's Institute of Semiconductor and Solid State Physics (in particular Dr. Thomas Fromherz and Patrick Rauter) and its cleanroom facilities is gratefully acknowledged.

References

[1] J. Kuntner, G. Stangl, and B. Jakoby, "Characterizing the Rheological Behavior of Oil-Based Liquids: Microacoustic Sensors Versus Rotational Viscometers", IEEE Sens. J., vol. 5, no. 5, p. 850-856, Oct. 2005

[2] C. Macosko, "Rheology: Principles, Measurements and Applications", Wiley/VCH, Poughkeepsie, NY, ISBN: 0-471-18575-2, 1994

[3] L.D. Landau and E.M Lifschitz, “Lehrbuch der Theoretischen Physik, Band VI, Hydrodynamik”, Akadamie Verlag, 1991

[4] S.J. Martin, V.E. Granstaff, G.C. Frye, “Characterization of a quartz crystal microbalance with simultaneous mass and liquid loading”, Anal. Chem. 63 (1981) 2272–2281.

[5] B. Jakoby and M. J. Vellekoop, “Properties of Love waves: applications in sensors,” Smart Mater. Struct., vol. 6, pp. 668–679, 1997.

[6] Baer R L, Flory C A, Tom-Moy M and Solomon D S, “STW chemical sensors”, Proc. IEEE Ultrasonics Symp. (New York: IEEE) pp 293–8, 1992

[7] F. Lucklum and B. Jakoby, “Novel magnetic-acoustic resonator sensors for remote liquid phase measurement and mass detection,” Sensors and Actuators A, vol. 2008, pp. 44–51, July, August 2008.

[8] B. A. Martin and H. E. Hager, J. Appl. Phys. 65, 2630, 1989.

[9] R. Thalhammer et al., Proceedings of the IEEE International Frequency Control Symposium, IEEE, Orlando, FL, 1997, pp. 105–113.

[10] R. Beigelbeck and B. Jakoby, “A two-dimensional analysis of spurious compressional wave excitation by thickness-shear-mode resonators,” J. Appl. Phys., vol. 95, pp. 4989–4995, May 2004.

[11] B. Jakoby, A. Ecker, and M. J. Vellekoop, “Monitoring macro- and microemulsions using physical chemosensors,” Sensors and Actuators A, vol. 115, no. 2-3, pp. 209–214, 2004.

[12] C. Riesch, E.K. Reichel, A. Jachimowicz, F. Keplinger, B. Jakoby, “A Micromachined Doubly-Clamped Beam Rheometer for the Measurement of Viscosity and Concentration of Silicon-Dioxide-in-Water Suspensions”, Proc. IEEE Sensors Conference 2008, Lecce, Italy, Oct 26–29, 2008, pp. 391–394.

[13] F. Krispel, C. Reiter, J. Neubig, F. Lenzenhuber, P. W. Krempl, W. Wallnöfer and P. M. Worsch, “Viscosity sensor based on a symmetric dual quartz thickness shear resonator”, Proc. 2003 IEEE International Frequency Control Symposium, Tampa, USA, 5-8 May 2003, p. 1048- 1054

[14] Personal communication with R. Schnitzer, M. Gröschl, E. Benes, and S. Radel

[15] C. Riesch, E.K. Reichel, A. Jachimowicz, F. Keplinger, B. Jakoby, “A Novel Sensor System for Liquid Properties Based on a Micromachined Beam and a Low-Cost Optical Readout”, IEEE Sensors 2007 Proceedings, p. 872 - 875.

[16] E.K. Reichel, C. Riesch, B. Weiss, B. Jakoby, “A Vibrating Membrane Rheometer Utilizing Electromagnetic Excitation”, Sensors and Actuators A: Physical, 7/8-2008, Vol. 145-146, p. 349-353.

[17] B. Weiss, E. K. Reichel, B. Jakoby, “Modeling of a clamped–clamped beam vibrating in a fluid for viscosity and density sensing regarding compressibility”, Sensors and Actuators A: Physical, Vol 143, Iss 2, 16 May 2008, p. 293-301

[18] E.K. Reichel, C. Riesch, F. Keplinger, B. Jakoby, “Resonant Measurement of Liquid Properties in a Fluidic Sensor Cell”, Proc. Eurosensor XXII 2008, Dresden, VDI, p. 540-543

[19] W. Hilber, B. Weiss, M. Mikolasek, R. Holly, K. Hingerl and B. Jakoby, “Particle manipulation using 3D ac electro-osmotic micropumps”, J. of Microelectronics and Microengineering, 18, 064016, 2008.

[20] B. Weiss, W. Hilber, R. Holly, P. Gittler, B. Jakoby and K. Hingerl, “Dielectrophoretic particle dynamics in alternating-current electro-osmotic micropumps”, Appl. Phys. Lett., 92, 184101, 2008.

[21] J. Kasberger, B. Jakoby, “Design of a Novel Fully Integrated IR - Absorption Sensor System” , Proceedings IEEE Sensors Conference 2007, p. 515-518, 10-2007, ISBN: 1-4244-1262-5

Magnetic Lab-on-a-Chip: Magnetic Nanoparticles for Biomedical Diagnostics

H. Brückl, J. Schotter, N. Kataeva, A. Shoshi, O. Bethge, S. Schrittwieser

'Nano-System-Technologies', Austrian Research Centers GmbH – ARC, Donau-City-Str. 1, 1220 Vienna, Austria

Recent progress in fabrication and characterization of magnetic nanoobjects like rods and beads has triggered many ideas and possible applications in the biomedical field. A magnetic biochip using the combination of both magnetic nanoobjects as markers and magnetoresistive sensors has proven to be competitive to standard fluorescent DNA-detection at low concentrations. Superparamagnetic nanoparticles are detected via giant magnetoresistance (GMR) or tunnel magnetoresistance (TMR) sensors. Their size ranges from a few nm up to few 100 nm and can be reliably reproduced by physical or chemical processes.

Magnetic nanoobjects additionally provide the unique possibility to actively manipulate biomolecules, on-chip, which paves the way to an integrated 'magnetic lab-on-a-chip' combining detection and manipulation. Manipulation can be accomplished either by an external magnetic field or on-chip via currents running through specially designed line patterns on a chip platform. It can be shown that hybridization processes can be accelerated compared to usual thermal activation. A prototype is under development for Sepsis diagnosis. The ultimate goal is the detection of antibodies at the picomolar level at shortest reaction times.

Today's lab-on-a-chip systems are designed in such a way that surfaces play a major role, either as substrate where molecular reaction takes place or as sensor environment for detection, combined with microfluidics. This makes them complicated, slow, and ineffective. Looking forward, a paradigm shift from the 'magnetic lab-on-a-*chip*' to a 'magnetic lab-on-a-*bead*' is discussed as a future device solution. Ferromagnetic nanoobjects are thereby directly used as both molecular recognition sites and detection units. Information about binding events is communicated via characteristic property changes of the nanoobjects which are remotely detected. For this, we envisage a combination of magnetorelaxation and plasmon detection. Symmetry considerations and numerical estimations show that anisotropic magnetic core-shell nanoobjects are best suited for this task. Au-decorated iron oxide nano-spindles were synthesized and investigated for such purposes.

Integrated Cell Analysis Devices

Michiel J. Vellekoop

Institute of Sensor and Actuator Systems, Vienna University of Technology, Vienna, Austria

Introduction

The increased interest of biotechnologists to learn more about the functioning of cells has resulted in various research projects where microdevices and some times nanodevices are investigated to yield information from cells. The miniaturization of the analysis chambers and the integration of microsensors and -actuators allow new measurement techniques and new insights.

Two developments are visible; the analysis of single cells suspended in a buffer fluid, and the analysis of cell cultures that are, however, much smaller than the classical culture which contains millions of cells. Small cell cultures roughly contain less than one million cells and are grown on a sensor chip. The advantages of studying single cells and small cultures are technical; the origin and the initiation of diseases for example can be better examined. Also costs can play a significant role because of the small amount of cells and chemicals needed. For several applications it is investigated if physical and electronic analysis methods can be used to study cells and cell behavior. Optical, electrical, magnetic, and thermal properties are examples of physical effects that are being used.

Microfluidics has become an important field in on-chip analysis devices for the control of gases and liquids that contain the cells or chemicals to treat or nurture the cells.

Microfluidics for Single Cell Analysis

For on-chip manipulation and handling of particles and cells microfluidic elements can be designed. In passive hydrodynamic focusing, a channel is being narrowed down which causes a sample flow that is surrounded by a carrier flow to narrow down accordingly. In order to control the height and width of the sample flow, a non-coaxial fluidics chip was developed where the ratio of the flow rates of carrier flow and sample flow determines the height of the sample flow. By using fluidic sideports through which carrier flow can be injected or withdrawn from the main flow, the width of the sample flow can be adjusted and controlled. The position and size of the sample flow can thus be controlled allowing to steer the suspended particles or cells to certain locations for further handling, for analysis (sensors) and for sorting. Further, the chance of clogging is dramatically reduced [1]. An example where we benefit from this device is the optical projection cytometer where cells can flow very closely over integrated optical sensors so that near-field projection optics can be applied. A second example is an integrated Coulter counter where sensitivity can be greatly enlarged by controlling the diameter of the conductive sample flow containing the particles surrounded by a non-coaxial non-conductive carrier flow. The limits of further downscaling these (non-)coaxial fluidic devices have been investigated in [2].

Sensing

As mentioned in the introduction, cell parameters which are of interest to determine are identity, size, shape, quantity, viability, biochemical activity, and electrical activity. Outside electrochemical detection systems, the sensing systems applied for cell detection and characterization are mostly based on optical and electrical (impedance) principles.

The measurement of electrical impedance of cells also yields information on type, viability, membrane and cytoplasm. An example of a flow-through impedance characterization setup can be found in [3]. At lower frequencies, information on the cell membrane can be obtained, at higher frequencies, the conductivity of the cytoplasm can be determined. Instead of a setup where the cell flows between two electrodes, a Coulter counter can be used to determine the electrical impedance of particles. By applying conductive sample fluid and non-conductive carrier fluid in the non-coaxial sample sheath flow chip described in the previous section, the impedance of the sample can be monitored. When a particle or cell flows through, the impedance will change. For solid particles, successful measurements have been conducted [4]. For cells this has been demonstrated in [5].

Optical cytometry is one of the standard methods for cell characterization [6]. In a typical system scattered and reflected light – often fluorescent – is measured which gives information about cell size, viability and cell type. In a new approach an on-chip near-field optical projection cytometer has been developed. The shadow of a particle that flows through the near field of a strip photodiode is being recorded. The non-coaxial microfluidics setup described in the previous section is being applied to get the particles or cells in the near field of the detector, reducing interference and thus allowing the recording of a projection (shadow). Measurements with transparent and non-transparent particles showed the potential of the system to determine optical properties of particles and cells. (Semi)optical particles act as a lens and instead of a decrease in photocurrent output, an increase can be detected, depending on size and transparency of the particle. The use of this effect for identification of different cells has been shown for yeast and CHO cells [7]. The measurement response for those cells also shows a positive peak, which indicates that the light is indeed focused by the cell increasing the sensor signal – the cell acts like an optical lens.

Sorting

For selection and sorting of particles and cells, different principles have been applied. An important method is dielectrophoresis, where forces can be applied to cells by electric polarization. By switching electric fields in the microchannel single particles can be selected (e.g. [1]). This can be a very useful tool to accumulate particles of specific interest after analysis in a flow-through system. Due to the more complex structure of cells (wall, membrane, cytoplasm) the electric polarization is frequency dependent and so is the DEP force (can be positive of negative). This effect can be used to determine viability [8] or to separate cells from mixtures [9].

Conclusion

Different techniques for monitoring and analysis of single cells or small cultures are being investigated successfully, such as on-chip culturing, flow-cytometry and array analysis. In addition to electrochemical methods, physical detection methods are currently being developed, yielding extra information on cell properties (e.g. optical and mechanical) and cell behavior.

Acknowledgements

This project is a part of a joined EU Marie Curie Research Training Network (MRTN) “On-Chip Cell Handling and Analysis” CellCheck. Project no. MRTN-CT-2006-035854.

References

[1] J.H. Nieuwenhuis, “Microsystems for Particle Analysis”, ISBN 3-85465-014-0, 2005.

[2] G. Hairer, M.J. Vellekoop, “An integrated flow-cell for full sample stream control”, Acc. for publication in the Journal of Microfluidics and Nanofluidics (2009).

[3] K. Cheung, S. Gawad, P. Renaud, “Impedance spectroscopy flow cytometry: On-chip label-free cell differentiation”, Cytometry Part A, Vol. 65A (2), 2005, pp. 124-132.

[4] J.H. Nieuwenhuis, F. Kohl, J. Bastemeijer, P.M. Sarro, M.J. Vellekoop, “Integrated Coulter Counter based on 2-Dimensional Liquid Aperture Control”, S&A B 102 (2004), pp. 44-50.

[5] S-H. Oh, D.K. Wood, S-H. Lee, K.Y. Dane, P.S. Daugherty, H.T. Soh, A.N. Cleland, “Micromachined Broadband RF Cytometer for High-Throughput Analysis of Mammalian Cells”, Proc. of MicroTAS 2005, pp. 1507-1509.

[6] H. M. Shapiro, “Practical Flow Cytometry”, 4th edition, Wiley, 2003, ISBN 0-471-41125-6.

[7] S. Kostner, M.J. Vellekoop, “Interpretation of projection cytometer signals for cell analysis”, Sensors and Actuators B: Chemical, Volume 132, Issue 2, 2008, pp. 631-636.

[8] H. Li and R. Bashir, “Dielectrophoretic separation and manipulation of live and heat-treated cells of Listeria on microfabricated devices with interdigitated electrodes”, S&A B 86, pp. 215-221, 2002.

[9] S. van den Driesche, S. Kostner, W. Witarski, M.J. Vellekoop, “A Strip electrode design for robust continuous cell separation based on positive and negative dielectrophoresis, acc. for presentation at microTAS 2009.

Nanostructures and Nanotechnology (Talks)

Nanoimprint Lithography

M. Mühlberger, I. Bergmair, W. Schwinger, M. Chouiki, H. Wiesbauer, H. Leichtfried, R. Schöftner

Profactor GmbH, Im Stadtgut A2, 4407 Steyr-Gleink, Austria

Introduction

Nanoimprint Lithography (NIL) is an emerging nanoreplication technology with the potential for high throughput and low cost for a huge variety of applications. The basic idea is to have a stamp which contains a (nano-) pattern. This pattern may be binary but can also contain different height levels, curved or sloped featured (e.g. microlenses) etc. In a typical nanoimprint process this stamp is then pressed into a soft material which is coated on a substrate. This soft material can be a UV-curable material but also a thermoplastic one. After UV-curing or cooling down below the glass transition temperature the stamp is removed from the now hardened material, which then features the reverse topography of the stamp. Postprocessing steps like reactive ion etching may follow, however the polymer can also already be the finished device. Since the first proposal by Richard Feynman in his famous lecture “There is plenty of room at the bottom” (1959) and the first publications of S. Y. Chou [1], [2], Haisma [3] and Xia [4] in the mid 1990ies a lot of progress has been made as far as equipment, processes and materials are concerned. Hot embossing or thermal NIL (using a thermoplastic polymer), UV-NIL (utilizing a UV-curing polymer) and micro- or nano-contact printing (μ/n-CP), where an ink is transferred from the stamp to the substrate) are 3 basic variants of the same nanoimprint idea.

Each of these 3 processes appears in a different form in the literature. There is roller NIL [5], reversal NIL [6], combined photo- and nanoimprint lithography [7] etc. The imprint polymer can be droplet dispensed [8] or spin coated [9]. Typically hot embossing processes require higher pressures than UV-NIL processes [10] with μ-CP processes using the lowest pressure [11].

Advantages

The main advantages of NIL are the following:

a) high resolution in a fast process: Due to the stamping nature of the process, NIL is inherently parallel and therefore fast. It may take hours, days or weeks to fabricate the master stamp, but to replicate the patterns only takes seconds or minutes. Soon after the first publications it was shown, that sub 10 nm features can be replicated (see e.g. [12] or [13]).

b) direct 2.5D patterning: If the stamp exhibits several different height levels or curved features, this can be replicated as well (see e.g. [14] or [16]).

c) direct structuring of functional materials: After the imprinting step it is not mandatory that an etching step follows to transfer the pattern into the substrate. In many cases the structured polymer is already the final device (see e.g. [17]).

These advantages make NIL very interesting for industrial but also research applications. Nanoimprint Lithography has also been included in the ITRS roadmap [15] and in technology review’s list of “10 Emerging Technologies That Will Change the World” [19].

Challenges

The Stamp

The stamp is a central part in the imprinting process. The result of the imprint process usually can only be as good as the stamp. Stamps are commonly fabricated by electron beam (e-beam) lithography. The e-beam lithography is followed by reactive ion etching (RIE). For stamps with 2.5dimensional structures, i.e. features that contain multiple height levels or curved and inclined surface features (but no undercut features!) grey-scale lithography (either optical or e-beam is used). Also the use of two-photon polymerization for stamp fabrication has been reported [20]. A promising technology is also PMLP (projection maskless patterning) by IMS Nanofabrication AG [18], that allows the use of several thousand of beams in parallel combined with direct patterning of the substrate [21], [22].

Soft stamps e.g. from PDMS (Poly-dimethylsiloxane) are made from nanostructured masters by casting the liquid PDMS on the master and removing it after the PDMS has been hardened (see e.g. [23]).

The stamps have to be compatible with the imprint material, i.e. they must be easy to remove from the hardened polymer and they must not undergo a (chemical) reaction with the imprinting material. To reduce the sticking of the stamp to the imprint polymer, usually an anti-adhesion layer is applied to the stamp. Such a layer is typically a self-assembled monolayer of fluorinated silanes [24]. There is however a debate going on regarding the durability and therefore also the suitability of such layer for the production process, and diamond-like carbon layers have been suggested and tested [25], [26].

To reduce the risk to damage the stamp during the imprint process it is advantageous to use working stamps instead of the original master. These stamps are replicated from the master and then used for imprinting. Materials for such working stamps can be Ormocer-based materials like Ormostamp [27], [28] or polymeric materials like PFPE (perfluoropolyether) [29] – [31], but also PDMS.

The Materials

The following parameters have to be considered when designing or choosing a suitable polymer for a certain process:

a) Adhesion to the substrate. The polymer has to stick to the substrate and it has to wet the substrate. Adhesion promoters like Ti-Prime [32] or HMDS (Hexamethyldisilazane) can be used.

b) Non-adhesion to the stamp. When stamp and substrate are separated from each other the cured polymer has to remain on the substrate and not on the stamp. Should for some reason the polymer stick on the stamp, it must be easy to remove from the stamp, without the danger of changing the features on the stamp during the cleaning procedure.

c) Functionality. The imprinting polymer has to fulfill certain tasks after having been patterned, e.g. serve as an etching mask. In this case the etching selectivity has to be high enough with respect to the substrate (see e.g. [33], [34]). The polymer can also serve as an optical element, in that case the optical parameters and the durability for the desired application are important [35], [36].

d) Process compatibility. The imprint polymer must not interact with the stamp material. Any swelling of soft stamps has to be avoided.

e) nCP inks. Similar considerations are valid for the inks used in nCP. Again they must not destroy the stamp, wet the substrate but also the stamp to allow for a homogene-

ous distribution on the stamp surface. A high vapor pressure of the ink molecules has to be avoided to reduce the risk of material deposition in areas where not deposition is wanted. Diffusion on the substrate surface has to be minimized [37], [38]. For the stamp material similar considerations are valid.

The Process

Contact

The first challenge is to bring the stamp in close and homogeneous contact with the substrates. Both stamp and substrate are not perfectly flat. There are several approaches regarding this topic, which basically all make it possible for the substrate of the stamp (or both) to bend during the imprinting process: a compliant layer [39], flexible stages [40] or air cushions [41] are used to name a few examples. When bringing the stamp into contact one has to take care not to trap too much air in the cavities of the stamp. In many cases small air bubbles dissolve in the imprint material, larger bubbles however remain for a long time and therefore the process time is significantly increased. It is obvious that the inclusion of particles between stamp and substrate has to be avoided.

Residual Layer

The residual layer is the layer of imprinting polymer that remains in the areas where the material has been pressed down. This layer can usually not be avoided, since either too much time or too much force would have to be exerted to reduce it almost completely (see e.g. [42] p. 53ff). It is also not completely unwanted since it prevents the stamp from getting into direct hard contact with the substrate, which is especially advantageous if hard stamps are used. To enable further processing like reactive ion etching this layer has to be removed (by oxygen plasma etching). If the residual layer is homogeneous and thin this breakthrough etch can be performed without degrading the overall pattern quality. To optimize the residual layer thickness, knowing the filling factor of the stamp is critical, i.e. the ratio of cavities on the stamp to the total stamp area, as it determines the necessary amount of material to fill all cavities and still produce a homogeneous film, without any unfilled features. To achieve a homogeneously thin residual layer, the filling factor should be constant on the stamp (which can not always be achieved) and the pressure distribution during the imprinting process has to be as homogeneous as possible, which is mainly a quality criterion for the imprinting setup. Another parameter that enters the equation is the viscosity of the imprinting polymer. For imprint polymers with higher viscosity as used e.g. in hot embossing often a compromise has to be made between imprinting time and imprinting pressure on the one hand and residual layer thickness on the other hand. Time and pressure should be kept small, which increases the residual layer thickness. Residual layer thicknesses below several 10 nm can be achieved routinely and are very well suited for post-processing.

Alignment

To bring stamp and substrate very close to each other, do the alignment and then press the stamp into the imprinting polymer, without misaligning is difficult to achieve. Often in-liquid alignment is performed, i.e. alignment when the stamp is already pressed into the imprinting polymer (with less pressure than needed for the actual imprinting step). For the often necessary sub 100 nm alignment accuracy optical microscopes have been used, implementing Moiré-alignment markers and sub-pixel image processing [43] diffraction techniques [44] or interferometric setups [45]. Also dual focus x-ray alignment microscopes have been used for alignment in NIL [46]. Stamp and substrate distortions influence the alignment accuracies over larger areas so that again the imprinting pressure homogeneity is crucial for good results [47].

Demolding

After the imprinting process the stamp has to be removed from the substrate. Here the structure can be damaged in various ways, either by being deformed or ripped off. If the adhesion of the imprint polymer to the substrate is not high enough it can happen that large areas of the polymer are removed from the substrate and stick to the stamp, which then requires careful cleaning.

Depending on the kind of stamp and equipment used either parallel demolding or peeling off can be used. Flexible stamps are often advantageous for easy demolding, since they can deform and the forces acting on the imprint polymer are reduced.

Inspection

It is an unsolved issue how a fast inspection of nanoscale features on a large area can work, especially if the geometry of the features is complex and has many height levels. Many investigations concerning this topic have been performed by Molecular Imprints Inc. [48], e.g. [49].

Examples

Examples for the successful use of nanoimprint lithography stem from a wide range of very different applications. Most of them are still to be found in a research environment, but there are also industrial applications, where NIL is already used as a production tool or where it is planned to be used. Many examples can be found in the field of optics or photonics, like the fabrication of metamaterials [50], [51], polarizers [52], [53] and for the fabrication of photonic crystal structures [54], [55]. Nanoimprint lithography is also used for the replication of diffractive optical elements and microlenses [16] also for mass production e.g. [56] performed on equipment of EVG [57], [58]. It has been used to structure the donor-acceptor interface in organic solar cells [59]. The replication of multi-level features has been published e.g. in [60] or [61]. In the field of biology NIL has been used for example to pattern substrates for cell growth [62], [63] to fabricate Gold nanoislands [64] and to prepare chemical gradients on surfaces [65]. One of the most demanding but also interesting applications will be the preparation of next generation hard disks, so called bit patterned media. Here nanoimprint lithography will most probably find a real high volume industrial application (see e.g. [66], [67]). The list of applications could be extended significantly.

Conclusions

Nanoimprint Lithography has been shown to be able of high resolution and high throughput patterning making it highly interesting for a number of applications, in a research environment as well as for industrial applications. The challenge is to improve materials and processes and also the equipment even further to meet the demands of the industry. Nevertheless nanoimprint lithography is already today a very powerful tool for nanopatterning.

Acknowledgements

Financial support from the European Union (FP6 project 3DNanoPrint, www.profactor.at/3dnanoprint) and the Austrian Nanoinitiative (FFG and bmvit, NILaustria project cluster, www.nilaustria.at) is gratefully acknowledged.

References:

[1] Chou, S.Y., R.P. Krauss, and J.P. Renstrom, Imprint of sub-25 nm vias and trenches in polymers. Applied Physics Letters, 1995. 67(21): p. 3114-3116.

[2] Chou, S.Y., P.R. Krauss, and J.P. Renstrom, Nanoimprint lithography. Journal of Vacuum Science & Technology B, 1996. 14: p. 4129-4133.

[3] J. Haisma, M. Verheijen, K. v. d. Heuvel, and J. v. d. Berg, Mold-assisted nanolithography: A process for reliable pattern replication. Journal of Vacuum Science & Technology B, 1996. 14: p. 4124-4128.

[4] Y. Xia, E. Kim, M. Mrksich, and G. M. Whitesides, Microcontact Printing of Alkanethiols on Copper and Its Application in Microfabrication. Chem. Mater., 1996. 8(3): p. 601-603.

[5] Tan, H., A. Gilbertson, and S.Y. Chou, Roller nanoimprint lithography. Journal of Vacuum Science & Technology B: Microelectronics and Nanometer Structures, 1998. 16: p. 3926-3928.

[6] Bao, L.R., et al., Nanoimprinting over topography and multilayer three-dimensional printing. Journal of Vacuum Science & Technology B: 2002. 20: p. 2881-2886.

[7] Cheng, X. and L.J. Guo, A combined-nanoimprint-and-photolithography patterning technique. Microelectronic Engineering, 2004. 71(3-4): p. 277-282.

[8] Colburn, M., et al. *Step and Flash Imprint Lithography for sub-100nm Patterning*. in SPIE's 25th Intl. Symp. Microlithography: Emerging Lithographic Technologies III. 2000. Santa Clara, CA

[9] M. Bender et al., *Fabrication of nanostructures using a UV-based imprint technique*, Microelectronic Engineering, (2000) 53 (1-4): p. 233-236

[10] H. Schift., Nanoimprint Lithography: An old story in modern times? A review, J. Vac. Sci. Technol. B 26(2) 458-480 (2008)

[11] Michel, B., et al., Printing meets lithography: Soft approaches to high-resolution patterning. IBM Journal of Research and Development, 2001. 45(5): p. 697-719.

[12] Austin, M.D., et al., Fabrication of 5 nm linewidth and 14 nm pitch features by nanoimprint lithography. Applied Physics Letters, 2004. 84(26): p. 5299-5301.

[13] Hua, F., et al., Polymer Imprint Lithography with Molecular-Scale Resolution. Nano Lett., 2004. 4(12): p. 2467-2471.

[14] Park, S.-H., et al., Effective fabrication of three-dimensional nano/microstructures in a single step using multilayered stamp. Applied Physics Letters, 2006. 88(20): p. 203105.

[15] International Technology Roadmap for Semiconductors, http://public.itrs.net/

[16] Gale, M.T., Replication techniques for diffractive optical elements. Microelectronic Engineering, 1997 34(3.4): p. 321 - 339

[17] Kim, M.-S., et al., Flexible conjugated polymer photovoltaic cells with controlled heterojunctions fabricated using nanoimprint lithography. Applied Physics Letters, 2007. 90(12): p. 123113.

[18] IMS Nanofabrication AG, www.ims.co.at

[19] Special Report Technology Review, 10 Emerging Technologies That Will Change the World. Technology Review 2003, 106, 36
http://www.technologyreview.com/article/13060/

[20] Park, S.-H., et al., Effective fabrication of three-dimensional nano/microstructures in a single step using multilayered stamp. Applied Physics Letters, 2006. 88(20): p. 203105

[21] E. Platzgummer, H. Loeschner and G. Gross, Proc. SPIE Vol. 6730, pp. 673033-1 – 673033-9 (2007)

[22] E. Platzgummer, H. Loeschner and G. Gross, presented at EIPBN 2008, Portland, USA, May 30, 2008, submitted to J. Vac. Sci. Technol. B., Nov/Dec 2008

[23] Bender, M., et al., High resolution lithography with PDMS molds. Journal of Vacuum Science & Technology B, 2004. 22: p. 3229-3232.

[24] Beck, M., et al., Improving stamps for 10 nm level wafer scale nanoimprint lithography. Microelectronic Engineering, 2002. 61-62: p. 441-448

[25] Houle, F.A., et al., Antiadhesion considerations for UV nanoimprint lithography. Applied Physics Letters, 2007. 90(21): p. 213103.

[26] Grigaliūnas, V., et al., Imprint Lithography for Large Scale Angular Encoders. Materials Science, 2007. 13(2): p. 103-106

[27] M. Mühlberger et al., UV-NIL with Working Stamps made from Ormostamp. Microelectronic Engineering, accepted for publication

[28] Microresist technology GmbH, Ormostamp. http://www.microresist.de/produkte/ormocer/pdf/ormostamp_080821_en.pdf

[29] Truong, T.T., et al., Soft Lithography Using Acryloxy Perfluoropolyether Composite Stamps. Langmuir, 2007. 23: p. 2898-2905.

[30] Liquidia Technologies, I., Perfluoropolyethers as Enabling Materials in Micro and Nano-technologies, NCMC-8, Editor. 2005. p. 46.

[31] Huang, Y., et al., Solvent Resistant Microfluidic DNA Synthesizer. Lab on a Chip, 2007. 7(1): p. 24-26

[32] Microchemicals. Ti-Prime. http://www.microchemicals.de/adhesion_promotion.html

[33] Vogler, M., et al., Development of a novel, low-viscosity UV-curable polymer system for UV-nanoimprint lithography. Microelectronic Engineering, 2007. 84: p. 984-988.

[34] Vogler, M., et al. Low-viscosity and fast-curing polymer system for UV-based nanoimprint lithography and its processing. 2007: SPIE

[35] Stager, B., M.T. Gale, and M. Rossi. Replicated micro-optics for automotive applications. 2005: SPIE.

[36] Rudmann, H. and M. Rossi, Design and fabrication technologies for ultraviolet replicated micro-optics. Optical Engineering, 2004. 43(11): p. 2575-2582

[37] Balmer, T.E., et al., Diffusion of Alkanethiols in PDMS and Its Implications on Microcontact Printing. Langmuir, 2005. 21(2): p. 622-632.

[38] Kraus, T., et al., Printing Chemical Gradients. Langmuir, 2005. 21(17): p. 7796-7804

[39] Bergmair, I., et al., Equalising stamp and substrate deformations in solid parallel-plate UV-based nanoimprint lithography. Microelectronic Engineering, 2008. 85(2008): p. 822-824.

[40] Hiroshima, H., Photo-Nanoimprinting Using Sample-on-Flexible-Thruster Stage. Japanese Journal of Applied Physics, 2006. **45**(6B): p. 5602–5606

[41] He Gao, et al., Air Cushion Press for excellent Uniformity, High Yield and Fast nanoimprint Across a 100 mm Field. Nano Letters, 6, 2438 (2006)

[42] Sotomayor Torres, C.M., ALTERNATIVE LITHOGRAPHY, ed. C.M.S. Torres. 2003

[43] Mühlberger, M., et al., A Moiré method for high accuracy alignment in nanoimprint lithography. Microelectronic Engineering, 2007. 84: p. 925-927

[44] Jae-Hwang, L., et al., DiffractedMoiré fringes as analysis and alignment tools for multilayer fabrication in soft lithography. Applied Physics Letters, 2005. 86(20): p. 204101

[45] Fuchs, A., et al., Interferometric in situ alignment for UV-based nanoimprint. Journal of Vacuum Science & Technology B, 2004. 22: p. 3242-3245

[46] Li, J. and F. Martin. Accurate alignment technique for nanoimprint lithography. 2005: SPIE

[47] Zhang, W. and S.Y. Chou, Multilevel nanoimprint lithography with submicron alignment over 4 in. Si wafers. Applied Physics Letters, 2001. 79(6): p. 845-847

[48] Molecular Imprints Inc., www.molecularimprints.com

[49] McMackin, I., et al., Patterned Wafer Defect Density Analysis of Step and Flash Imprint Lithography, EIPBN 2007, available at http://www.molecularimprints.com/NewsEvents/ tech_articles/new_articles/EIPBN2007_defects.pdf

[50] I. Bergmair et al., submitted to Microelectronic Engineering

[51] Wu, W., et al., Midinfrared metamaterials fabricated by nanoimprint lithography. Appl. Phys. Lett., 2007. 90: p. 63107.

[52] Chen, L., et al., Large flexible nanowire grid visible polarizer made by nanoimprint lithography. Appl. Phys. Lett., 2007. 90(6): p. 063111.

[53] Colburn, M., et al. Step and Flash Imprint Lithography for sub-100nm Patterning. in SPIE's 25th Intl. Symp. Microlithography: Emerging Lithographic Technologies III. 2000. Santa Clara, CA

[54] Kuniaki, I., et al., Organic light-emitting diodes with photonic crystals on glass substrate fabricated by nanoimprint lithography. Appl. Phys. Lett., 2007. 90(11): p. 111114.

[55] Glinsner, T., et al., Fabrication of 3D-photonic crystals via UV-nanoimprint lithography. Journal of Vacuum Science & Technology B, 2007. 25: p. 2337-2340.

[56] Heptagon Oy, www.heptagon.fi

[57] EV Group, www.evgroup.com

[58] EVGroup press release, July 14 2008, http://www.evgroup.com/de/about/news/IQAligner_uv-nil_heptagon/

[59] Kim, M.-S., et al., Flexible conjugated polymer photovoltaic cells with controlled heterojunctions fabricated using nanoimprint lithography. Applied Physics Letters, 2007. 90(12): p. 123113.

[60] Park, S.-H., et al., Effective fabrication of three-dimensional nano/microstructures in a single step using multilayered stamp. Applied Physics Letters, 2006. 88(20): p. 203105.

[61] Schmid, G.M., et al., Implementation of an imprint damascene process for interconnect fabrication. Journal of Vacuum Science & Technology B: 2006. 24(3): p. 1283-1291.

[62] Eliason, M.T., et al., Nanoimprint fabrication of polymer cell substrates with combined microscale and nanoscale topography. Journal of Vacuum Science & Technology B2007. 25(4): p. L31-L34.

[63] Charest, J.L., et al., Polymer cell culture substrates with combined nanotopographical patterns and micropatterned chemical domains. Journal of Vacuum Science & Technology B, 2005. 23: p. 3011-3014.

[64] W. Schwinger, et al., Fabrication of nano-gold islands with µm spacing using 2.5 dimensional PDMS stamps, Microelectronic Engineering 85 (5-6) 2008 1346-1349

[65] Kraus, T., et al., Printing Chemical Gradients. Langmuir, 2005. 21(17): p. 7796-7804.

[66] Hitachi Global Storage, http://www.hitachigst.com/hdd/research/storage/pm/index.html

[67] Glinsner, T., et al., Nanoimprint lithography enables patterned tracks for high-capacity hard disks. Solid State Technology, 2005. March.

Tailoring Carbon Nanostructures: Unraveling the Electronic Properties of Low-Dimensional Quantum Solids

Thomas Pichler

Faculty of Physics, University of Vienna, 1090 Vienna, Austria

The presentation will give an overview on our current research focus on the electronic properties of low dimensional quantum solids. These properties are strongly influenced by basic correlation effects. Archetypical examples of these systems are graphene, graphite and single wall carbon nanotubes (SWCNT) which are determined by the local arrangement of their sp^2 hybridized carbon atoms, such that their character is either semi-metallic, insulating, semiconducting or metallic. Examples of the recent work on how one can analyze these electronic properties using high energy spectroscopy (electron energy-loss, photoemission and x-ray absorption spectroscopy) as a probe will be presented. Special emphasis will be given to the influence of basic correlation effects and local field corrections on the electronic properties of graphene, graphite and SWCNT. The latter exhibit for metallic tubes a Luttinger liquid behavior.

Furthermore, an overview on how to functionalize nanotubes in order to tailor their electronic structure will be given. This includes examples for the three alternative doping routes, namely, substitution, intercalation and endohedral doping (e.g. by filling with fullerenes and metallocenes) as well as examples for the growth of defined innertubes from the different precursors via a thermal nanochemical reaction. In comparison to graphite intercalation compounds, the electronic structure of doped graphene will be unraveled and for metallic functionalized nanotubes doping induced changes will be discussed in the framework of a dimensionality crossover which causes a change from a one-dimensional metal to a normal Fermi liquid. The detailed understanding of these fundamental electronic properties of functionalized graphite, SWCNT and graphene is key to their future success.

Novel Device Concepts and Strategies Basing on SiGe Nanostructures

Detlev Grützmacher

Institute for Semiconductor Nanoelectronics, IBN1, Forschungszentrum Jülich, Germany

The development of the CMOS technology in the last decade has shown that classical materials in CMOS technology materials and device principles have been exhausted, long before the ultimate physical limits have been reached. As a consequence, some materials such as HfO_2 as gate dielectrics and Cu as interconnect metal, which have been off limits only a few years ago, have already entered the major Si device fabrication facilities. Today, additional materials are being investigated, with a particular emphasis on hybrid systems as well as on surfaces and interfaces. While further downscaling in combination with intensified research on hybrid systems will permit the continuation of the CMOS technology path for the next 10 to 15 years, radically new approaches are required for the "beyond-CMOS" scenarios, including device principles and matching architectures.

The introduction of Ge into Si technology permits the modification of the structural, mechanical and electrical properties. Thus the implementation of Ge into Si technology leads to the design of novel devices as well as to new routes for the fabrication of nanostructures. A central challenge for nanotechnology aiming towards nanoelectronics, nanomechanics, biochemical sensors and nanophotonics is to implement exact control in the positioning and size of semiconductor nanostructures. Here, we focus on the templated self-assembly of SiGe nanostructures and discuss two pathways for the fabrication of them.

Templated self-organization of Ge dots is achieved by patterning Si substrates by extreme ultra-violet interference lithography (EUV-IL) using diffractive optics. This method offers fast large area exposure of templates with close to perfect periodicity. Si substrates have been patterned with 2-dimensional hole arrays using EUV-IL and reactive ion etching. Subsequently, molecular beam epitaxy was employed to grow Si/Ge quantum dot stacks. This process allows the fabrication of 2- and 3-dimensional quantum dot crystals containing Ge dots in a Si host crystal of unmatched structural perfection as proven by X-ray diffractometry. The Ge dots exhibit a remarkably narrow size distribution and close to perfect ordering. 2-d ordered quantum dot arrays with lateral periodicities of 50 – 100 nm as well as stacking of those quantum dot arrays into 3-d quantum dot crystals with a vertical periodicity of < 10 nm have been investigated. The results were interpreted by comparison with model calculations using nextnano3.

In the second approach Si/SiGe as well as Si/SiGe/Cr hybrid layered structures are patterned by standard lithographic techniques into mesa structures. Underetching of the mesa structures leads to a scrolling of the layer stacks into nanotubes, nanospirals and other 3-d objects due to the strain. Thus, by this technique nanostructures are produced from templates in a self-assembled fashion. The mechanisms controlling the scrolling process were analyzed in detail and their dependence on the shape, the orientation and the size of the mesa pattern was determined. Moreover, the mechanical

properties of tubes, spirals and rings have been studied. Individual structures have been cut off from the substrate by micromanipulation and were subject to analysis.

Possible applications for quantum dots and scrolled nanotubes for nanoelectronic devices and nano-electromechanical systems will be discussed.

Novel Materials and Devices (Talks)

Solution-Processable Electronics

Peter Hadley

Institute of Solid State Physics, TU Graz

In ambient intelligence applications, the environment is filled with sensing elements, communication elements, and display elements. All of these require solution processable electronics that can be printed cheaply on substrates like plastic, cloth, or paper. Solution-processable semiconductors often have a complicated microstructure that has been difficult to control and to understand. However, our ability to determine and control the microstructure is rapidly improving. The Institute of Solid State Physics at the TU Graz has a strong program on organic semiconductors and their use in sensors, light emitting diodes, lasers, and transistors. Roland Resel described the structure of a self-assembled layer of molecules that form the channel of a transistor. His collaborators at Philips have made integrated circuits consisting of hundreds of these transistors. In Nature Photonics, a team lead by Emil List and Joachim Krenn explained how metal nanostructures can be used to efficiently extract and manipulate light from organic light emitting diodes. The fundamental crystal growth mechanisms of large organic molecules recently appeared in Science in a paper by Adolf Winkler and his collaborators in Leoben. The inside cover of the August 18th issue of Advanced Materials features an organic transistor that can be used as a chemical sensor. This transistor and its chemically active layer were built studied by Egbert Zojer and his team. The papers mentioned here represent the best of a broad effort in solution processable electronics that will contribute to the development of distributed sensors, electronic books, lighting panels, displays, solar cells, and RFID technologies. Strategies will be discussed for using inorganic materials (including silicon) in solution based processes.

Engineering of Dielectric Materials for Silicon Technology

Lothar Frey

Fraunhofer Institut für Integrierte Systeme und Bauelementetechnologie, Schottkystrasse 10, 91058 Erlangen

Scaling of electronic devices, especially of CMOS devices, follows Moore's law for more than two decades. But today, severe difficulties related to fundamental physical effects in ultra thin layers and small lateral structures have emerged. Among them are increased leakage currents and fast degradation of device parameters. One approach to overcome these problems is the introduction of new materials with specific tailored properties. Therefore, silicon technology, which was built on a rather restricted set of materials, has opened itself to a variety of new materials.

The most prominent case is probably the replacement of the gate dielectrics, silicon dioxide, by so called high k materials. In this talk, the problems related to the introduction of these new high-k materials will be discussed. The permittivity of high-k layers like Hf, Zr, or Ti based oxides is the driving force to use them in CMOS transistors to increase device performance like current drive. But in order to utilize those layers, many other problems occur and have to be solved. Examples are threshold voltage shift, mobility degradation, or parameter instability. Also new process steps like Atomic Layer Deposition had to be introduced and developed, mainly to control interfaces on sub-monolayer scale. Today, new high-k dielectrics are engineered materials with tailored properties for specific applications. High-k based gate stacks require well controlled interface and layer formation to ensure high carrier mobility, low and symmetrical threshold voltages, and tolerable degradation. After discussing this approach for MOS transistors, the application of tailored high-k dielectrics in DRAM capacitors and Flash memory cells will be shown. In DRAM capacitors, leakage current and dielectric integrity are the main issues to be engineered. On the other side, floating gate flash memory cells require controlled band alignment and low parasitic trapping in order to improve device performance.

Finally, a short outlook will show that new materials, engineered for specific electronic parameters, will open a variety of new option for scaling of classical devices as well as for heterogeneous integration of electronic components.

New Materials and Devices for Future Generation CMOS Technologies

S. Abermann, C. Henkel, O. Bethge, G. Pozzovivo, J. Kuzmik, D. Pogany, and E. Bertagnolli

Institut für Festlörperelektronik, Technische Universität Wien, Floragasse 7, A-1040 Wien

Introduction

New materials and devices will be needed to continue the performance scaling for future generation CMOS technologies. The introduction of high mobility channel materials (e.g. Ge, strained Si, and III/V) on a Si-based platform, or the implementation of high-*k* and metal gate materials into the MOS-stack will be necessary to achieve the scaling goals as given in the International Technology Roadmap for Semiconductors (ITRS) [1]. In general, the transistor performance can be enhanced by (i) reducing the channel length (scaling), (ii) increasing the carrier mobility μ, or by (iii) reducing the oxide thickness (increasing C_{ox}). New materials and device concepts are necessary to address the concepts mentioned above. Point (i) is still realized by the classical scaling approach, but in future technology generations new device geometries such as FinFETs or nanowires may be of advantage (see also Fig. 1); (ii) μ can be increased by using strain and high-mobility channel materials, and (iii) is already in production at Intel© by introducing the high-*k*/metal gate approach [2]. In this work, we present an overview of such materials and devices, including high-*k*/metal gate technology on high-mobility substrates such as Ge or strained Si, as well as new device geometry concepts.

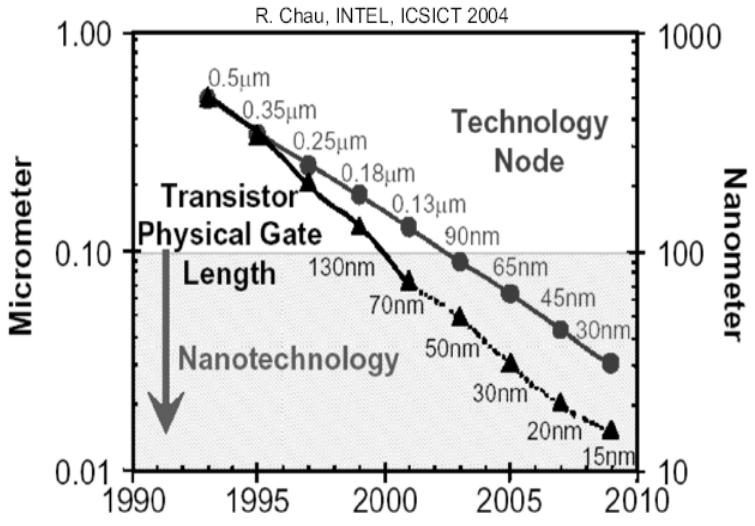

Fig. 1: Transistor physical gate length and technology node as a function of year of introduction (From R. Chau, INTEL, ICSICT 2004).

Experimental

We apply Atomic Layer Deposition (ALD) or Metal-Organic Chemical Vapor Deposition (MOCVD) to grow ultra-thin films of oxides such as Al_2O_3, ZrO_2, La_2O_3, HfO_2, and ternary oxides or oxide stacks of these. In some cases, the fabricated dielectric stacks are subjected to a post deposition anneal (PDA) in nitrogen- or argon-atmosphere. Metal electrodes, such as Aluminum (Al) or platinum (Pt) are deposited by ALD or sputter deposition, and patterned by optical lithography including lift-off technique or by wet-chemical etching. Some devices are then subjected to a post metallization anneal (PMA) in forming gas atmosphere. The finalized stacks or devices are characterized by physico-chemical or electrical measurement techniques. More details on the experimental and on the measurement procedures, as well as on the results that are exemplary given beneath can be found in [3] – [6].

Results

Silicon Substrates

In Fig. 2 measured leakage current density values at –1 V (accumulation regime) of MOS capacitors incorporating Al-gates and various oxide/semiconductor stack types are compared. All samples have been subjected to a PDA at various temperatures ranging from 400 °C to 800 °C, and a PMA at 425 °C. Regarding the single ternary oxides $La_xAl_yO_z$ and $La_xZr_yO_z$ (not shown), $La_xAl_yO_z$ exhibits clearly superior insulation properties compared to $La_xZr_yO_z$. If we introduce a thin layer of Al_2O_3 either at the bottom or the top, leakage currents are clearly reduced. The best leakage currents are achieved if the ternary oxide is sandwiched in between to thin layers of Al_2O_3. Additionally, from Fig. 4 we can learn that the following measures have a positive impact on the leakage current: (i) increasing the PDA-temperature, (ii) reducing the amount of La_2O_3 in the ternary oxides, and (iii) increasing the thickness of the single films. Point (i) is most likely due to an increased and more SiO_2-containing interfacial layer at the oxide/Si-substrate interface. Point (ii) indicates that the La_2O_3 ALD-process seems to be problematic, and point (iii) is due to reduced conductance mechanisms like tunnel- or Frenkel-Poole emission.

Germanium Substrates

The I-V measurements, shown in Fig. 3, indicate that lowering of the ALD deposition temperature from 300 °C to 150 °C yields lower gate leakage currents of about one order of magnitude. There are two possible explanations for this behavior: first, (i) much longer purge times during the ALD growth at lower deposition temperatures (see also Table 1) strongly increase the process time, and therefore enlarge possible diffusion times for oxygen, which may lead to a stronger GeO_x regrowth at the germanium/oxide interface. Second, despite of the thinness of the films an increased polycrystalline amount in the ZrO_2 layer at higher deposition temperatures may exist, and therefore generate a larger quantity of leakage paths across the oxide. All dielectric stacks exhibit a breakdown in the range of 3 V to 4 V gate bias with corresponding leakage current of >1 A/cm^2, except of the samples with HBr pre-treatment, whereat the breakdown occurs not until bias voltage has been driven to about 6 V. We believe that this remarkable result is correlated to the entire removal of the sub-oxide. For silicon, it has been reported that a thin interfacial SiO_2 layer is the origin of breakdown of high-k dielectric stacks. Assigned to our results, a thin interfacial GeO_x layer yields to a breakdown of the dielectric stacks at lower gate bias voltage compared to stacks deposited on a GeO_x-free germanium substrate.

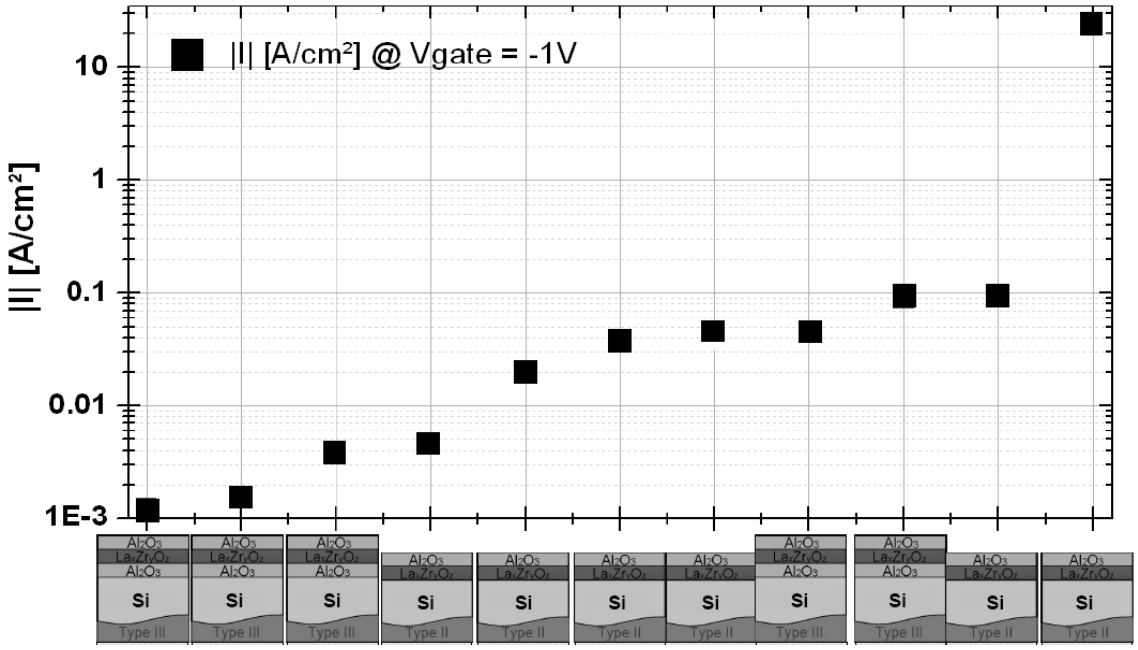

Fig. 2: Gate leakage current density values at –1V (accumulation regime) gate bias of MOS capacitors incorporating Al gate electrodes, p-Si substrates and various gate dielectrics. Every value corresponds to one gate stack type that is schematically shown at the bottom.

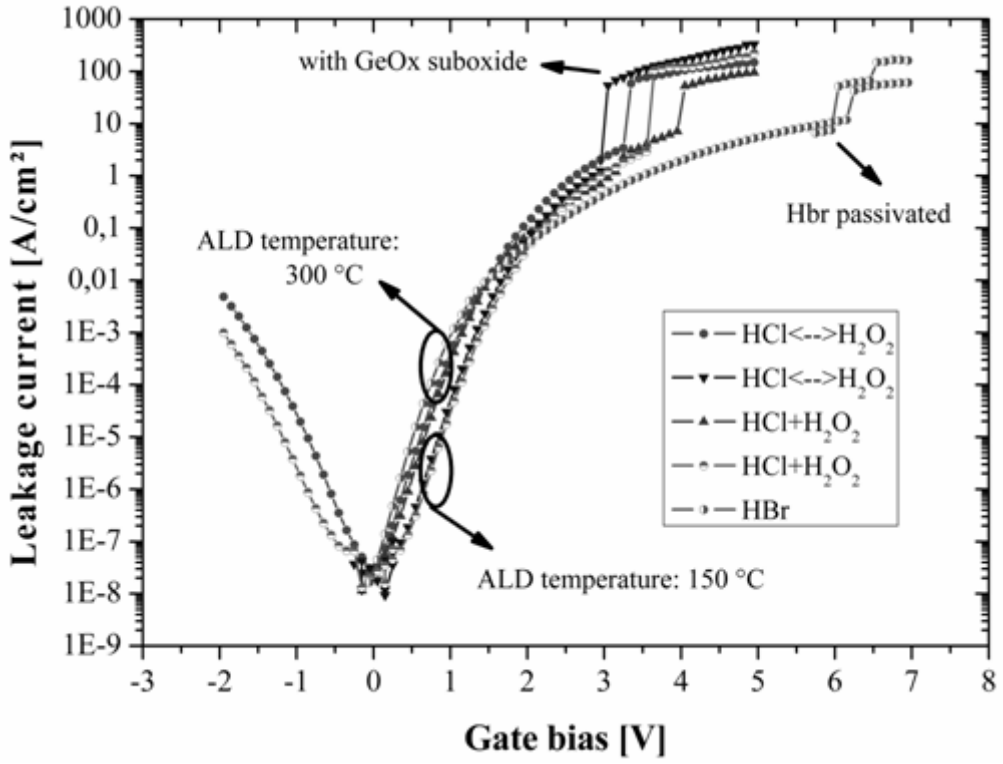

Fig. 3: FTIR spectra of the sample in Fig. 2 in the frequency range of the carbon-related local vibration modes. With increasing annealing time more and more carbon moves from substitutional into SiC sites.

Top-Down Vertical Nanowire Transistor with High-*k*/Metal Gate

Figure 4 summarizes a new device concept based on a top-down etching approach of Si nanowires. The Ni-dots serve as a hard mask to etch the wires out of the Si wafer as well as the top contact. The etched wires are capped by ALD deposited Al_2O_3 and Pt forming the gate stack. The advantage of this method is that well structured patterns of a distinct number of devices can be fabricated, which determine the obtained current of one pattern as shown in the upper left image of Fig. 4.

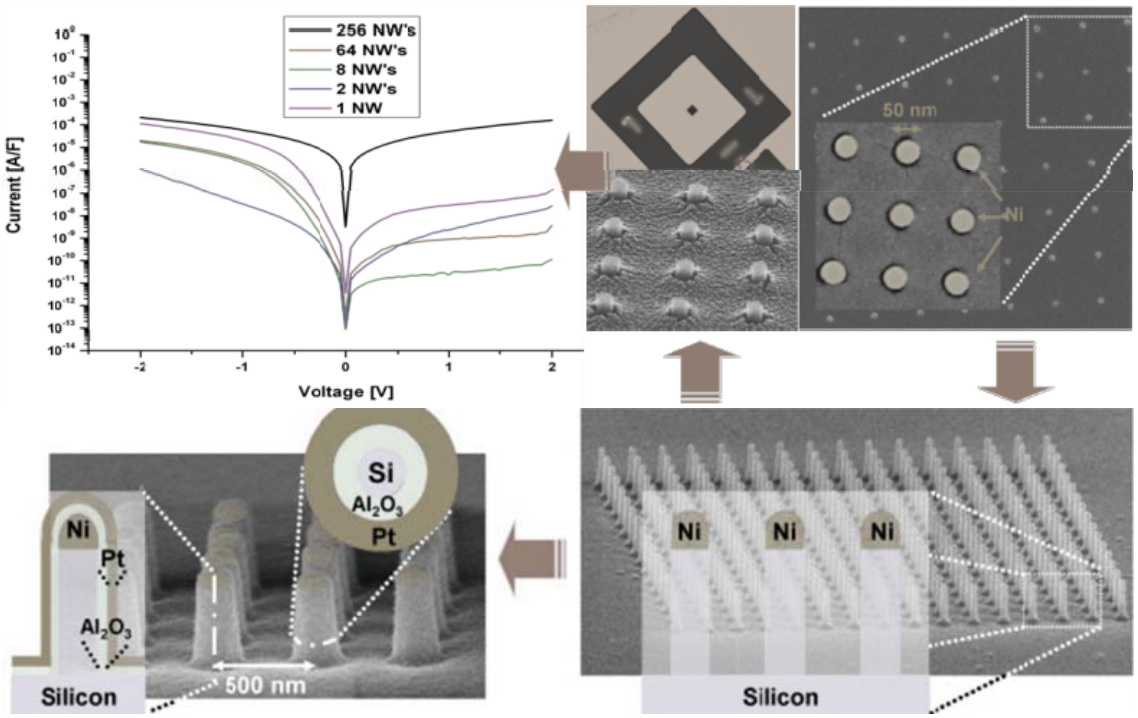

Fig. 4: Top-down vertical nanowire transistor device concept with high-k/metal gate technology deposited by ALD.

Conclusion

An overview of materials and devices, including high-*k*/metal gate technology on high-mobility substrates such as Ge or strained Si, as well as new device geometry concepts has been given.

References

[1] International Technology Roadmap for Semiconductors, http://www.itrs.net/

[2] K. Mistry et al., INTEL, IEDM 2007

[3] S. Abermann et al., Semicond. Sci. Technol. 22, 1272-1275, (2007)

[4] S. Abermann et al., J. Electrochem. Soc. 156, G53, (2009)

[5] O. Bethge et al., ECS Transactions: Physics and Technology of High-k Gate Dielectrics 6, 365-373 (2008)

[6] C. Henkel et al., ECS Transactions: Physics and Technology of High-k Gate Dielectrics 6, 195-201 (2008)

Investigations on the Wetting Layer and the Island Nucleation in the SiGe System on Planar Si(001) Substrates

M. Brehm, M. Grydlik, H. Lichtenberger, N. Hrauda, T. Fromherz, F. Schäffler, and G. Bauer

Institut für Halbleiter- und Festkörperphysik, Johannes-Kepler-Universität Linz, A-4040 Linz

In this work investigations on the Ge profile along the growth direction in SiGe wetting layers (WL) grown on Si(001) substrates are presented. The high relative resolution (0.025 monolayer) of the sample series is used to monitor the dependence of the WL photoluminescence (PL) transition energies on the amount of deposited Ge. Fitting **k·p** band structure calculations to the almost linear confinement shift provides for the first time reliable quantitative Ge profiles in the WL. The importance of the Ge content and thus the strain in the WL on the island nucleation is shown.

Introduction

Due to its relative simplicity the SiGe system has acted as model system for understanding the hetero epitaxial growth of semiconductor nanostructures. Ge on Si (lattice mismatch of 4.2%) grows in the Stranski-Krastanow mode. Ge forms within the first monolayers of growth a thin film on the Si (001) surface, adapting the inplane Si lattice constant. As the Ge film grows thicker the strain energy in the Ge film is either reduced by plastic relaxation, leading to dislocation nucleation, or by elastic relaxation, relieving the strain by island formation. However, despite the huge research efforts fundamental properties like Ge concentrations in the WL that influence the strain in the Ge film are not quantitatively known. The atomic force microscopy (AFM) images in Fig. 1 highlight the influence of increased intermixing and thus strain at higher growth temperatures (T_G). For these samples, 6 ML of Ge were grown at different T_Gs, ranging from 500 °C to 750 °C. At elevated temperatures the SiGe intermixing becomes enhanced and therefore the strain in the layers is reduced. This leads to a drastic increase of the WL thickness and the island sizes which, as a consequence has a large influence on the optical and electrical properties of such islands.

Experimental

The samples used for determination of the WL profiles were grown by solid source molecular beam epitaxy (MBE) on 4 inch Si(001) wafers. A 450 Å thick Si buffer layer was grown at a rate of 0.6 Å/s while the substrate temperature was ramped up from 450 °C to 550 °C. Only for the subsequent deposition of Ge (growth rate: 0.05 Å/s, growth temperature: 700 °C), the substrate rotation was turned off to implement a shallow, monotonous gradient of deposited Ge across the wafer. The local variation of the deposited Ge was determined by x-ray measurements on reference samples, and varies linearly from -20% to +20% across the wafer with respect to the nominal value in the wafer center. Three series of samples were prepared for PL experiments, which received 500 Å thick capping layers deposited at a rate of 1Å/s and deposition temperatures (T_c) of 300, 500 and 700 °C, respectively. For the PL investigations the wafers were cut into

pieces along the Ge gradient, and up to 75 PL spectra per wafer were taken at 4.2 K. PL was excited with an argon ion laser operating at 514.5 nm with 1 W/cm^2.

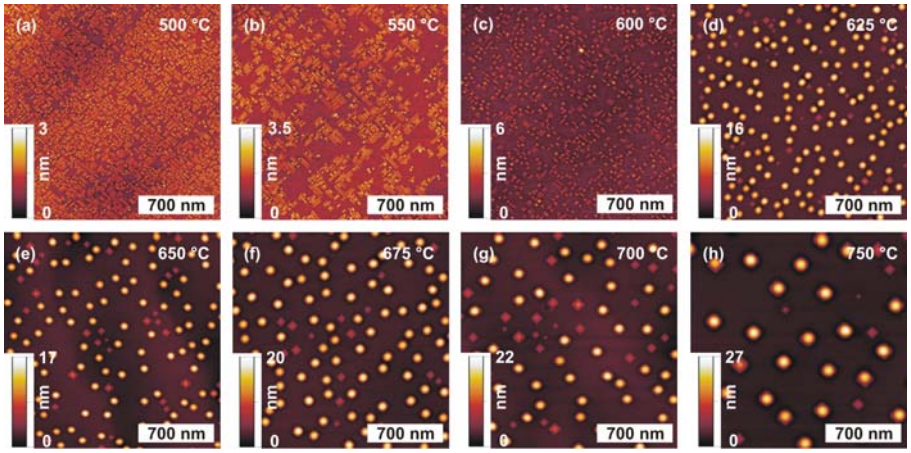

Fig. 1: AFM height images of Ge islands, deposited at different temperatures. (a) T_G = 500°C, (b) 550°C (c) 600°C (d) 625°C (e) 650°C (f) 675°C (g) 700°C and (h) 750°C. Despite the abrupt transition from (105) facetted hut clusters to the bi-modal pyramid-dome distribution between 600°C and 625°C, the increase of the island sizes with increasing T_G due to increased intermixing is obvious.

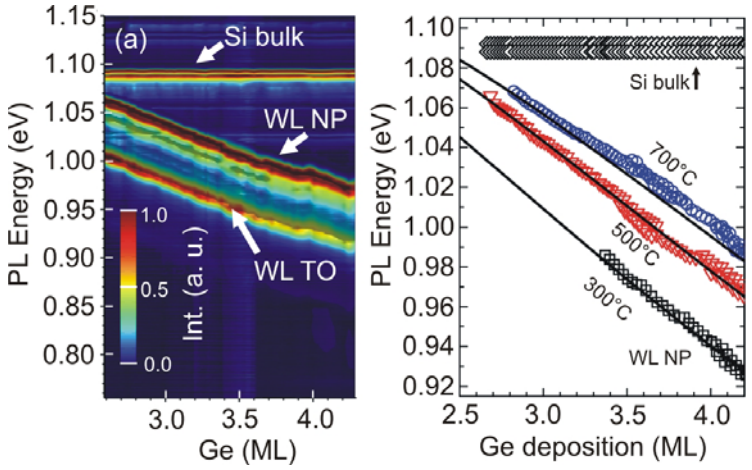

Fig. 2: (a) Dependence of the PL energies on the deposited amount of ML of a sample series grown at 700 °C and capped at 500 °C. The corresponding intensities of the WL and substrate peaks are color coded (b) Black open squares, red open triangles and blue open circles correspond to different T_cs of 300 °C, 500°C and 700°C. The Ge WL was deposited at 700°C for all samples. The black solid indicate the fitted confinement shift for the WL Ge profiles shown in Fig. 4.

Results

In Fig. 2 (a), normalized PL spectra are shown for the samples with at T_c = 500 °C. The WL emits characteristic quantum well (QW) PL bands consisting of a spectrally narrow no-phonon (WL NP) line and its split-off Si-Si TO phonon replica, (WL TO^{Si-Si}). With Ge coverage increasing from 2.6 ML to 4.3 ML, the WL bands shift to lower energies, be-

cause the confinement energy decreases with increasing WL thickness. Due to the shallow gradient of the Ge coverage across the wafers, the shift could be monitored with the extremely high resolution of 0.025 ML. Figure 2 (b) summarizes from a set of 10 wafers the dependence of the WL_{NP} energies on Ge coverage for the three investigated T_c's. A virtually linear decrease of the WL PL peak position with Ge coverage is observed for each T_c. Figure 2 (b) shows that the WL_{NP} peak positions shift to higher energies with increasing T_c. Since the WL was deposited under identical conditions on all samples, the observed shift of the WL_{NP} line indicates increased intermixing of the WL with increasing T_c. To determine the WL composition profile, and its dependence on T_c, we compared the PL results with band structure calculations. Since the band alignment of SiGe on Si(001) is of type II, only holes are confined to the WL. We calculated the heavy hole (HH) ground states in the WL on the base of a one band **k·p** envelope function model including the strain in the WL. Thus, the only two parameters, the HH effective confinement mass m_{HH}, and the valence band (VB) offset ΔV_{HH} enter [1]. The resulting values for m_{HH} decrease with only a small bowing from 0.276 m_o for pure Si to 0.223 m_o for $Si_{0.5}Ge_{0.5}$, and to 0.18 m_o for pure Ge. ΔV_{HH} increases linearly from 0 for pure Si to 720 meV for pure Ge. The WL_{NP} PL transition energy is calculated from the HH ground state energy by subtracting the energy difference between the HH ground state in the WL and the HH VB edge of bulk Si from the fundamental Si band gap. The seemingly linear slopes of the transition energies are due to the extremely narrow WL, which leads to ground state energies approaching the rim of the valence band QW.

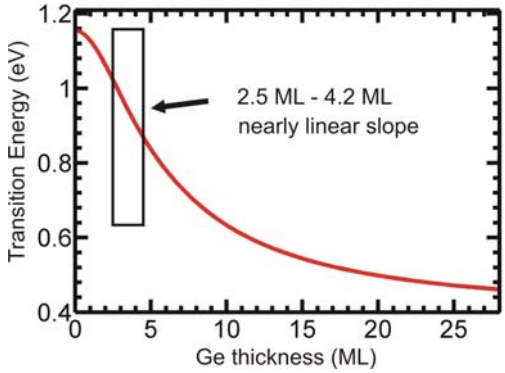

Fig. 3: Dependence of the transition energy on the thickness of a square quantum well with 100% Ge.

As shown in Fig. 3, at around 5 ML WL thickness, the thickness dependence of the WL PL energy shows vanishing curvature between the pinning to the QW rim and a $1/d_{WL}^2$ variation for QWs with large thickness d_{WL}. For a more realistic Ge profile, segregation and diffusion at both WL interfaces were taken into account. Four fitting parameters were used to model the shape of the hole-confining potential (i) The maximum Ge content x_{max} in the well, (ii) Si segregation at the lower interface, (iii) Ge segregation at the upper interface and (iv) Ge bulk diffusion, which is virtually negligible at the used T_cs. The observed blue shift of the WL PL energies with increasing T_c can only result from intermixing of the Ge WL with the Si cap due to segregation. For the high Ge concentrations in the WL, surface segregation results in an exponential composition profile at each interface with decay lengths λ_1 and λ_2 for the bottom and top WL interfaces, respectively. λ_1 was kept constant, because the lower interface was grown at 700 °C for all samples. λ_2 was varied with the cap deposition temperature T_c. In addition, a small amount of Ge bulk diffusion was allowed to smear out the sharp features in the concentration profiles. Good fits of the slopes for all T_c's (Fig. 2 (b)) could only be achieved for non-vanishing bulk diffusion length, and decay length λ_1. However, variations of L and

λ_1 within a realistic range of 0.5 Å < L < 2.5 Å and 0.1 < λ_1 < 0.3 have only negligible influence on the calculated binding energies of the WL quantum well. In the following, we used L = 1.3 Å and λ_1 = 0.25 Å. The two remaining fitting parameters are then x_{max}, and the segregation constant for the top interface, λ_2. The resulting Ge profile was used to calculate the spatial variations of strain and the HH valence band edges, the respective ground state energy in these potentials and the PL transition energies. The results shown by the solid lines in Fig. 2 (b) were obtained with x_{max} = 0.86 ± 0.01 and λ_2 = 1; 3.7; 4.8 Å for T_c = 300; 500; 700 °C. We want to point out, that by adjusting λ_2 only, both the change of the slopes and the relative positions of the three traces in Fig. 2 (b) are in excellent agreement with the experiment.

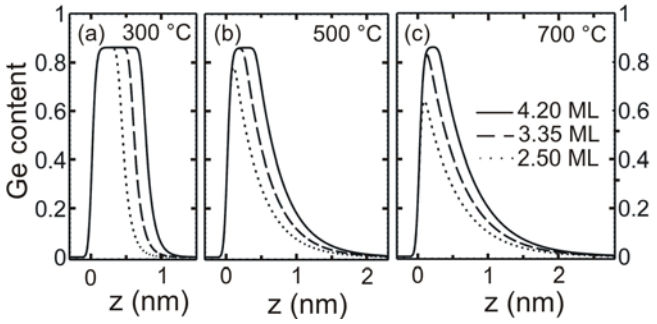

Fig. 4: Calculated Ge profile across the WL for T_c's of (a) 300 °C, (b) 500 °C and (c) 700 °C for the different Ge coverages indicated in the plot. The parameters for the calculated Ge profiles are: x_{max}= 0.86, L=1.3 Å, λ_1 = 0.25 Å, and λ_2 = 1; 3.7; 4.8 Å in (a), (b) and (c), respectively.

In Fig. 4, the results for the Ge profiles are shown for the three investigated T_c values. At T_c = 300 °C, an almost box-like Ge profile is obtained, indicating negligible Ge segregation. Increasing T_c to 500 °C and 700 °C results in enhanced Ge segregation, as indicated in Figs. 4 (b) and (c) by the decaying Ge profiles. The large value obtained for x_{max} evidently depends to some extent on the alignment of the Si and SiGe valence bands in the calculations. We checked the dependence of the result for x_{max} on the valence band alignment ΔV_{HH} and obtained a sensitivity of $\Delta x_{max}/\Delta(\Delta V_{HH}) = 2.4 \times 10^{-3}$ (meV^{-1}).

Conclusion

We have performed a detailed investigation of the dependence of the PL emission of a Ge WL on the amount of deposited Ge. By freezing the substrate rotation during Ge deposition, we were able to study systematically the shift of the WL emission as a function of Ge coverage with 0.025 ML resolution. These data allowed for an unambiguous fit of the observed slopes dE_{WL}^{NP} / dd_{WL} to results of band structure calculations. From these fits we determined quantitative Ge profiles along the growth direction and their dependence on T_c. At T_c = 300 °C an almost box-like Ge profile of the WL is obtained with a maximum Ge concentration of 86%. For Ge coverages > 4.2 ML this large maximum Ge concentration is preserved also in WLs capped at 500 °C and 700 °C.

References

[1] M. Brehm et al., Applied Physics Letters, **93**, (2008)

Opto-Electronics and Photonics (Talks)

LEDs for General Purpose Lighting

Stefan Tasch

Ledon Lighting Jennersdorf GmbH
Technologiepark 10, A-8380 Jennersdorf

Until a few years ago, LEDs were mainly seen as low-power light sources in indicators and advertising. With huge progress being made in terms of device performance, this has profoundly changed.

Especially since the beginning of the 21st century, LED components manufacturers and material suppliers have achieved remarkable progress in their endeavor to increase chip performance, phosphor efficiency and overall device efficiency, resulting in increased luminous efficiency (lm/W), high reliability / lifetime, high color rendering etc., making solid state lighting (SSL) not only feasible for professional lighting such as displays, signage, indicators, architectural, surgical and automotive applications, but bringing it closer to enter the general lighting market with applications such as home, office, and retail lighting.

In indoor applications, fluorescent lamps are still standard, with an efficiency of 80 – 90 lm/W; however, LEDs are catching up quickly. While the efficiency of standard high-power white LEDs on the market is about 40 – 70 lm/W, efficiencies of >100 lm/W have been achieved, and LEDs with an efficiency comparable to fluorescent lamps are to enter mass production.

Besides energy saving, one big advantage of LEDs is their tunability of the color temperature. For instance, for RGB-devices, the color locus can be varied anywhere within the color gammut by independently controlling the current for R, G, and B. Furthermore, it is recognized that color rendering and color temperature have a physiological influence on humans. A combination of a blue LED with green and red phosphors would cover most of the visible spectrum and can achieve color rendering indices (RA8) of well over 90. By combination of warm and cold white devices with the appropriate drivers and sensors, it is possible to automatically adjust the color temperature with daytime and season (cold white in summer/daytime, warm white in winter/evening). Due to the potential of miniaturization, LEDs have a considerable advantage over other light sources for including optics and achieving well-defined emission angles and shapes, which would not be possible with big-sized fluorescent lamps.

Photonic Engineering of Intersubband Devices

S. Schartner, E. Mujagić, L.K. Hoffmann, M. Nobile, H. Detz, P. Klang, A. M. Andrews, W. Schrenk, and G. Strasser

Zentrum für Mikro- und Nanostrukturen, TU Wien, Floragasse 7, A-1040 Vienna, Austria

Photonic cavities play a crucial role when engineering laser as well as detector elements. In the particular case of intersubband optoelectronic devices they are essential for light in- and out-coupling. We discuss three novel realizations of optical cavities that are used for a quantum well infrared photodetector (QWIP) and quantum cascade lasers (QCLs). Photonic crystals are employed for QWIPs in order to investigate their feasibility as a resonant detection scheme. A new waveguide design was developed that increases the coupling efficiency of a distributed-feedback (DFB) grating and hence allows fabricating ultra-short surface emitting DFB QCLs. Finally we have realized ring shaped DFB lasers that naturally exhibit a circularly shaped far field. Moreover, single-mode surface emitting ring QCLs have a reduced divergence of only 3° in either direction.

Introduction

Intersubband (ISB) transitions in the conduction band of III-V semiconductors are used to realize optoelectronic devices in the mid-IR (3 – 25 µm) as well as in the THz region (60 – 200µm). Quantum cascade lasers (QCLs) being intersubband based lasers have undergone tremendous progress since their invention in 1994 and are nowadays close to their exploitation in real world applications like trace gas sensing, spectroscopy or free-space communication. The level of output power is already in the Watt regime with wall plug efficiencies above 10% at room temperature and under continuous wave (cw) operation. Their detector counterparts – quantum well infrared photodetectors (QWIPs) – are also well developed, having several advantages over band gap based detectors like a ultra fast response time enabling transfer rates up to 30 GHz and are mature in growth and processing methods, which makes them interesting applications in the field of thermal imaging.

As a special property of ISB transitions they have a polarization selection: the electric field of the generated/absorbed light has to be polarized normal to the epitaxial layers. In order to realize surface emitters or detectors being sensitive to surface incident light a diffractive element like a grating or a photonic crystal (PhC) is required, which places an additional demand on photonic engineering of intersubband devices.

Photonic Crystal Defect States in Intersubband Detectors

As mentioned above, QWIPs have potential applications in thermal imaging. In order to make a single pixel sensitive to surface incident light such multi-pixel arrays usually carry gratings that diffract the light. Using (deep etched) photonic crystals instead of (shallow) gratings would have the advantage of providing a resonant detection. The light is not just redirected and passes the detecting layers one time but it is coupled resonantly into the cavity and the absorption probability can be enhanced. In this way the drawback of QWIPs, namely the inferior signal-to-noise behavior, can be improved.

We therefore started to investigate the properties and technical feasibility of PhC QWIPs. We were able to obtain information about coupling efficiency and its correlation to PhC symmetry, polarization dependence [1] as well as linewidth and the behavior of defect modes [2].

Figure 1 shows a comparison between the measured frequency shift of defect modes and results from a 2D finite-element simulation. The defect states were induced by removing a single hole, and by changing the diameter of the six defect surrounding holes (defect holes) a shift of the resonant frequencies was realized. This frequency shift is negligibly small for small defect holes (r_D < 0.5r) whereas for larger defect holes an almost linear increase is observed. The results enable us to shift the defect mode to a distinct frequency. And probably even more important is the fact that the region with small defect holes is stable over small inaccuracies in the fabrication process. The geometric dependence was also used to identify the peaks with calculated mode profiles.

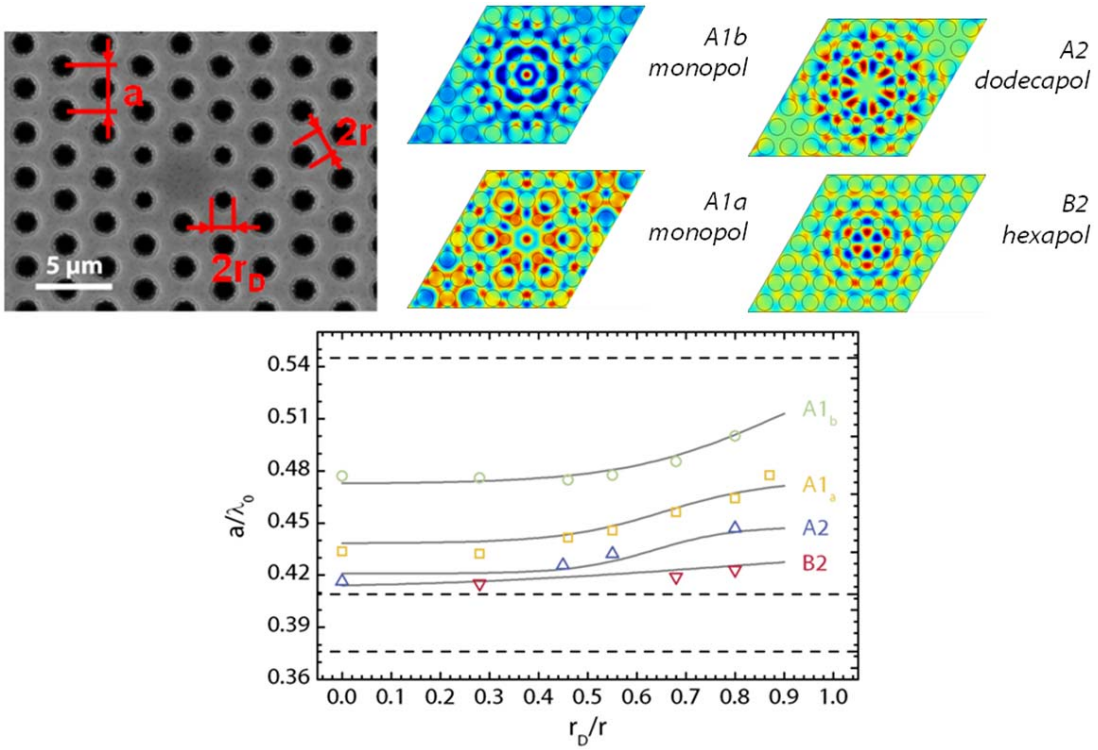

Fig. 1: A scanning electron microscope (SEM) picture with the relevant dimensions of the PhC is shown together with a graph that compares simulated with measured defect modes. The shift was achieved by changing the size of the six defect surrounding holes. Also the mode patterns of the defect modes are shown.

Ultra-Short Distributed-Feedback Lasers

In order to obtain single-mode surface emitting QCLs usually 2nd order distributed-feedback gratings are etched into the surface of ridge lasers. The coupling strength introduced by the grating is determined by the overlap of the waveguide mode with the grating and limits the laser length. Since the overlap is small (~0.2 % → coupling strength ~7 cm^{-1}) lasers have a typical minimum length of around 1 mm. In order to achieve further device minimization we have developed a new type of waveguide that increases the modal overlap.

The small overlap is due to the fact that the grating region is diluted by air and has a low refractive index. This pushes the waveguide mode away from the grating region. In order to overcome this we place a continuous metal layer on top of the grating and an air cladding on the opposite side. In this way the negative effect of the grating is partly compensated since the TM polarized mode is attracted by the metal. In addition the large step in refractive index from the waveguide core to air further improves this effect [3]. Finally we were able to increase the modal overlap with the grating region by roughly one order of magnitude.

The structure was realized by wafer-bonding the pre-structured laser chip grating-down on a gold covered, doped GaAs template. The grating is therefore sandwiched between the laser's active region and the continuous gold layer. The air cladding on the opposite side was fabricated by removing the substrate on the laser chip by selectively wet-etching and subsequent standard laser processing that includes lateral contact stripes leaving out an air window. The light out-coupling takes place via this air window.

The fabricated devices operate in single-mode down to a length of 180 µm being significantly smaller then 1 mm as for standard DFB QCLs. Lasing threshold as well as slope efficiency are comparable to standard DFB lasers and the waveguide design still leaves room for the reduction of loss without sacrificing coupling strength.

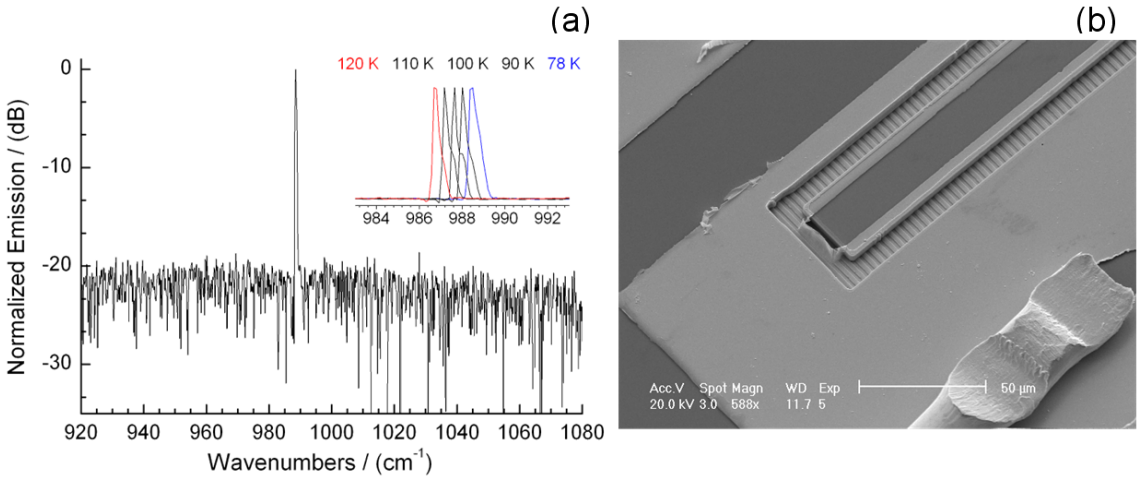

Fig. 2: (a) A single-mode spectrum and the temperature tuning of a 176 µm short DFB QCL fabricated with a combined metal-air waveguide is shown. (b) SEM picture of a finished device. The grating is on the bottom side and can only be seen in the trenches.

Surface Emitting Ring Lasers

A promising concept to address divergence of the output beam is a ring shaped resonator with a radial, light out-coupling grating on top (Fig. 3 (b)). The ring-type emitting area naturally forms a circularly shaped far field and the overall large emission area narrows the beam. The grating is crucial for light extraction via the surface as QCLs are intersubband devices and are therefore restricted to TM polarization. Light propagating normal to the epi-layers – and hence normal to the surface – cannot directly be generated and one needs a diffractive element to realize surface emission. Second order distribute-feedback (DFB) gratings are a perfect choice as they additionally allow for mode selection yielding single-mode surface emitting lasers.

Our group was the first to realize grating coupled, surface emitting ring QCLs in multi-mode [4] as well as in single-mode. [5] Multi-mode devices have a shallow grating that introduces only a small coupling not enough for single mode operation. The emitted far-fields are ring to point shaped, depending on the detuning of the lattice period. If the grating period matches the center of the emission spectrum, the far field forms a single spot with a full-width-at-half-maximum (FWHM) of around 10°. This value is limited by the broadness of the emission spectrum as a slight detuning causes angled emission. Lasing threshold is similar to those of Fabry-Perot type cavities, which is expected as the waveguide loss is unchanged and mirror loss for standard cavity lengths is comparable to out-coupling loss introduced by the grating.

The far fields emitted from single-mode devices show a clearly reduced FWHM below 3° (Fig. 3 (a)). This is due to the spectral narrowing induced by the DFB grating which has a higher coupling coefficient. Along with the increased coupling that leads to single-mode operation also the out-coupling is increased. This influences lasing threshold in a negative way but benefits slope efficiency so that at typical operating currents efficiency is identical to multi-mode devices.

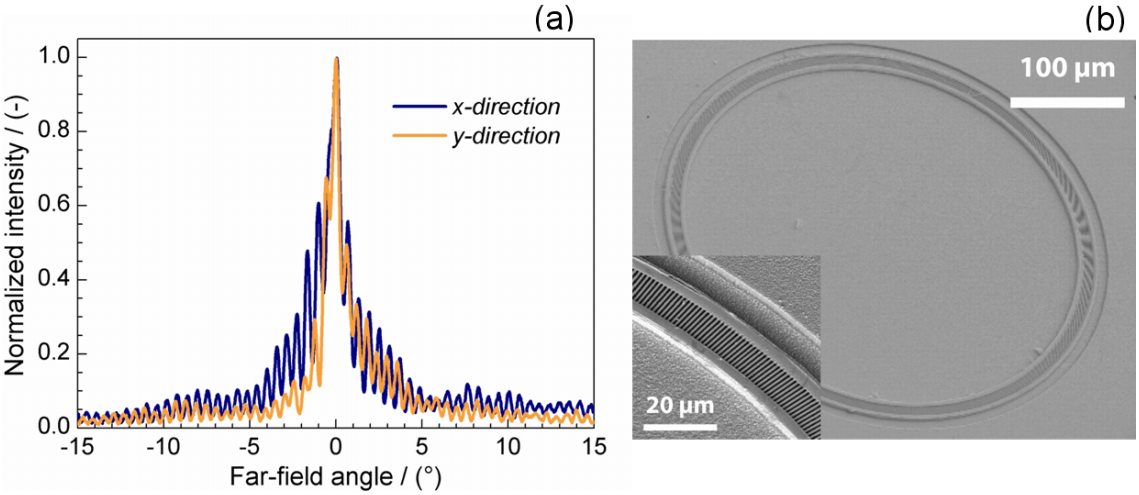

Fig. 3: (a) The far-field of single-mode surface emitting ring QCL has a FWHM of 3°
(b) Top view SEM of a fully processed device.

Acknowledgements

Appart from the GMe we acknowledge partial support by the following projects and agencies: IRON, ADLIS, PLATON, and MNA.

References

[1] S. Schartner et al., *Appl. Phys. Lett.* **89**, 151107 (2006)

[2] S. Schartner et al., *Opt. Express* **16**, 4797 (2008).

[3] S. Schartner et al., *Opt. Express* **16**, 11920 (2008)

[4] E. Mujagić et al., *Appl. Phys. Lett.* **93**, 011108 (2008)

[5] E. Mujagić et al., *Appl. Phys. Lett.* **93**, 161101 (2008)

Spintronics (Talks)

Origin and Control of Ferromagnetism in Magnetically Doped Semiconductors: the Case of (Ga,Fe)N

A. Bonanni, A. Navarro-Quezada, T. Li, M. Wegscheider, B. Faina, R. Lechner, and G. Bauer
Institut für Halbleiter- und Festkörperphysik, Universität Linz – Austria

Z. Matey, and V. Holý
Dept. of Condensed Matter, Charles University, Prague – Czech Republic

W. Pacuski, M. Sawicki, and T. Dietl
Institute of Physics, Polish Academy of Sciences, Warsaw – Poland

The control over the incorporation of magnetic ions into a semiconducting host is fundamental for the functionality of magnetically doped semiconductors. Our magneto-optical data on diluted samples corroborate recent suggestions that the strong *p-d* hybridization specific to nitrides and oxides leads to a significant renormalization of the valence band exchange splitting. Furthermore, through a structural analysis at the nanoscale, we give experimental evidence that the aggregation of Fe ions in (Ga,Fe)N and consequently the magnetic response of the material are affected by the growth rate and doping with acceptors or donors.

Introduction

The comprehensive search for materials exhibiting spintronic functionalities has resulted in the discovery of a number of magnetically doped and nominally undoped wide-band gap semiconductors and oxides exhibiting ferromagnetic features persisting up to high temperatures. The nature of this puzzling robust ferromagnetism has become one of the most controversial topics in nowadays materials science and condensed matter physics [1]. In order to shed new light on the origin of high-T_C ferromagnetism, we have undertaken studies of (Ga,Fe)N [2] – [5] grown by metalorganic vapor phase epitaxy (MOVPE), either undoped or co-doped with Si or Mg, combining magnetic (SQUID and electron paramagnetic resonance), magnetooptical, and x-ray absorption near-edge spectroscopy (XANES) investigations with a comprehensive structural and chemical characterization (secondary ion mass spectroscopy – SIMS, transmission electron microscopy – TEM, electron diffraction spectroscopy - EDS, synchrotron x-ray diffraction – XRD), that provides information on the Fe distribution at the nanoscale.

Here, we first discuss our quantitative study of the exchange coupling between the spins S = 5/2 localized on the Fe ions and the effective mass electrons. Our results point to an anomalous *p-d* exchange splitting of the valence band [4], that we explain in terms of a renormalization of extended states occurring if the impurities perturb strongly the crystal potential [6]. We then show that the Fe ions are distributed in the nitride matrix in a way giving rise either to a diluted random alloy [2] – [5] or to ferromagnetic nanocrystals that aggregate by precipitation [2], [3], [5] or by spinodal decomposition into regions more or less rich in the magnetic component [3], [5]. Our latest results demonstrate that this aggregation can be controlled by growth conditions and co-doping with either acceptors or donors.

Strong Coupling Effects in (Ga,Fe)N

In II-VI oxides and III-V nitrides, a small bond length and, thus, strong *p-d* hybridization, should result in a large value of $N_0|\beta|$, and this prediction is supported by photoemission experiments [7]. Surprisingly, however, abnormally small exciton splittings in (Zn,Co)O [8] and (Zn,Mn)O [9] have been observed. Prompted by these observations, a theory has been put forward [6], which shows that the strong *p-d* coupling makes the apparent exchange energy $N_0\beta^{(app)}$ describing the valence band splitting small and of opposite sign than expected. In order to test the above model, magnetization and magnetoreflectivity in the free exciton region of (Ga,Fe)N epilayers have been studied [4], as reported in Fig. 1(a, b). Since in GaN – in contrast to ZnO – the actual ordering of valence subbands is settled, the sign of $N_0\beta^{(app)}$ can be unambiguously determined from polarization-resolved magnetooptical spectra. Furthermore, unlike Mn, Fe in GaN is an isoelectronic impurity with the simple d^5 configuration [2], [10], allowing a straightforward interpretation of the data.

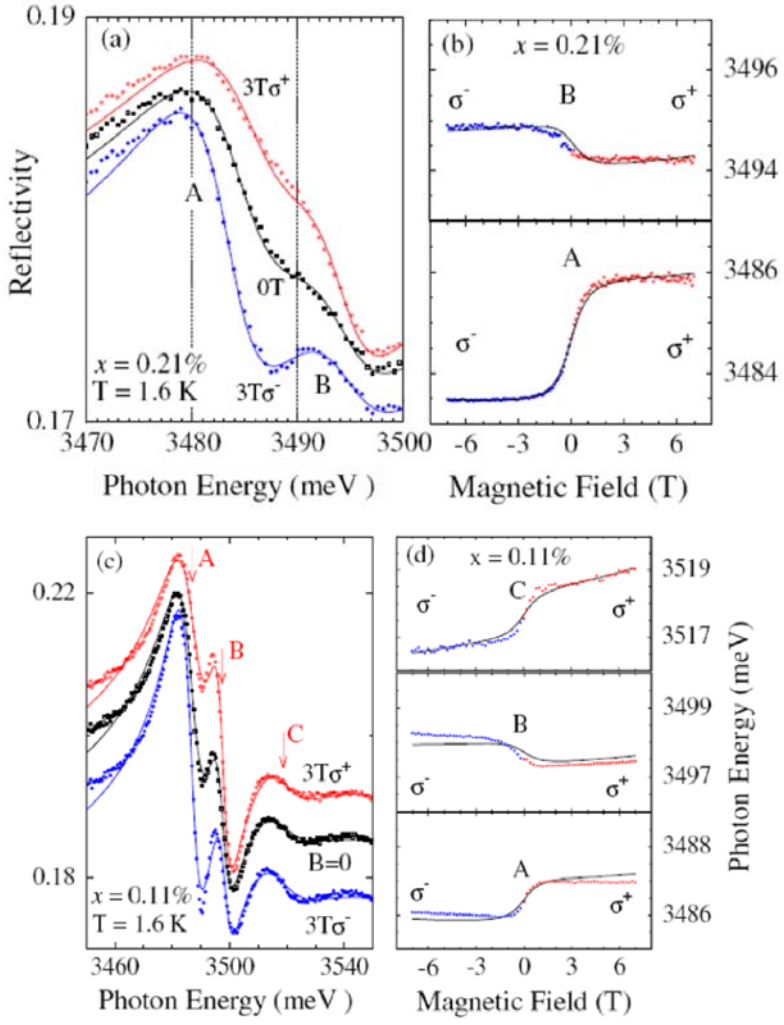

Fig. 1: Reflectivity of (Ga,Fe)N in Faraday configuration at 1.6 K for x = 0.21% (a) and 0.11% (c) where particularly well-resolved excitons A, B, and C are visible in σ^- polarization. Panels (a), (c) show experimental data (symbols) and their fitting with the polariton model (solid lines). Symbols in (b), (d) present exciton energies obtained from such a fitting at various magnetic fields; solid lines are the expectation of the exciton model for the exciton.

The fitting procedure, whose results are presented in Fig. 1 (b), (d) yielded $N_0\beta^{(app)}$ = +0.5 ± 0.2 eV and $N_0\alpha^{(app)}$ = +0.1 ± 0.2 eV. We note that this evaluation of $N_0\alpha^{(app)}$ includes, within the experimental error, the values of $N_0\alpha^{(app)}$ = 0.25 ± 0.06 eV found in early studies of Mn-based II-VI DMSs [11]. We have no reason to question here the applicability of the standard description of the conduction band in (Ga,Fe)N. For the expected *d* level arrangement, both the ferromagnetic sign and the small magnitude of the apparent *p-d* exchange energy are surprising. Indeed, in GaN the Fe d^5/d^6 acceptor-like level resides less than 3 eV above the top of the valence band [10].

This state, $e_g\downarrow$, and the higher lying $t_2\downarrow$ level that can hybridize with the valence band states, remain unoccupied in intrinsic (Ga,Fe)N. At the same time, no donor-like d^5/d^4 state has been found within the GaN gap. This could be expected, as in the transition metal (TM) series a particularly large correlation energy *U* separates the d^5 and d^6 shells. Hence, the occupied Fe $t_2\uparrow$ levels reside within the valence band. According to the Schrieffer-Wolf theory, in such a case the *p-d* exchange coupling is antiferromagnetic: this was confirmed by magnetooptical studies of tellurides and selenides containing either Mn or Fe, including studies carried out in our labs, which lead systematically to $N_0\beta = -1.4 \pm 0.5$ eV [11].

However, it has been recently remarked [6] that for an appropriately strong TM potential like the one expected for oxides and nitrides, the magnetic ion can bind a hole – a trend which was already suggested by strong deviations from the virtual crystal approximation (VCA) in (Cd,Mn)S [12] and by results of the numerical diagonalization of a model Hamiltonian for diluted magnetic semiconductors (DMS) [13]. A summation of infinite series of relevant self-energy diagrams demonstrates that the spin splitting of extended states involved in the optical transitions remains proportional to the magnetization, but the apparent exchange energy becomes significantly renormalized [6]. For the expected coupling strength, the theory predicts $-1 < \beta^{(app)}/\beta < 0$, as observed for (Ga,Fe)N.

Observation and Control of Fe Aggregation in (Ga,Fe)N

There is an increasing amount of evidence that owing to specific features of magnetic impurities in wide band-gap semiconductors and oxides, the epitaxial growth of these systems can result in the self-organized aggregation of magnetically robust nanocrystals embedded in the host paramagnetic matrix [1], [14], [15]. With no doubt this finding holds enormous potential for the fabrication of a range of multifunctional nanosystems relevant to spintronics, nanoelectronics, photonics, and plasmonics [14], [16].

A series of (Ga,Fe)N layers has been grown by MOVPE [5] and by combining TEM and synchrotron XRD with SQUID studies we have identified three distinct ways by which Fe incorporates into the GaN lattice: (i) substitutional Fe^{3+} diluted ions accounting for the paramagnetic response [2]; (ii) Fe-rich (Ga,Fe)N wurtzite nanocrystals commensurate with and stabilized by the GaN host lattice and (iii) hexagonal ε-Fe_3N precipitates, as summarized in Fig. 2. The formation of nanocrystals containing a large density of the magnetic constituent elucidates the origin of the ferromagnetic features persisting up to above room temperature.

Furthermore, we have found [5] that by increasing the growth rate we can reduce the presence of secondary phases and then hamper the spinodal decomposition. This influence of the growth rate on the nanocrystal formation indicates that the Fe aggregation occurs at the growth surface. Importantly, our TEM, synchrotron XRD, and SQUID data reveal that the aggregation of Fe cations can be diminished or even prevented by co-doping with either Si donors or Mg acceptors.

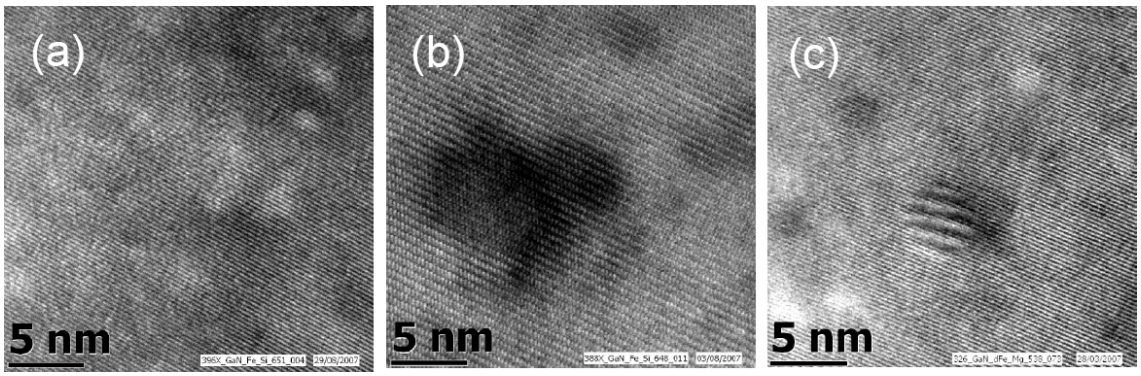

Fig. 2: High-resolution TEM images of (a) diluted GaN:Fe; (b) Fe-rich (Ga,Fe)N wurtzite regions coherent with the GaN matrix; (c) hexagonal ε-Fe_3N nanocrystal.

Since, quite generally, the binding energy of TM pairs depends on the valency of the open *d*-shells [17], there is a ground to suppose that the Fermi level engineering we evoke for (Ga,Fe)N:Si,Mg and others for (Zn,Cr)Te [18] can serve to control the magnetic ion aggregation in a number of semiconductors and oxides, providing a way to the self-organized fabrication of multi-component systems with tailored magnetic, magneto-optical, and magneto-transport properties at the nanoscale.

Acknowledgements

This work has been supported by the Austrian Fonds zur Förderung der wissenschaftlichen Forschung - FWF (projects P17169, P20065 and N107-NAN)

References

[1] A. Bonanni. Semicond. Sci. Technol., 22:R41, 2007.

[2] A. Bonanni, M. Kiecana, C. Simbrunner, T. Li, M. Sawicki, M. Wegscheider, M. Quast, H. Przybylinska, A. Navarro-Quezada, R. Jakiela, A. Wolos, W. Jantsch, and T. Dietl. Phys. Rev. B, 75:125210, 2007.

[3] M. Wegscheider, Tian Li, A. Navarro-Quezada, B. Faina, A. Bonanni, W. Pacuski, R. Jakie la, and T. Dietl. J. Phys: Condens. Matter, 20:454222, 2008.

[4] W. Pacuski, P. Kossacki, D. Ferrand, A. Golnik, J. Cibert, M. Wegscheider, A. Navarro-Quezada, A. Bonanni, M. Kiecana, M. Sawicki, and T. Dietl. Phys. Rev. Lett., 100:037204, 2008.

[5] A. Bonanni, A. Navarro-Quezada, T. Li, M. Wegscheider, Z. Matej, V. Holy, R.T. Lechner, G. Bauer, M. Kiecana, M. Sawicki, and T. Dietl. Phys. Rev. Lett., 101:135502, 2008.

[6] T. Dietl. Phys. Rev. B, 77:085208, 2008.

[7] T. Mizokawa, T. Nambu, A. Fujimori, T. Fukumura, and M. Kawasaki. Phys. Rev. B, 65:085209, 2005.

[8] W. Pacuski, D. Ferrand, J. Cibert, C. Deparis, J. A. Gaj, P. Kossacki, and C. Morhain. Phys. Rev. B, 73:035214, 2006.

[9] E. Przezdziecka, E. Kaminska, M. Kiecana, M. Sawicki, L. K lopotowski,W. Pacuski, and J. Kossut. Solid State Commun., 139:541, 2006.

[10] E. Malguth, A. Hoffmann, and M. R. Phillips. phys. stat. sol. (b), 245:455, 2008.

[11] P. Kacman. Semicond. Sci. Technol., 16:R25, 2001.

[12] C. Benoit à la Guillaume, D. Scalbert, and T. Dietl. Phys. Rev. B, 46:9853(R), 1992.

[13] R. Bouzerar, G. Bouzerar, and T. Zimai. Europhys. Lett., 78:67003, 2007.

[14] H. Katayama-Yoshida, K. Sato, T. Fukushima, M. Toyoda, H. Kizaki, V. A.Dinh, and P. H. Dederichs. phys.stat. sol. (a), 204:15, 2007.

[15] M. Jamet, A. Barski, T. Devillers, V. Poydenot1, R. Dujardin, P. Bayle-Guillmaud, J. Rotheman, E. Bellet-Amalric, A. Marty, J. Cibert, R. Mattana, and S. Tatarenko. Nature Mat., 5:653,2006.

[16] T. Dietl. J. Appl. Phys., 103:07D111, 2008.

[17] T. Dietl. Nature Mat., 5:673, 2006.

[18] S. Kuroda, N. Nishizawa, K. Takita, M. Mitome, Y. Bando, K. Osuch, and T. Dietl. Nature Mat., 6:440, 2007.

Photonics and Optoelectronics (Posters)

Performance of Phonon Depopulated Terahertz Quantum Cascade Lasers

Ch. Deutsch[1], A. Benz[1], G. Fasching[1], K. Unterrainer[1], A. M. Andrews[2], P. Klang[2], W. Schrenk[2], and G. Strasser[2]

[1] Photonics Institute and Center for Micro- and Nanostructures, Vienna University of Technology, Gusshausstrasse 29/387, 1040 Vienna, Austria

[2] Institute of Solid-State Electronics and Center for Micro- and Nanostructures, Vienna University of Technology, Floragasse 7/362, 1040 Vienna, Austria

In this contribution we present experimental results of optimized active regions for terahertz quantum cascade lasers. The optimization was achieved by employing a Non-equilibrium Green's Functions model. Theoretical results suggested to revise the extraction barrier of the current design in order to increase the peak gain. Measurements showed an improved dynamic range and also an increased operating temperature of 145 K.

Introduction

The mid-infrared (MIR) quantum cascade laser was demonstrated in 1994 [1] and 8 years later the concept was successfully extended to the terahertz region [2]. So, the terahertz quantum cascade laser (THz QCL) might be the long wavelength relative but not for operating temperatures, which in contrast to room temperature-working MIR QCLs still requires cryogenic cooling [3].

Terahertz radiation has lots of potential applications (spectroscopy, imaging, medical diagnostics, etc.), which means solid-state, compact and efficient sources would be very desirable. At the moment only quantum cascade lasers fulfill these criteria and a lot of effort is put into pushing the operating temperatures at least to 240 K. Such temperatures are accessible with thermoelectric cooling stages.

Theory

Unlike in ordinary semiconductor band gap lasers, the energy levels in a quantum cascade laser are formed only in the conduction band of a semiconductor heterostructure. Consequently, one is no longer limited by the naturally given band gap of a material, in fact one can now tailor the optical transition energy by changing the width of the wells and barriers. The difficulty in realizing a terahertz quantum cascade laser is the small energy spacing of the lasing transition (1 THz is equivalent to 4 meV) and to establish population inversion in the presence of phonons. One successful realization is the so-called phonon depopulation scheme [4]. It is a combination of resonant tunneling and sub-picosecond emission of a longitudinal optical phonon for an efficient depopulation of the lower laser state. In a previous study we showed that the threshold current density can be significantly reduced with a lower doping density [5]. Unfortunately not only the threshold is reduced but also the dynamic range. The limiting factor is the onset of a negative differential resistance region. One design strategy for reaching higher operating temperatures is to extend the dynamic region. In a collaboration a newly devel-

oped transport code based on Non-equilibrium Green's Functions (NEGF) [6] was used to improve the design of the active region. This realistic description of the transport in such a heterostructure can be used to obtain an energy-resolved density distribution and to calculate the peak gain of the active region (Fig. 1). Simulations focused on the barrier responsible for the resonant tunneling out of lower laser state suggested to reduce the anticrossing of the involved states. This is done by thickening the barrier from 4.1 to 5.2 nm.

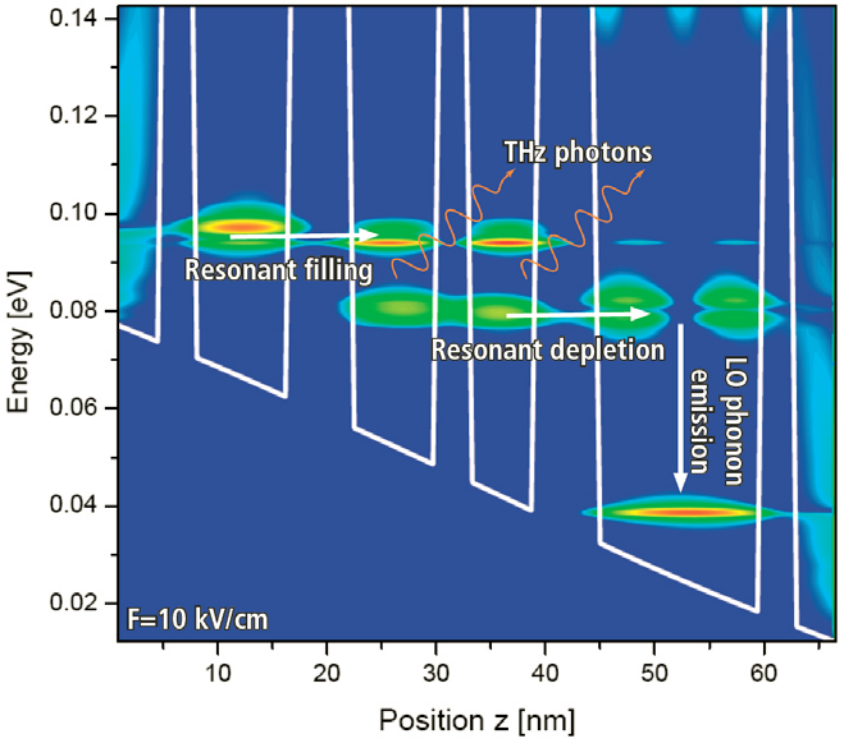

Fig. 1: Simulation results gained from the NEGF based transport model. The energy-resolved local density of states is color coded. The white lines represent the conduction band profile [6].

Experimental

Sample Preparation

The active region designs were realized in the GaAs/$Al_{0.15}Ga_{0.85}As$ material system by molecular beam epitaxy (MBE). The 15 µm thick heterostructure is then processed into a so-called double-metal waveguide, very similar to a microstrip transmission line.

First of all, a piece of the device wafer and the receptor wafer (n+ doped) are prepared with a thick gold layer (~ 1 µm) for thermocompression bonding. The bonding takes place at 330 °C and under constant pressure of 200 bar. Afterwards the device substrate is removed by polishing, followed by selective wet etching stopping at the underlying etch stop layer of the heterostructure. Another selective wet etching step removes this etch stop layer. Now, since the active region is accessible again, standard processing methods can be applied. Ridge resonators are lithographically defined, a gold top contact is sputtered and the mesas are formed by reactive ion etching in a $SiCl_4/N_2$ plasma environment.

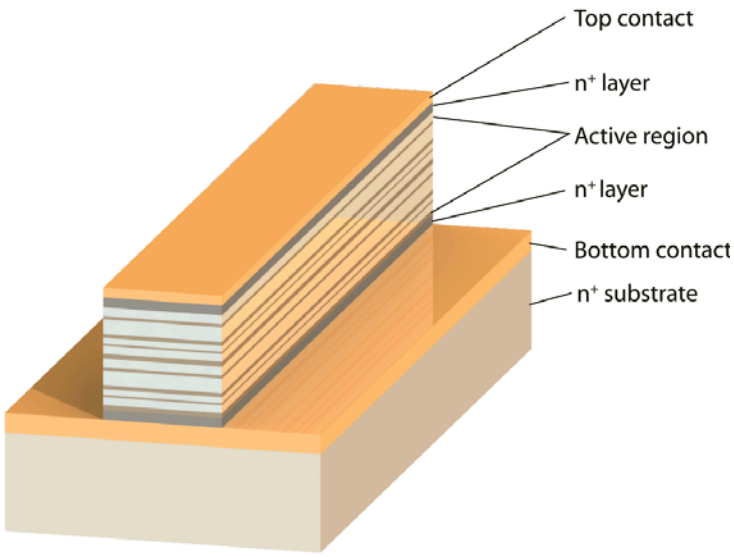

Fig. 2: Schematic of the processed double-metal ridge laser. The active region is sandwiched between two layers of gold which function as waveguides and electrical contacts.

Measurements

The samples are mounted on the cold finger of a cryostat and the terahertz radiation is collected by an off-axis parabolic mirror. The collinear beam is guided through a Fourier transform spectrometer and detected with a liquid helium cooled silicon bolometer. In pulsed operation a lock-in detection technique is applied to increase the signal-to-noise ratio.

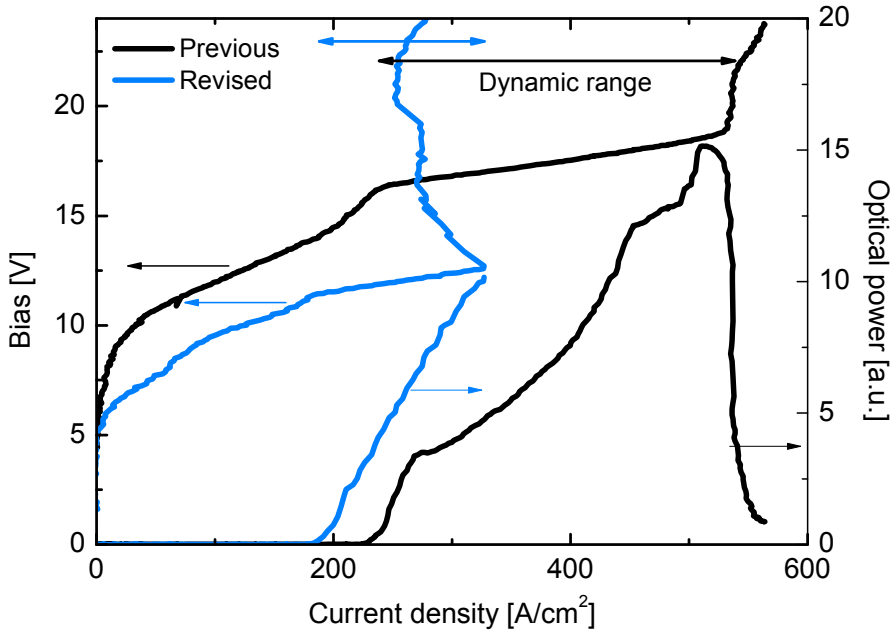

Fig. 3: LIV characteristics - comparison of the previous and the revised structure. The double arrows on top clearly show the improved dynamic range.

Figure 3 shows the electrical characteristics and optical power of the previous and the revised design. The previous design features a pronounced negative differential resistance (NDR) region which limits the operation at higher current densities. After redesigning the extraction barrier, the current transport is no longer limited by an NDR region and the dynamic range is almost extended by a factor of 2.5. However, the influence on the maximum operating temperature was not that dramatic, raising it from 140 K to 145 K.

Conclusion

We were able to improve the active region design of a terahertz quantum cascade lasers by using a sophisticated transport theory based on Non-equilibrium Green's Functions. The revised design exhibits an extended (more than doubled) dynamic range and therefore reaches slightly higher operating temperatures.

Acknowledgements

We gratefully acknowledge the financial support from the Austrian Scientific Fund FWF (Spezialforschungsbereich ADLIS and IRON, DK CoQuS) and the Austrian nano initiative project PLATON.

References

[1] J. Faist, F. Capasso, D. L. Sivco, C. Sirtori, A. L. Hutchinson, and A. Y. Cho: "Quantum cascade laser", Science 264, 553 (1994).

[2] R. Köhler, A. Tredicucci, F. Beltram, H. E. Beere, E. H. Linfield, A. G. Davies, D. A. Ritchie, R. C. Iotti, and F. Rossi: "Terahertz semiconductor-heterostructure laser", Nature 417, 156 (2002).

[3] S. Kumar, Q. Hu, ad J. L. Reno: "186 K operation of terahertz quantum-cascade lasers based on a diagonal design", Appl. Phys. Lett. 94, 131105 (2009).

[4] B. S. Williams, H. Callebaut, S. Kumar, Q. Hu, and J. L. Reno: "3.4 THz quantum cascade laser based on longitudinal-optical-phonon scattering for depopulation", Appl. Phys. Lett. 82, 1015 (2003).

[5] A. Benz, G. Fasching, A. M. Andrews, M. Martl, K. Unterrainer, T. Roch, W. Schrenk, S. Golka, and G. Strasser: "Influence of doping on the performance of terahertz quantum cascade lasers", Appl. Phys. Lett., 90, 101107 (2007).

[6] T. Kubis, C. Yeh, P. Vogl, A. Benz, G. Fasching, and C. Deutsch: "Theory of nonequilibrium quantum transport and energy dissipation in terahertz quantum cascade lasers", Phys. Rev. B 79, 195323 (2009).

Photonic Crystal Frequency Control in Terahertz Lasers

A. Benz[1], Ch. Deutsch[1], G. Fasching[1], K. Unterrainer[1], A. M. Andrews[2], P. Klang[2], W. Schrenk[2], and G. Strasser[2]

[1] Photonics Institute and Center for Micro- and Nanostructures, Vienna University of Technology, Gusshausstrasse 29/387, 1040 Vienna, Austria

[2] Institute of Solid-State Electronics and Center for Micro- and Nanostructures, Vienna University of Technology, Floragasse 7/362, 1040 Vienna, Austria

We present the design and the fabrication of a photonic crystal with a complete bandgap for TM-modes. The photonic crystal is used as a resonator for terahertz quantum-cascade lasers. This allows us to control the emission frequency of the devices within the gain region precisely.

Introduction

Designing microresonators for semiconductor lasers is a challenging task. Aspects such as cavity quality factor, laser far-field, lasing threshold or output power have to be balanced. All of them are greatly influenced by the resonator. The widely used standard resonator geometries, such as Fabry-Perot or ring resonators, do not allow meeting all the requirements simultaneously. The full control over the dispersion relation is required.

Photonic crystals (PhCs) offer exactly this unique feature, the control of optical properties on a sub-wavelength scale [1]. All device characteristics such as quality factor [2] or lasing far-field [3] can be designed. For the realization of compact lasers, direct integration of an active gain medium into the PhC is the most promising solution. However, for conventional semiconductor lasers, this approach is limited by the greatly increased device surface which leads to strong increase in surface recombination and leakage currents. Any benefit gained by the improved resonator is destroyed by the increased threshold current. Therefore, it is necessary to separate both components spatially, leading to increased device size and complexity. Quantum-cascade lasers (QCLs), being unipolar devices, do not suffer from any of these parasitic effects, which make them the ideal choice for monolithic solutions. Since their realization in 1994 [4], QCLs have become the preferred source in the mid-infrared and terahertz (THz) spectral region, covering wavelengths from 3 to 300 µm.

Design of Photonic Crystals

The present work describes the design and fabrication of PhC-resonators for THz-QCLs. The PhC used consists of free standing pillars which are surrounded by air. A calculated band structure for the ideal PhC is presented in Fig. 1. This two-dimensional array is embedded in a double-metal waveguide for vertical confinement. The pillars have diameters between 12 and 21 µm which make them significantly smaller than the emission wavelength of typically 120 µm. The period of the PhC is in the range of 22 to 35 µm, resulting in a filling factor of only 33%. The sub-wavelength pillars are fabri-

cated directly from the active THz quantum cascade layer structure. Thereby, we are able to realize all components monolithically.

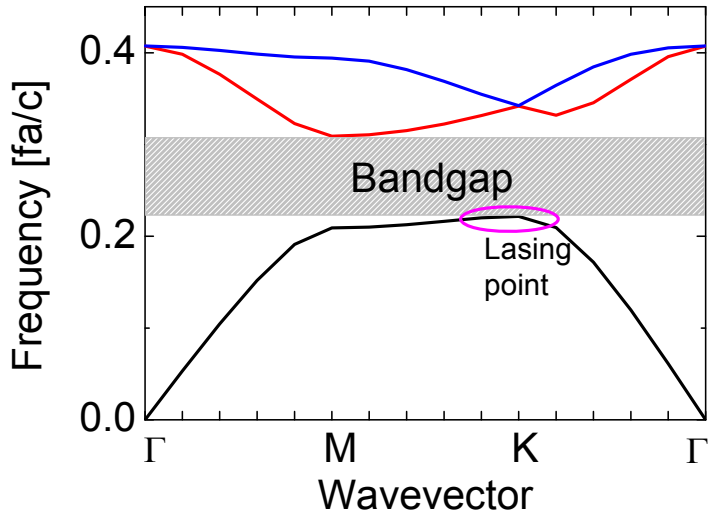

Fig. 1: A calculated band structure for the perfect, two-dimensional PhC. The first full bandgap for TM-modes is clearly visible.

Experimental Results

We start with devices based on a bulk gain region which is surrounded by a PhC-mirror. Both components are embedded in a double-metal waveguide which ensures strong interaction of the optical mode with the PhC and prevents any out-of-plane scattering. This approach achieves a reasonable frequency control while maintaining a simple processing based on standard planar processing technology. Spectra for PhCs with periods ranging from 22.18 to 35.49 µm are presented in Fig. 2.

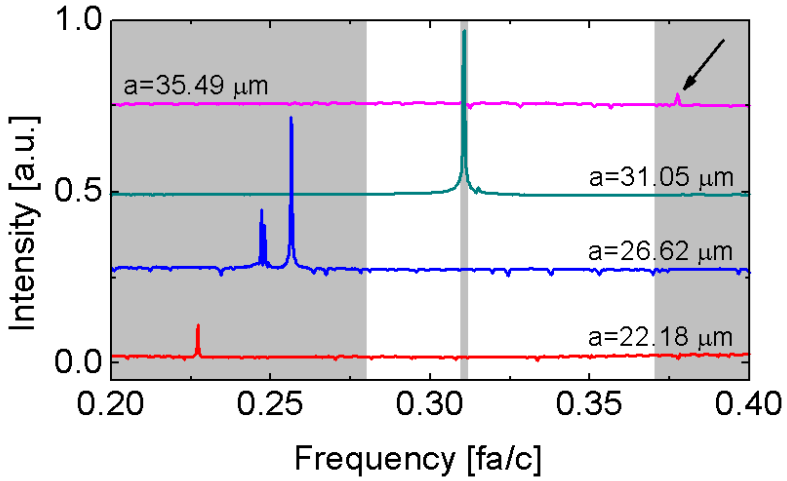

Fig. 2: Measured spectra for the PhC-resonator with different PhC-periods. The emission can be tuned from the gain maximum of the active region into the bandgap of the PhC-mirror.

The second type of devices omits the bulk gain region [5], [6]. Instead the pillars themselves provide the necessary optical gain as they are fabricated directly from the active region THz quantum-cascade layer structure; a SEM-image of the finished device is shown in the inset of Fig. 3. This resonator type requires a substantially more complicated processing. However, it offers some advantages compared to the first approach, such as small cavity volumes, stable single-mode emission or large tuning range. We are able to achieve resonators with diameters of 240 µm, comparable to twice the emission wavelength. It is important to stress that only 1/3 of the volume contains gain region. Nevertheless, the strong index contrast between the active region and the surrounding vacuum allow us to achieve a modal confinement of 95 %. The strong optical coupling of the lasing mode and the PhC results in stable-single mode emission for all driving currents, results for a PhC with a 26.62 µm period are shown in Fig. 3. Varying the PhC period allows us to tune the emission frequency over 400 GHz, this is significantly larger than the typical gain bandwidth of THz-QCLs of only 130 GHz [7].

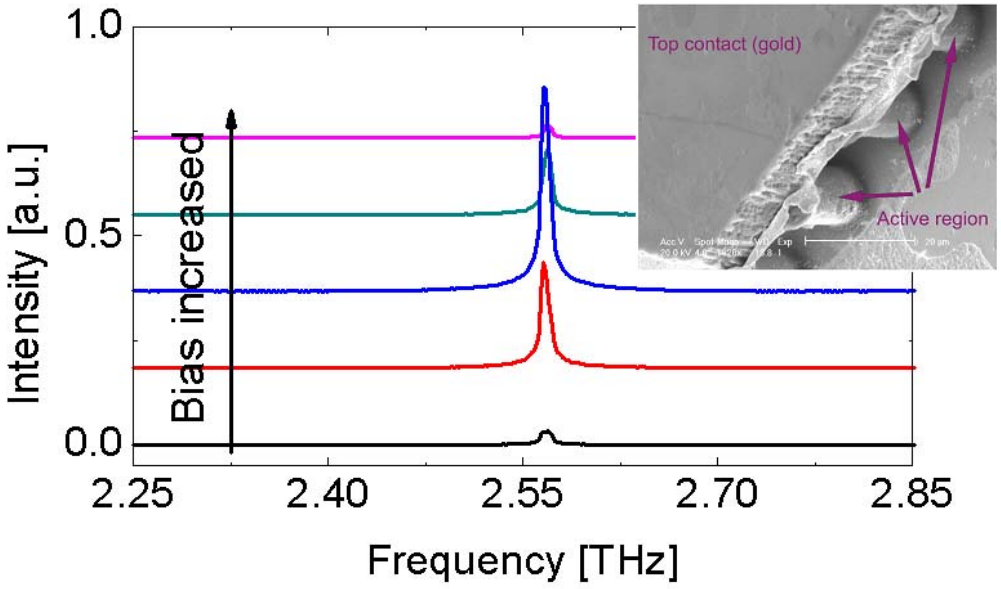

Fig. 3: Measured spectra for the active PhC-resonator with a period of 26.62 µm. The stable single-mode emission under all driving conditions is clearly visible. The inset is showing a SEM-picture of the facet.

Conclusion

We have presented different resonator concepts for THz-QCLs based on PhC. The designable dispersion of the PhCs allows us to tune the optical properties of the resonators on a sub-wavelength scale. The emission wavelength can be adjusted to almost any value within the gain bandwidth.

Acknowledgements

This work was partly supported by the Austrian Scientific Fund FWF (SFB ADLIS, SFB IR-ON, DK CoQuS) and the Austrian nano initiative project (PLATON).

References

[1] J. D. Joannopoulos, S. G. Johnson, J. N. Winn and R. D. Meade, “Photonic crystals – Molding the flow of light”, Princeton University Press, 2008

[2] Y. Tanaka et al., Nature Materials 6, 862 (2007)

[3] Y. Chassagneux et al., Nature (London) 457, 174 (2009)

[4] J. Faist et al., Science 264, 553 (1994)

[5] H. Zhang et al., Opt. Express 15, 16818 (2007)

[6] A. Benz et al., Opt. Express 17, 941 (2009)

[7] J. Kröll et al., Nature (London) 449, 698 (2007)

Fabrication of Ordered Ge Quantum Dots Arrays on Prepatterned SOI Platform for Waveguide Photodetectors and Emitters

G. Chen, V. Lavchiev, F. Schäffler, G. Bauer, and W. Jantsch

Institut für Halbleiter- und Festkörperphysik, Johannes-Kepler-Universität Linz, A-4040 Linz

Introduction

Silicon-on-insulator substrates offer opportunities for integrated optics and micro photonic applications. A thick buried oxide covered by a crystalline silicon layer leads to a very high difference of refractive index, which is as large as two in the near-infrared spectral range. With such a large variation, strong optical confinement can be easily achieved in the transparency window of silicon, and in particular, in the spectral windows around 1.3 and 1.55 μm corresponding to the telecommunication wavelengths. Meanwhile Ge/Si self-assembled islands with their high-Ge content are good candidates to operate at telecommunication wavelengths. They can be epitaxially covered by silicon and offer the advantage of silicon-terminated surfaces, thus keeping the compatibility with silicon standard processing. Moreover, our recent work shows that the ordered Ge quantum island arrays could be obtained by growth on a prepatterned Si substrate. The ordered Ge quantum island arrays could provide high homogeneity in both size and height of the Ge islands, which might lead to a narrowing of the photo emission.

In this work, we report on the fabrication of a set of ordered Ge self-assembled quantum dots arrays on prepatterned SOI platforms. Structural and optical as well as electronic analyses of the arrays are presented.

Experiment and Results

Silicon-on-insulator substrates offer opportunities for integrated optics and micro photonic applications. To explore their advantages, in this work, we fabricated of a set of ordered Ge self-assembled quantum dots arrays on prepatterned SOI platforms, as shown in Fig. 1 and Fig. 2. This design exhibits the compatibility with current Si-based VLSI technology. The rib waveguide and RCE detectors can also improve the quantum efficiency by increasing equivalent absorption length. Furthermore, the incorporation of the multilayer of ordered Ge-QDs can improve the moderate oscillator strength of optical transition when precisely located at places with high photonic density of states [1].

To achieve this aim, the main challenge we were facing is to fabricate ordered Ge-QDs on the rib waveguide. We have successfully achieved the Ge-QDs arrays on the patterned flat Si (001) substrate [2], [3]. Based on these results, we tried two different approaches.

The first try is to deposit 7ML Ge under 620 °C, at a fixed growth rate of 0.03 A/s on the rib waveguide, which has been pit-patterned by electron beam lithography and reactive etching. Atomic Force Microscopy shows most of the Ge islands nucleate at the edge of the waveguide instead of the pit site prepared by patterning, as shown in Fig. 3.

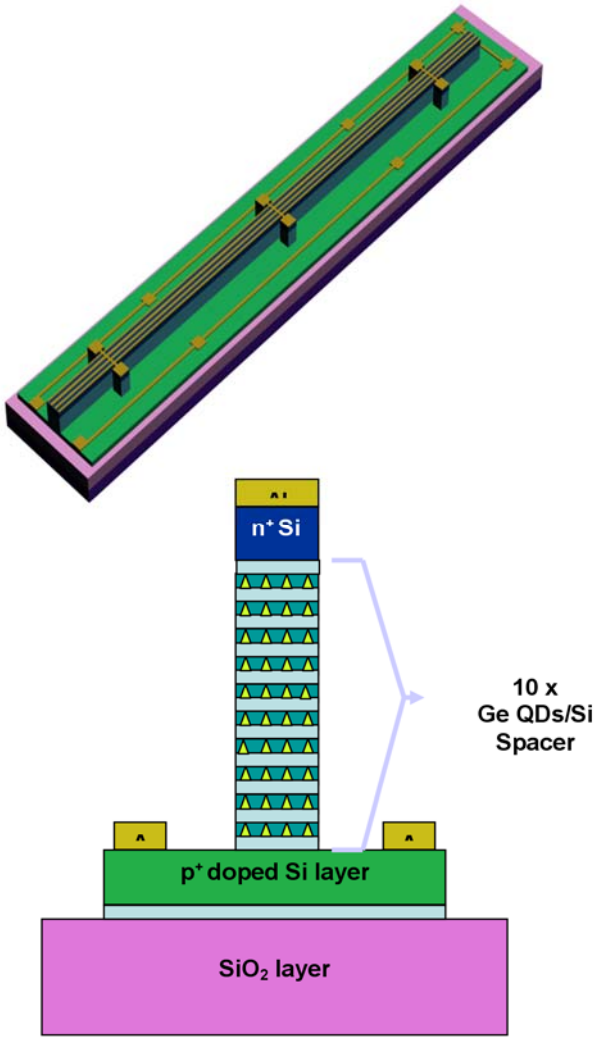

Fig. 1: Scheme of rib-waveguide integrated p-i-n Ordered Ge-QDs Photodetector

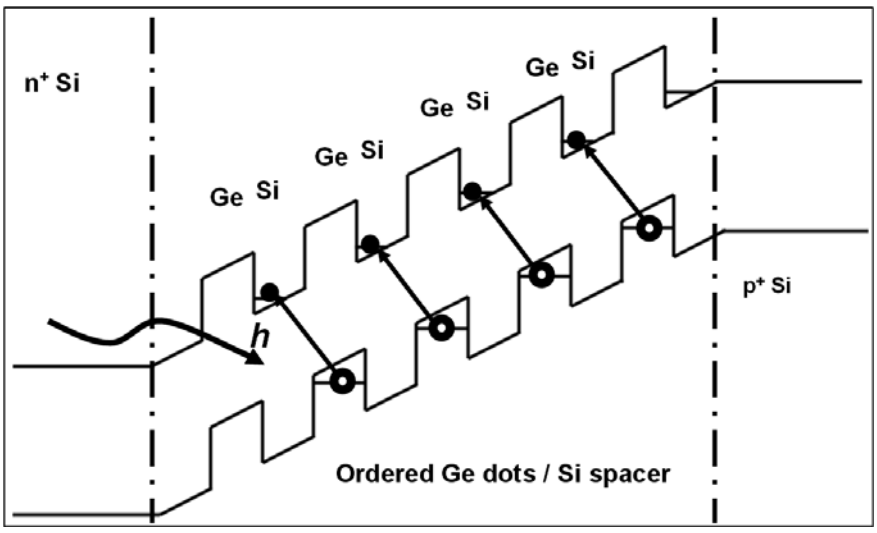

Fig. 2: Simplified bandgap diagram for rib-waveguide integrated p-i-n ordered Ge-QDs photodetector under bias.

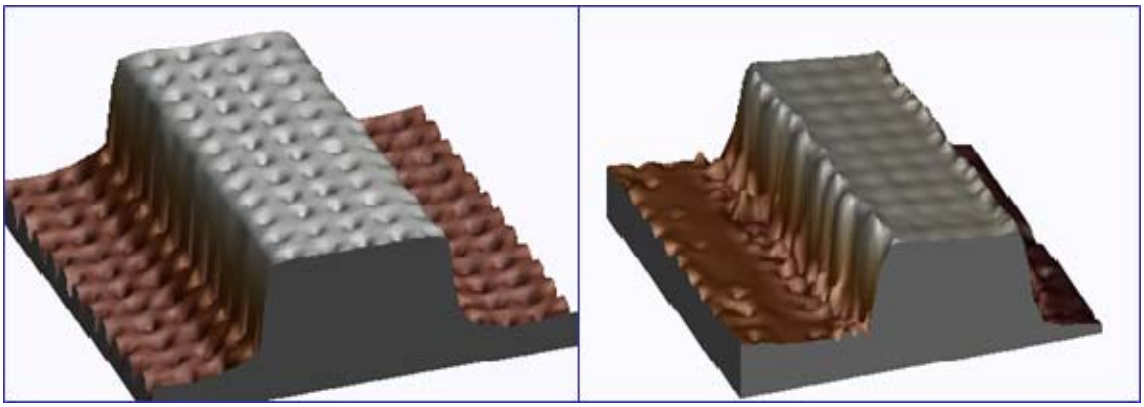

Fig. 3: AFM image of the patterned waveguide before and after Ge deposition.

This phenomenon could be explained by the fact that the edge is the energetically most favorite site.

Another try was performed by changing the sequence of the above experiment, i.e., first an array of ordered Ge islands was prepared on the flat Si substrate, and then a waveguide was prepared through electron beam lithography and reactive ion etching. This approach is quite successful, as shown in Fig. 4.

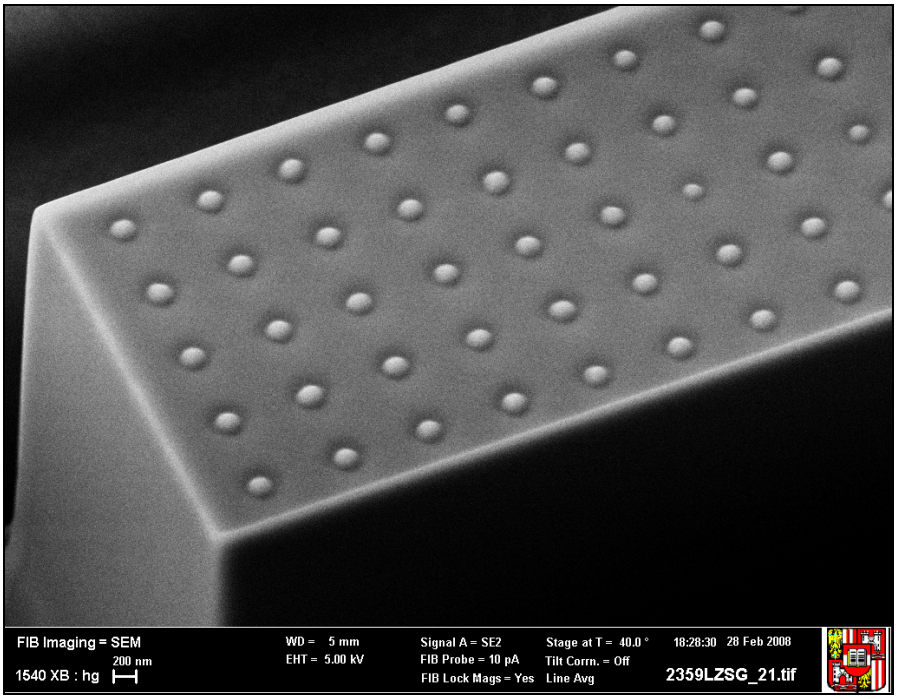

Fig. 4: SEM image showing the ordered Ge array sits on the rib-waveguide.

The temperature dependence of photoluminescence of the patterned Ge dots array has been measured. A UV cw-Ar+ laser was used for the excitation. A LN-cooled Ge detector with lock-in amplifier was used for detection. We observed a red-shift of the Ge dots peak with increase of temperature.

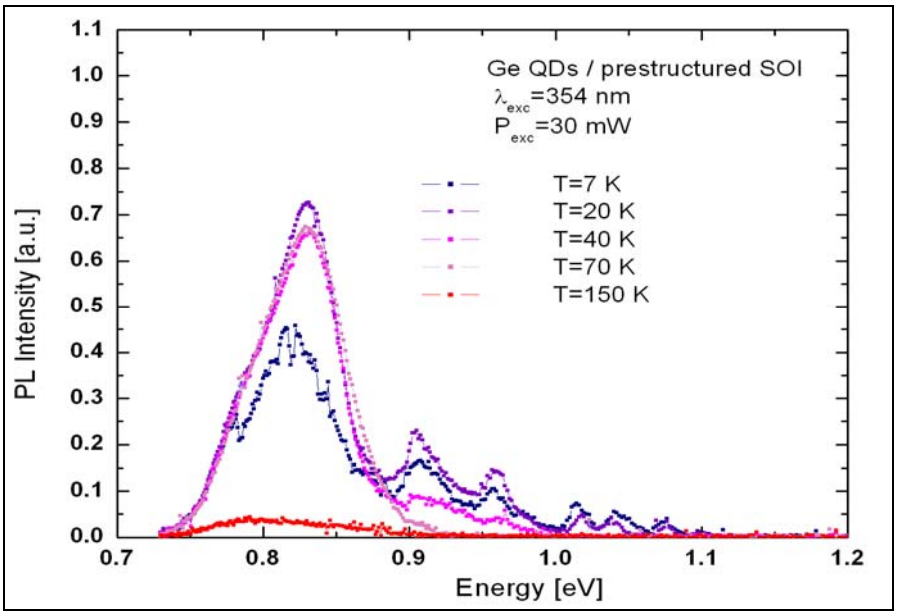

Fig. 5: Temperature dependence of the photoluminescence of the patterned Ge dots array.

References

[1] C. B. Li, et. al., Appl. Phys. Lett. 85 2697 (2004).

[2] G. Chen, et. al., Phys. Rev. B 74 035302 (2006).

[3] G. Chen, et. al., Appl. Phys. Lett. 92 113106 (2008).

Highly Efficient (Infra)-Red-Conversion of InGaN Light Emitting Diodes by Nanocrystals, Enhanced by Color Selective Mirrors

R. Seyrkammer, J. Roither, M. V. Kovalenko, and W. Heiss

Institute of Semiconductor and Solid State Physics, University of Linz, Altenbergerstr. 69, 4040 Linz, Austria

Colloidal nanocrystal layers deposited onto the enclosure of InGaN light emitting diodes are demonstrated to operate as nano-phosphors for color conversion with high color stability. Dependent on the choice of the nanocrystal materials, either CdSe/ZnS or PbS nanocrystals are applied, the diode emission at 470 nm is converted to the red or to infrared light, with similar quantum efficiencies. The color conversion is further improved by dielectric mirrors with high reflectivity at the emission band of the nanocrystals, resulting in an almost doubling of the nanocrystal light extraction from the devices, which increases the nanocrystal device efficiency up to 19.1%.

Introduction

The development of energy and cost efficient, reliable and long-lived solid state light emitting devices with excellent color stability and color rendering capability is one of the main challenges in lighting industry [1] – [3]. As a result of the continuing progress in the development of solid state light sources for more and more applications incandescent or fluorescent light sources are replaced by light emitting diodes [1], [2] (LEDs) based on III-V nitride compound semiconductors. These LEDs emit in the blue or in the blue-green [4] and color conversion with phosphors is commercially adopted to generate “white” light from a single-chip LED by combining the converted light, i.e. the phosphor emission with the remaining blue LED emission [1]. Promising candidates to be used as nano-phosphors are in particular CdSe/ZnS core/shell nanocrystals (NCs) due to their excellent environmental stability combined with their exceedingly high fluorescence quantum yield [5]. While in the previous reports the excellent color quality of nanocrystal based color conversion has been highlighted [6], here we rather focus on the efficiency of the color conversion, which we almost double by depositing color selective Bragg mirrors directly onto the LED devices. By controlling the film thickness of the nanocrystals on the InGaN LEDs, light emission ranging from blue to pure red is demonstrated with excellent brightness dependent color stability. Furthermore, color conversion from the blue to the near-infrared spectral region is demonstrated by using PbS NCs, resulting in as high quantum efficiencies as in the visible.

Sample Preparation

For the color conversion experiments we make use of commercial InGaN-LEDs (Nichia corporation, type NSPBF50S) exhibiting strong blue electroluminescence around a wavelength of 470 nm, and having a molded and transparent epoxy enclosure with a flat-top surface. Onto the flat surface uniform films of colloidal CdSe/ZnS core/shell

NCs in a polymethyl methacrylate (PMMA) matrix are deposited by drop- or spin-casting, depending on the required NC-quantity (sample series S1). The NC volume fraction amounts 2.53% corresponding to a NC density n_{NCs}=4.37x10^{17} cm^{-3}. The total number of deposited NCs is varied between 6.54x10^{11} and 1.97x10^{14}. Prior to the mixing into the PMMA, dodecylamine (DDA) is added to the NCs delivered from NFM Ltd (m_{NCs}:m_{DDA} = 2:1) to improve their surface passivation and their dispersion in chlorobenzene (CB). An image of a diode with a NC film deposited on its oval shaped surface (length 4 mm and width 1.8 mm) is shown in the inset in Fig 1 (b). We have made use of two series of samples, for the series S1 the NCs are directly deposited on the enclosure of the LEDs, while for the series S2 a Bragg interference mirror was placed underneath the NC layer, to recycle photons emitted back into the device.

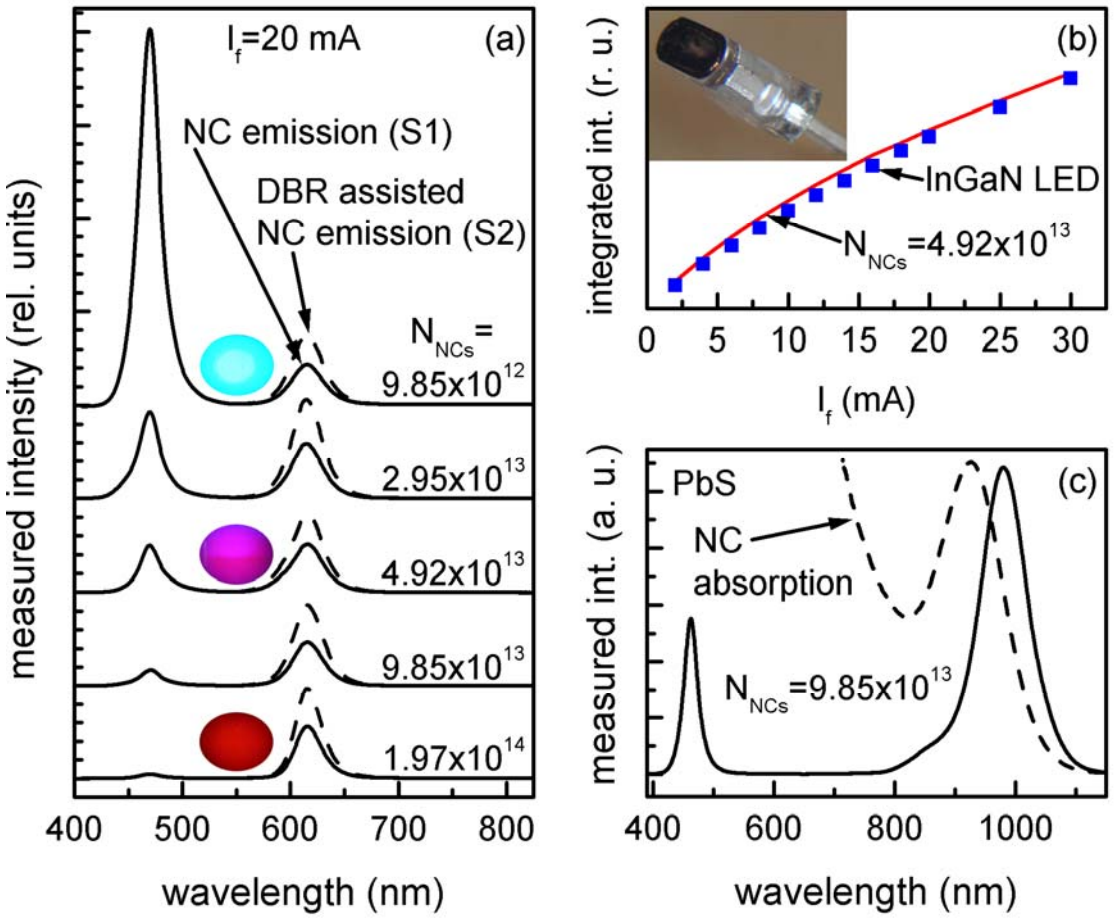

Fig. 1: (a) Emission spectra from sample series S1 (solid lines) and S2 (dashed lines) for different deposited nanocrystal quantities (N_{NCs}). For 9.85x10^{12}, 4.92x10^{13} and 1.97x10^{14} nanocrystals, respectively, the color of the emission is given by the photographs taken from the top of the devices. (b) Spectrally integrated InGaN (squares) and nanocrystal emission (solid line) as function of the LED forward current. The inset shows a photograph of the device with a PbS-PMMA film deposited on top. (c) Absorption spectrum (dashed line) of PbS nanocrystals in solution, used as active material for near-IR color conversion. Emission spectrum (solid line) of a PbS-LED device covered by 9.85x10^{13} nanocrystals.

Conversion Results

For the optical characterization all side faces of the LED enclosure are carefully covered by a black tape to detect emission from the NC covered areas only. The spectra were measured by collecting a part of the hemispherical emission of the devices. To determine the conversion efficiencies, a calibrated photodiode with a flat spectral response was used. The color conversion is demonstrated in Fig. 1 (a), showing the emission spectra of the devices from series S1 biased by a forward current of 20 mA. For clarity, the spectra of samples covered by different NC quantities are shifted in vertical direction with respect to each other. The spectra show clearly two emission maxima, one around 470 nm corresponding to the emission generated in the InGaN diode and the second one around 615 nm originating from the NC film deposited on top of the diode enclosure. With increasing quantity of deposited NCs the intensity of the direct emission from the LED decreases whereas the emission from the NCs slightly increases. By controlling the intensity ratio between the LED and the NC emission the color of the device is tuned between light blue, observed for a NC amount of 9.85×10^{12}, to magenta for 4.92×10^{13} NCs, to almost pure red for 1.97×10^{14} NCs, as is demonstrated by the colored photographs of the device emission shown in Fig. 1 (a). For the sample covered by 4.92×10^{13} NCs the integrated intensity of the blue and the red emission maximum is almost the same, independent of the diode bias, as shown in Fig. 1 (b). The constant ratio between the NC emission (solid line) and the InGaN emission (symbols) across the whole operation range of the diode approves the excellent color stability achieved with the colloidal NCs as nano-phosphor. It should be mentioned that operation over several days did not lead to any change of the red-blue ratio at all.

To show that efficient color conversion can also be achieved for the infrared spectral region we have prepared also devices with PbS NCs, exhibiting their first excitonic absorption peak around 925 nm [dashed line in Fig 1 (c)]. In this case the NCs were dissolved in a PMMA-CB solution, resulting in a NC volume fraction of 6.6% in the film. The emission spectrum of a sample with 9.85×10^{13} NCs deposited on the enclosure of the LED exhibits a strong peak close to a wavelength of 980 nm [solid line in Fig. 1 (c)] in addition to the InGaN peak. By choosing PbS NCs with larger sizes the emission can be shifted to even longer wavelengths up to 1.8 µm (ref. [7]) thus the whole telecommunication wavelength region can be covered by light conversion from InGaN LEDs.

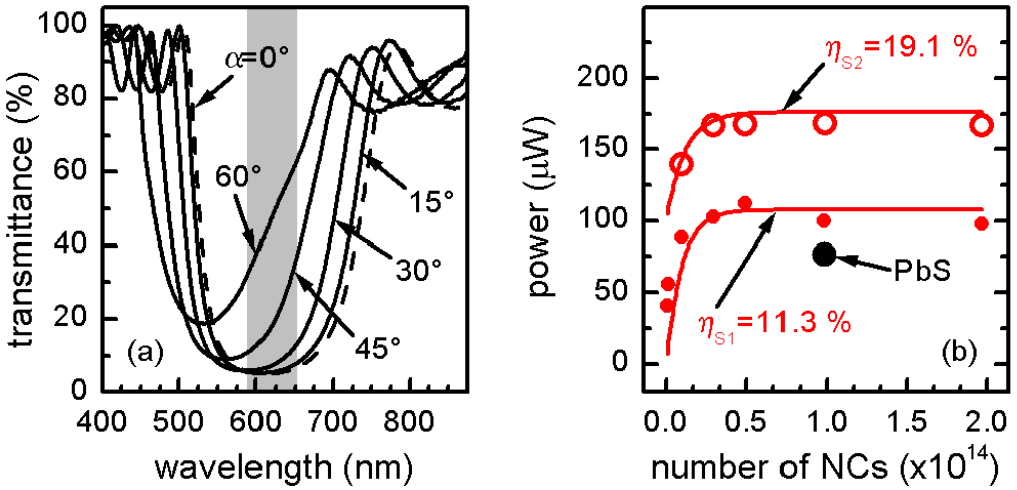

Fig. 2: (a) Transmittance spectra of the used distributed Bragg reflector for several angles of incidence. (b) Power of the color converted light from the nanocrystal quantity for sample series S1 and S2 in dependence on the nanocrystal quantity as well as for the color conversion by PbS nanocrystals.

For the series S2 we designed dielectric mirrors, which are highly reflective at the wavelength of the NC emission but transparent for the blue light from the LED. These mirrors are directly deposited onto the flat surfaces of the LED housing prior to the deposition of the NC films on top of these structures. The distributed Bragg reflectors (DBRs) consist of five pairs of TiO_2 and SiO_2 layers. For normal incidence the mirror stop-band is observed between 550 nm and 700 nm [dashed line in Fig. 2 (a)] and the stop-band center is located at a wavelength of 615 nm, matching perfectly the NC emission band, indicated as grey bar in Fig 2 (a). Outside the stop-band Fabry-Perot interference fringes appear due to multiple reflections at the mirror/air and the mirror/substrate interfaces. At 470 nm, at the emission wavelength of the InGaN LED, the transmittance is T_{470nm} = 90%. The application of such color selective mirrors markedly improves the overall performance of the devices for color conversion, by redirecting the backward directed part of the emission from the NC layer placed on top of the LED housing into the half-space in front of the device. This redirection of the color converted photons is in particular improving their extraction efficiency. The effect is already seen in the emission spectra in Fig. 1 (a) where the dashed lines, representing the measurements performed with devices coated by the color selective DBR mirrors (series S2), exhibit clearly higher intensities within the NC emission band than the uncoated devices. Due to the reflection of the mirror at 470 nm, 10% less of the LED light is absorbed by the NCs as without mirror, but almost twice as much of the NC emission is extracted from the device due to the high reflectivity band of the mirror. This is shown in detail in Fig. 2 (b) where the output power of the devices is shown as function of the amount of deposited nanocrystals. For sample series S1 the device extraction efficiency is 11.3 % whereas the application of the Bragg mirror almost doubles this efficiency to 19.1%. It is also worth to note that in the infrared, by the use of PbS nanocrystals almost the same extraction efficiency is obtained as in the visible, as shown in Fig 2 (b).

Conclusion

As an alternative to rare earth based phosphors colloidal CdSe/ZnS nanocrystals are demonstrated for light conversion from emission of InGaN LEDs to the red. For this purpose, nanocrystal films are deposited onto the enclosures of LEDs, which allows the tuning of the color of the device overall emission between blue and red, with excellent brightness dependent color stability. Color selective mirrors are applied to improve the extraction of the converted light, resulting in an almost doubling of the NC device efficiency, which is demonstrated to be almost as high for PbS NCs as for CdSe/ZnS ones.

References

[1] E F Schubert and J K Kim, Science **308**, 1274 (2005)

[2] J Y Tsao, IEEE Circuits & Devices **20**, 28 (2004)

[3] A Bergh, G Craford, A Duggal, and R Haitz, Physics Today **54**, 42 (2001)

[4] F A Ponce and D P Bour, Nature (London) **386**, 351 (1997)

[5] D V Talapin, A L Rogach, A Kornowski, M Haase, and H Weller, Nano Lett. **1**, 207 (2001)

[6] S Nizamoglu and H V Demir, Nanotechnology 18, 405702 (2007)

[7] M A Hines and G D Scholes, Adv. Mater. **15**, 1844 (2003)

Nanostructures and Quantum Devices (Posters)

Widely Tunable and Intense Mid-Infrared PL Emission from Epitaxial Pb(Sr)Te Quantum Dots in a CdTe Matrix

S. Kriechbaumer[1], T. Schwarzl[1], H. Groiss[1], W. Heiss[1], F. Schäffler[1],T. Wojtowicz[2], K. Koike[3], M. Yano[3], and G. Springholz[1]

[1] Institut für Halbleiter- und Festkörperphysik, Universität Linz, Austria

[2] Institute of Physics, Polish Academy of Sciences, Warsaw, Poland

[3] Osaka Institute of Technology, Asahi-ku Ohmiya, Osaka 535-8585, Japan

We present the temperature dependence of the mid-infrared PL of epitaxially precipitated PbTe/CdTe QDs for different dot sizes. A strong shift of the emission to longer wavelengths with decreasing temperature is found and explained by a theoretical model of the ground state transition energy. Secondly, we demonstrate that $Pb_{0.93}Sr_{0.07}Te$ ternary QDs also give strong PL emission at room temperature, thus extending the size tunability of such epitaxially precipitated dots. In addition, we showed that size control is also obtained for a fixed layer thickness by variation of the growth temperature.

Introduction

Epitaxial semiconductor quantum dots (QDs) are of great importance for optoelectronic devices. Their conventional synthesis uses the Stranski-Krastanow growth mode for strained layer heteroepitaxy with efficient interband emission mostly found in the visible and near-infrared spectral regions. Recently, we have demonstrated a completely different approach for the synthesis of epitaxial QDs for the mid-infrared (MIR). It is based on phase separation between two lattice-type mismatched, immiscible materials, namely PbTe (rock salt lattice) and CdTe (zinc blende lattice). Upon thermal annealing, 2D PbTe layers grown by molecular beam epitaxy within CdTe barrier layers are transformed into PbTe QD nano-precipitates with highly symmetric almost spherical shapes and atomically sharp hetero-interfaces. These defect-free QDs show continuous-wave photo-luminescence (cw-PL) with high efficiency even at room temperature [1], [2]. Moreover, due to the very small strain in the dots (lattice mismatch only 0.29% at 300 K) and the narrow band gap of bulk-like PbTe of 320 meV (3.85 µm), the optical emission is in the MIR. We are also able to control the dot sizes and the vertical positions of the dots to a large extent [3]. The lead salts have widely been applied for fabrication of MIR lasers and detectors for gas spectroscopy due to their favorite band structure and low Auger recombination rates.

Sample Structure and Experimental Details

The samples were grown by MBE using solid source CdTe, PbTe, Cd, and Te effusion cells on (100)-oriented GaAs substrates. On a CdTe buffer layer, PbTe and PbSnTe layers with different thicknesses were deposited using a low growth temperature of 220 °C to ensure a two-dimensional growth without island formation. A 50 nm CdTe cap layer was grown on top to form a PbTe quantum well.

By in-situ and post-growth thermal annealing in inert N_2 atmosphere, the PbTe quantum well layers are transformed into isolated quantum dot nano-precipitates [1], [2] due to the immiscibility of PbTe and CdTe. The annealing conditions (duration and temperature) were optimized for each sample to achieve the highest cw-PL intensity at room temperature. As shown by TEM [1] – [3], the annealed dots have a centrosymmetric shape of a small-rhombo-cubo-octahedron which is the dot shape in thermal equilibrium (minimization of interface energies). From the TEM investigations, we also know that the dots are essentially defect free and exhibit atomically sharp hetero-interfaces.

The PL measurements were done with cw diode lasers with wavelengths between 980 nm and 1480 nm and output powers of up to 245 mW. Therefore, only the PbTe dots and not the CdTe barriers are excited. The pump laser was focused on the sample placed in a He flow cryostat under an angle of 45°, and the PL emission was recorded by lock-in technique with a liquid-nitrogen-cooled InSb infrared detector mounted on a grating spectrometer.

Results

In this work, at first, we present the temperature dependence of the cw PL of PbTe/CdTe QDs for different dot sizes. A strong shift of the emission to longer wavelengths with decreasing temperature is found for both dot sizes (see Fig. 1).

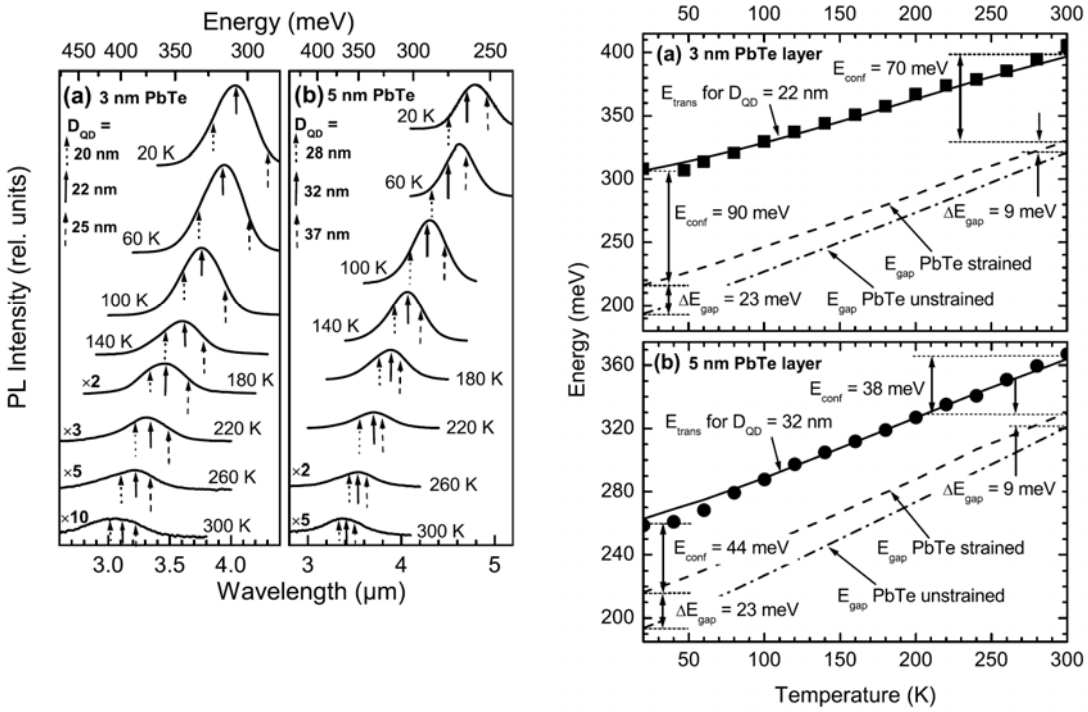

Fig. 1: (left:) Temperature dependent cw-PL spectra for PbTe/CdTe quantum dots formed by an initially (a) 3 nm and (b) 5 nm thick PbTe layer. The arrows depict the calculated ground state transition energy for different dot diameters D_{QD} as indicated.
(right:) Peak energy of the PL emission spectra as a function of temperature (symbols) for (a) 3 nm and (b) 5 nm PbTe. The full, dashed and dash-dotted lines depict the calculation of the ground state transition energy for (a) 22 nm and (b) 32 nm dot diameter, the band gap of isotropically strained PbTe, and the band gap of bulk-like PbTe, respectively.

This shift is not just explained by the strong temperature dependence of the band gap of PbTe, but also by the strain in the dot as well as by the high quantum confinement (ΔE_g(PbTe-CdTe) = 1.2 eV), both being temperature dependent via the lattice mismatch and the effective masses of PbTe. We also observed an increase of the emission intensity with rising temperature for temperatures below 55 K or 100 K, depending on dot size (Fig. 2 (left)). This is attributed to the presence of a dark ground state lying below the bright state as was also observed for other quantum dots. The influence of the excitation power on the emission spectra at various temperatures (Fig. 2 (right)) indicates a carrier redistribution between the dots, which could also explain the observation of Fig. 2 (left).

Furthermore, a calculation of the transition energy responsible for the PL emission is presented. We make use of the fact that the ground state transition in a spherical dot with finite barriers can exactly be calculated using the results for the first excited state in a quantum well with the same size. We also include the strain in the dots as well as in the matrix and the anisotropic effective masses of PbTe, both being temperature dependent, and by that we obtain a good agreement to the experimental data as seen in Fig. 1.

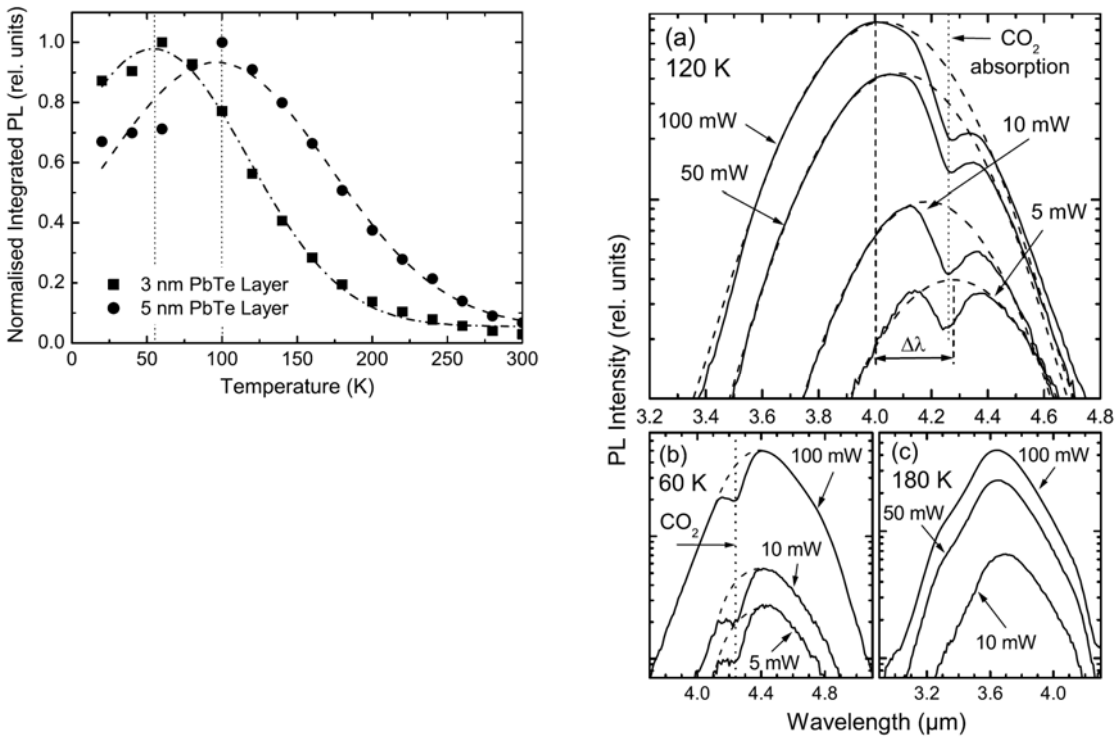

Fig. 2: (left:) Normalized integrated PL intensity vs. temperature for PbTe/CdTe dots with a 3 nm (squares) and a 5 nm thick PbTe layer (circles). The lines are guides to the eye.
(right:) Excitation power dependent PL spectra at different temperatures of (a) 120 K, (b) 60 K and (c) 180 K on a logarithmic scale. The dips at 4.25 μm indicated by the dotted line arise from residual CO_2 absorption in the optical measurement path. The dashed lines are Gaussian line fits to the data.

Secondly, we demonstrate for the first time $Pb_{0.93}Sr_{0.07}Te$ ternary QDs also giving strong PL emission at room temperature. Due to the increasing band gap with increasing Sr content, this leads to a larger tunability of the emission towards shorter wavelengths. Remarkably, for originally 1 nm thin PbSrTe layers, the PL signal is much

stronger as compared to a 1 nm PbTe reference dot sample, despite the shorter emission wavelength for the PbSrTe sample. We also observed for thin PbSrTe layers that the blue shift with regard to the bulk band gap is much lower as expected indicating that part of the Sr is incorporated in the CdTe matrix material.

In addition, we show that it is possible to fabricate high quality PbTe dots by simply growing 50 – 300 nm thick ternary $Cd_{1-x}Pb_xTe$ layers with Pb-contents of 1 % to 6 %. The strong PL emission at room temperature is peaked at about 2 – 2.3 µm indicating a rather small average dot size of 9 – 11 nm in diameter depending on the actual Pb content. Recently, we showed that the size of the PbTe dots can effectively be tuned by the original 2D PbTe layer thickness [3]. In addition to that, we demonstrate here that size control is also obtained for a fixed layer thickness by variation of the growth temperature (see Fig. 3). For a nominally 1 nm PbTe layer, dots with average diameter of 10 nm for 300 °C and of 15 nm for 400 °C growth temperature are found.

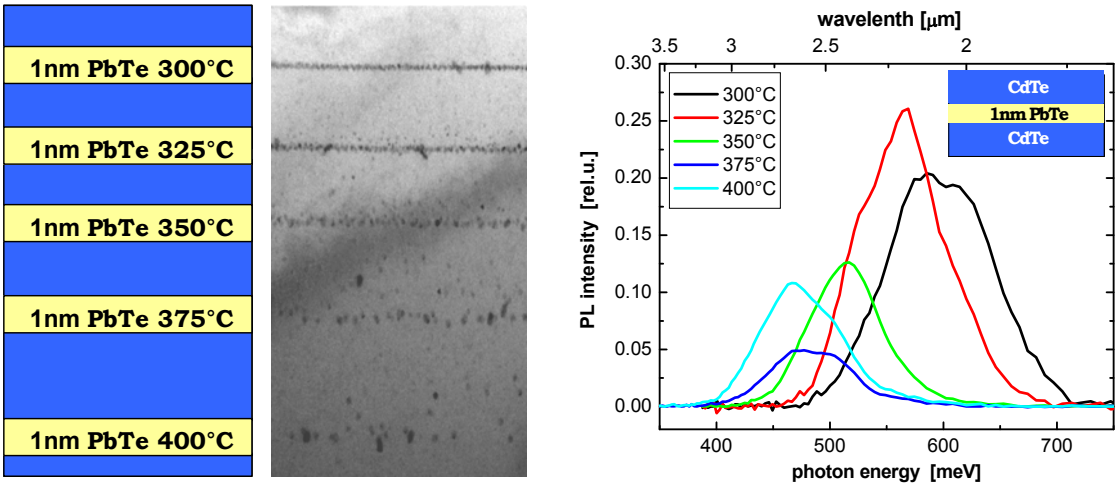

(a) (b)

Fig. 3: (a) TEM image of a sample with 1 nm PbTe layers in CdTe grown at different temperatures with a sketch of the sample structure. (b) Room temperature cw PL emission spectra of five individually grown 1 nm PbTe layers grown at different substrate temperatures demonstrating a longer wavelength emission for samples grown at higher temperatures. This indicates a larger dot size for higher growth temperatures as also seen in the TEM image.

Conclusion

We presented the temperature dependence of the cw PL of epitaxially precipitated PbTe/CdTe QDs for different dot sizes. A strong shift of the emission to longer wavelengths with decreasing temperature is found and explained by a theoretical model of the ground state transition energy. Secondly, we demonstrated that $Pb_{0.93}Sr_{0.07}Te$ ternary QDs also give strong PL emission at room temperature, thus extending the size tunability of such epitaxially precipitated dots. In addition, we showed that size control is also obtained for a fixed layer thickness by variation of the growth temperature.

Acknowledgements

This work was supported by the Austrian Science Fund (SFB IR-ON, L303).

References

[1] W. Heiss, H. Groiss, E. Kaufmann, G. Hesser, M. Böberl, G. Springholz, F. Schäffler, K. Koike, H. Harada, M. Yano, Appl. Phys. Lett. **88**, 192109 (2006).

[2] W. Heiss, H. Groiss, E. Kaufmann, G. Hesser, M. Böberl, G. Springholz, F. Schäffler, R. Leitsmann, F. Bechstedt, K. Koike, et al., J. Appl. Phys. **101**, 081723 (2007).

[3] H. Groiss, E. Kaufmann, G. Springholz, T. Schwarzl, G. Hesser, F. Schäffler, W. Heiss, K. Koike, T. Itakura, T. Hotei, et al., Appl. Phys. Lett. **91**, 222106 (2007).

Coupled Surface States in Thin, Frequency Dependent Layers

M. Bergmair[1], K. Hingerl[2]

[1] CD Labor für oberflächenoptische Methoden, Institut für Halbleiter- und Festkörperphysik, Universität Linz – Austria

[2] ZONA, Universität Linz - Austria

In photonic crystals made of materials with a frequency dependent dielectric function surface plasmon modes are extending over some adjacent layers and it turns out, that the dispersion can be tailored by coupling surface plasmons of adjacent layers. To give a detailed study we start investigating surface plasmons on a single metallic sheet. The mode dispersion is not bijective any more (i.e. is bent back) due to the coupling of surface plasmons and radiative modes, and the group velocity diverges and is even negative. This effect is still physical as the absorption of the metal influences the properties of the surface plasmons and yields an inequality between group and energy velocity. Next to these effects we investigate the propagation distance of the surface states and optimize them by varying the thickness of the layers. Finally we calculate the dispersion for two adjacent layers to see possible coupling effects.

Introduction

Photonic crystals (PC) have been investigated for two decades theoretically and experientially as they allow to model the dispersion of this artificial material according to the needs and interests [1].

A very efficient approach was presented by Kuzmiak et al. by using metal in one and two-dimensional PCs [2]. In the one-dimensional case the large imaginary part (and via Kramers-Kronig relations negative real part) of the dielectric function below the plasma frequency leads to the formation of additional band gaps which comes clearly from absorption. This absorption band gap can be controlled by the thickness of the metallic layers (i.e. the filling factor) and the penetration depth is much smaller in this absorption band gap than in the band gaps arising from the structure and dielectric difference of the two composites. Further, it turns out (for example by studying a polaritonic PC where one material has a Lorentzian dielectric function) that these absorption band gaps are omnidirectional for both polarizations and angles of incidence [3].

In material with a negative dielectric function also surface plasmons can be excited [4]. These modes lie below the light line and are propagating almost parallel to the surface of a metal. Surface plasmons have a huge potential in applications as their coupling to free space is forbidden without any structural changes (like a grating). They can be guided, e.g., by a bent metallic ridge.

In this work we study surface plasmons on metallic interfaces as it was done in [5] (without damping) and [6] (for one silver layer) for some parallel layers and compare the resulting solutions with the dispersion of the surface plasmons in a metallic PC. We are also interested in the coupling effects of different modes in different frequency regions which results in a negative and back bent dispersion. Further we investigate the propagation length of surface plasmons on a single film with respect to the layer thickness.

The group velocity becomes negative and infinite. We study the expressions of the group and energy velocity and show that in absorbative systems the group velocity loses its meaning.

Surface Plasmons in Thin Films

Surface plasmons on a single metal-air interface are described by

$k_y = \omega(\varepsilon_b\varepsilon(\omega)/(\varepsilon_b\ \varepsilon(\omega))^{1/2}$.

In this equation k_y is the in-plane component of the wave vector, ω the frequency and ε_b and $\varepsilon(\omega)$the dielectric function of the background and the metal, respectively. In our contribution we will follow literature and use the Drude model to describe the metal. By doing so we obtain different modes, namely bound surface modes below $\omega_a := \omega_p/\sqrt{2}$, quasi bound modes between ω_a and the plasma frequency ω_p and radiative modes above ω_p (see [6]). The quasi bound modes result from the coupling of surface modes with the radiative ones and are only obtained by taking the imaginary part of the Drude dielectric function into account. This coupling results in a negative dispersion which is therefore connected to a large damping via the Kramers-Kronig relations. Therefore these quasi bound modes only propagate small distances which can be optimized by changing the thickness of the metallic film.

A thin metallic film shows two solutions (symmetric and antisymmetric) which are obtained from an implicit equation:

$\varepsilon(\omega)k_b/\varepsilon_b k_m = -\tanh(k_m d/2) = -\operatorname{ctanh}(k_m d/2)$

In this equation k_m and k_b indicate the normal component of the wave vector in the metal or the background, respectively. With the help of a Nelder-Mead minimization algorithm [8] one obtains both solutions for arbitrary thickness and damping of the metallic film. The solutions were often discussed in literature [5], [7] and therefore we mention that one solution is strongly damped whereas the other one shows small damping and is quite similar to the mode on a single interface except that the asymptotic frequency ω_a shifts towards ω_p by decreasing the thickness of the film.

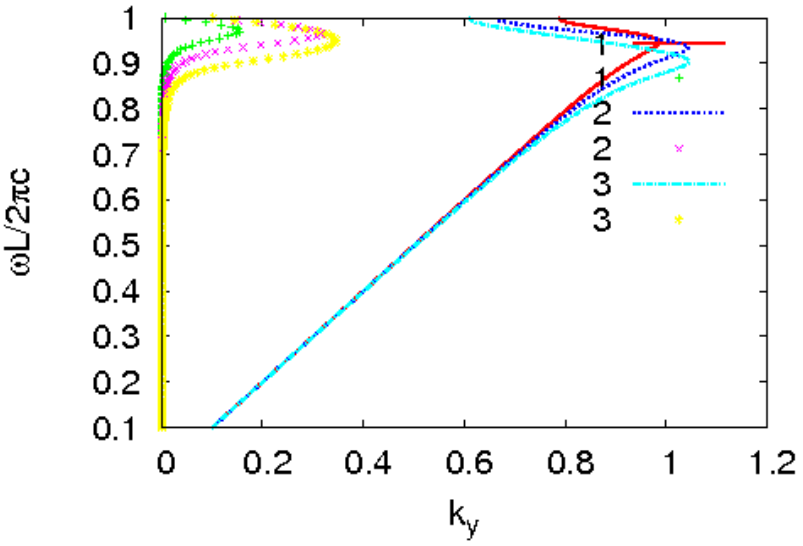

Fig. 1: The hardly damped solutions for one (red), two (blue) and three layers (turquoise). The imaginary part of the dispersion is displayed in green, magenta and yellow for one, two and three adjacent sheets, respectively. The thickness of the metallic film is always kept constant.

Adding a second metallic sheet parallel to the first one allows to study the coupling of surface plasmons. The four solutions can again be obtained from an implicit equation

$A^4\text{-}V\,A^2 + e^{-4kmd}$

with $A = (k_b\,\varepsilon(\omega) - k_m\varepsilon_b)/(k_b\,\varepsilon(\omega) + k_m\varepsilon_b)$ and $V = 2e^{-2kmd} + e^{-2kbL}(1-e^{-2kmd})^2$. We solve this equation again by the Nelder-Mead algorithm. In Fig. 1 the thickness of the layers is $d = 0.1\ \omega_p$ and the distance between the sheets is $L = \lambda_P$ (which is the free space wavelength of the plasma frequency).

One can see that the damping increases for an increasing number of layers (green, pink and yellow dots) and the asymptotic frequency in the real part of the dispersion goes towards $\omega_p/\sqrt{2}$ (red, blue, cyan curves). For each additional layer more the number of solutions increases by a factor of two which should lead to an infinite number of surface plasmon solutions in the metallic PC. The surface modes in the PC are obtained by determining the solutions for a fixed value of the Bloch wave vector (in [3] the solution for $k_{Bloch} = 0$ is presented which is almost similar to the solution on a single interface). In [5] it is suggested that the solutions for an infinite amount of parallel metallic sheets the solutions should lie in an area which is bounded by $k_{Bloch} = 0$ and $k_{Bloch} = \pi/L$.

Group Velocity

In the previous section we saw that the coupling of the bounded and the radiative mode yield a negative, back bent dispersion. The group velocity, which is defined by $v_g = d\omega/dk$, is therefore negative and at certain points infinite which is of course unphysical. Many authors have shown that in absorbing systems such superluminal effects are obtained (e.g. see [9]).

We show here that by studying Poyntings theorem S = E x H and the resulting continuity equation

$-\mathrm{div}(S) = d/dt\ u + j\,E$

one finds that the energy velocity is not equal to the group velocity (which is unphysical at certain points) as the energy density reads [10] in first approximation

$u \sim d\,(\varepsilon(\omega)\,\omega)/d(\omega).$

Due to the imaginary part of the dielectric function of the metal this inequality arises and additional terms contribute to the expression for the energy velocity. Therefore the group velocity looses its meaning for absorbing materials.

Conclusion

In our contribution we have studied the negative dispersion of surface plasmons which arises from the coupling of bound and radiative modes. The negative dispersion results in unphysical values for the group velocity. We have pointed out that the group velocity becomes meaningless in absorbing systems as additional terms modify the expression for the energy velocity. Further we have investigated how the dispersion of surface plasmons changes for parallel metallic layers and have compared these modes with surface plasmons in a metallic photonic crystal.

Acknowledgements

The authors are thankful for two EC grants (N2T2 and NanoCharM). Further they thank Johann Messner from the University Linz (Supercomputer Department).

References

[1] J. Joannopoulos, R. Meade, and J. Winn, Photonic Crystals . Princeton University Press, 1995.

[2] V. Kuzmiak and A. Maradudin, “Photonic band structure of one- and two-dimensional periodic systems with metallic components in the presence of dissipatation,” Physical Review B , vol. 55, pp. 7427–7444, 1997.

[3] M. Bergmair, M. Huber, and K. Hingerl, “Band structure, wiener bounds, and coupled surface plasmons in one dimensional photonic crystals,” Applied Physics Letters , vol. 89, p. 081907, 2006.

[4] H. Raether, Surface Plasmons on Smooth and Rough Surfaces and on Grantings . Springer, Berlin, 1988.

[5] E. N. Economou, “Surface plasmons in thin films,” Phys. Rev. , vol. 182, pp. 539–554, Jun 1969.

[6] J. Dionne, L. Sweatlock, H. Atwater, and A. Polman, “Planar metal plasmon waveguides: frequencydependent dispersion, propagation, localization, and loss beyond the free electron model,” Physical Review B , vol. 72, p. 075405, 2005.

[7] A. Zayats, I. Smolyaninov, and A. Maradudin, “Nano-optics of surface plasmon polaritons,” Physics Reports , vol. 408, pp. 131–314, 2005.

[8] J. Nelder and R. Mead, “A simplex method for function minimization,” The Computer Journal , vol. 7, p. 308, 1964.

[9] E. Bolda, R. Chiao, and J. Garrison, “Two theorems for the group velocity in dispersive media,” Physical Review A , vol. 48, p. 3890, 1993.

[10] L. Landau and E. Lifschitz, Lehrbuch der theoretischen Physik: VIII . Berlin: Akademie Verlag, 3 ed., 1974.

Intraband Auger Effect in InAs/InGaAlAs/InP Quantum Dot Structures

T. Gebhard[1], D. Alvarenga[2], P.L. Souza[3], P.S.S. Guimarães[2], K. Unterrainer[1], M.P. Pires[4], G.S. Vieira[5], and J.M. Villas Boas[6]

[1]Center for Micro & Nanostructures, TU, Vienna, Austria
[2] Departamento de Fisica, UFMG, Belo Horizonte, Brazil
[3] LabSem/CETUC, PUC, Rio de Janeiro, Brazil
[4] Instituto de Fisica, UFRJ, Rio de Janeiro, Brazil
[5] Divisão de Fisica Aplicada, IEA, São José dos Campos, Brazil
[6]Walter Schottky Institute, TU, Munich, Germany

Intraband photocurrent and absorption measurements were performed on InAs/InGaAlAs/InP quantum dot structures. A full three-dimensional theoretical model has been employed to identify the observed PC as a bound to bound transition, where the final state is about 200 meV deep below the conduction band continuum. The reported results strongly suggest that an Auger process plays a fundamental role in generating the observed intraband photocurrent.

Introduction

Semiconductor quantum dot (QD) structures have raised much interest in the past years for application in mid-infrared photodetection due to their potential for efficiently coupling normal incident light and for higher operation temperature as compared to quantum well structures [1] – [6]. For most of the QD structures the intraband optical transitions occurs in the 5-20 μm range between a bound to bound or a bound to quasibound state. Beside the fact that they produce more selective detectors, they require an extra carrier transport mechanism to generate the observed photocurrent (PC) and this is attributed to thermal excitations even for deep final bound states [1] – [4]. Another possibility to extract the carriers from the final bound energy state to the continuum, where they can easily participate in the PC, is via an Auger effect.

Theoretical studies in the 90's showed that inter- and intraband Auger scattering in quantum dots are very effective processes [7]. The activation of photoexcited electrons by Auger scattering in interband transitions has been shown experimentally for InAs/InP QD structures [2] and Auger scattering in undoped and n- and p-type doped InGaAs quantum dots was theoretically investigated in [9]. However, experimental evidence of the Auger effect on intraband transitions has not yet been reported. In this communication we present results that demonstrate that Auger processes can indeed play a fundamental role in generating an intraband PC, broadening the possibilities for designing QD structures for highly selective mid-infrared photodetectors.

Experiment and Discussion

The samples under investigation are grown on a 150 nm thick InP buffer layer deposited at 630 °C on a semi-insulating InP substrate followed by a 500 nm thick n-doped lattice matched InGaAs layer acting as the bottom contact. Afterwards a 109 nm thick

lattice matched layer of InGaAlAs is grown with 16% Al content. The InAs QDs are then deposited for 5.5 s at 520 °C and they are annealed in an arsine atmosphere for 12 s. They are covered by a 16 nm thick InP layer while the temperature is ramped up to 600 °C. This sequence is repeated for 10 times. A last 109 nm thick layer of the quaternary material is then grown and finally a 250 nm *n*-doped InGaAs contact layer is deposited. The doping level at the contact layers is 1.0 x 10^{18} cm^{-3}. All ternary and quaternary layers are grown at 600 °C. The QD samples were grown with three different doping levels: one nominally undoped sample and 2 samples with 2 and 4 electrons respectively. The composition of the quaternary material was chosen so as to maximize the dot density [11]. Using atomic force microscopy (AFM) average dot height and density of 9 nm and 1.5 x 10^{10} respectively has been measured on uncapped QD control samples. Transmission electron microscopy (TEM) images showed lens shaped QDs with a base diameter of approximately 60 nm and confirmed the QD height average of 9 nm.

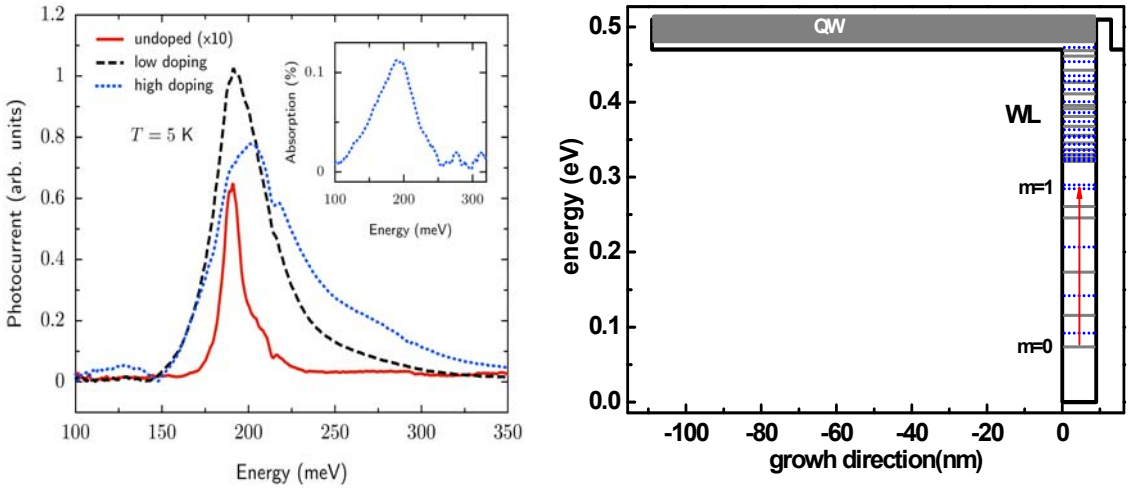

(a) (b)

Fig. 1: (a): PC response for different doping; the inset shows the absorption with respect to InP substrate at 5K. (b): Conduction band structure profile and calculated energy levels for the investigated samples for quantum numbers m = 0 (solid lines) and m = 1 (dashed lines). The arrows show the optical transitions for which the oscillator strength is largest. The WL-layer states are also shown.

Photocurrent (PC) and absorption measurements were performed using Fourier Transform Infrared Spectroscopy (FTIR). Figure 1 (a) shows the photocurrent spectra at 5 K for the investigated samples measured with the FTIR with normal incident light and no external bias. A narrow PC peak is observed around 190 meV for the undoped sample. The sample is nominally undoped, but the presence of residual doping and carrier diffusion from the contacts leads to a population of the QD so that intraband absorption can occur. A ten times stronger and three times broader signal was observed for the same structure with a doping of about 2 and 4 electrons per dot. The broadening of the PC-peak as a function of doping can be explained by the inhomogeneous broadening of the quantum dot sizes. The ground state of large QD lies deeper in energy, so if the doping is low, only a small fraction of the QDs get populated. But broadening also occurs if higher QD states get populated due to higher doping. Absorption measurements were performed in order to confirm the results. They where done in waveguide geometry using the same structures as for the PC measurement but with 20 layers instead of 10 layers. A peak centered around 185 meV – 195 meV has been observed in nice agreement with the PC spectra (inset Fig. 1 (a)).

An effective mass model was applied in a theoretical calculation assuming lens shape for the QD (according to the TEM images) and where the physical parameters were taken from [12]. A more sophisticated treatment about the theoretical model can be found in [11]. The results of the calculations can be seen in Fig. 2 (b). The solutions for the quantum numbers 0 (solid line) and 1 (dashed line) are superimposed to the QD structure profile. The transition between the ground state and the fourth excited state, corresponding to energy of 197 meV, turned out to be the strongest. For the absorption of normal incoming light a change in angular momentum is necessary. Now the important point to note is that the final state of this transition is still 200 meV from the continuum that implies that the excited electrons cannot contribute directly to the PC.

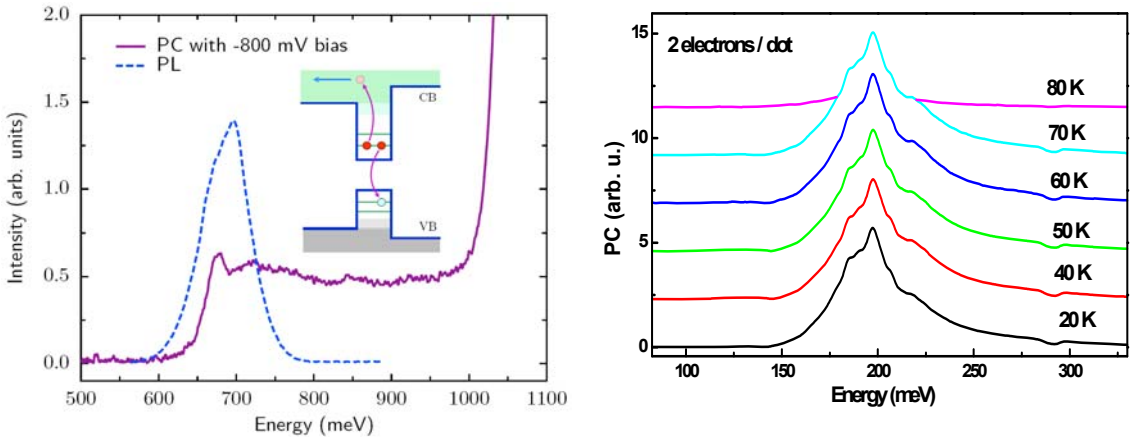

(a) (b)

Fig. 2: (a): PL (solid line) and interband PC (dotted line) spectra for the undoped sample at 80 K. PC spectra at 70 K (dash-dotted line) and 60 K (dashed line) are also shown. The inset illustrates the intraband and interband Auger. (b): Temperature dependence of the medium doped sample. The amplitude stays constant up to 70 K.

Comparing the photoluminescence (PL) (Fig. 2 (a), dashed line) with the interband PC (solid line) at 80 K a clear contribution from the QDs can be observed around 700 meV. This gives further support that the intraband PC comes from the absorption of a transition deep inside the QD. As has been clamed by Landin et al. [8] the interband PC from the QDs is produced by an interband Auger effect, where the photo-excited electron receives additional energy from the recombination of another electron with the photo-generated hole. A scheme of such a process is depicted in the inset of Fig. 2 (a).

The final state of the intraband transition that produces the PC is 200 meV below the contiunuum. The thermal energy is very small at low temperature so that thermal assisted extraction of such photo-excited carriers gets inefficient. The amplitude of the PC as a function of temperature shows nearly no dependence on temperature between 5 and 60 K (Fig. 2 (b)). This behavior can be explained by Auger scattering as a temperature independent process. A photo-excited electron can be promoted to the continuum by an energy transfer from an electron that relaxes from a higher energy state down to the ground state. The suggested intraband Auger scattering can be seen schematically in in the inset of Fig. 2 (b). The theoretical calculation showed that there are many possible states available to participate to this process. One should also consider that the FTIR measurement is done with a broadband light source that increases the possibility to have two electrons in a dot simultaneously excited.

Dynamical processes in the device could cause a non-vanishing population of higher states. The dark current in the devices is a result of thermal emission and re-capture of

electrons. Time resolved measurements showed that electron capture occurs very fast into high lying states and is then slowed down for lower lying states [13]. As a consequence we can expect that higher lying states are populated.

Conclusion

In summary, we have carried out a detailed study of the intraband optical response of quantum dot structures for mid-infrared photodetection in order to verify the possibility of carriers in a rather deep bound state generating a photocurrent. The obtained photocurrent and absorption results, together with a realistic theoretical calculation, strongly suggest that an Auger process can produce a significant current. Photoluminescence together with interband photocurrent further supports this attribution. The reported results indicate that quantum dot photodetector structures could be designed to operate based on the more selective bound-to-bound transitions of quantum dots and still produce an efficient device.

Acknowledgements

We thank I. G. Solórzano and H. F. Filho for the TEM and AFM measurements. This work has benefited from fruitful discussions with G. Bastard. Financial support from the WPI, FWF SFB IR-ON, EC NoE SANDIE, CAPES, CNPq, FINEP, FAPERJ and FAPEMIG is acknowledged. JVB is supported by the Alexander von Humboldt Foundation.

References

[1] Lim H, Zhang W, Tsao S, Sills T, Szafraniec J, Mi K, Movaghar B, Razeghi M, Phys. Rev. B 72, 085332 (2005).

[2] Liu H C, Opto-electronics Rev. 11, 1 (2003).

[3] Boucaud P, Sauvage S, C. R. Physique 4, 1133 (2003).

[4] Towe E, Pan D, IEEE J. Sel. Topics Quantum Electronics 6, 408 (2000).

[5] Bhattacharya P, Su X H, Chakrabarti S, Ariyawansa G, Perera A G U, Appl. Phys. Lett. 86, 191106 (2005).

[6] Chakrabarti S, Stiff-Roberts A D, Su X H, Bhattacharya P, Ariyawansa G, Perera A G U, J. Phys. D: Appl. Phys. 38, 2135 (2005).

[7] Pan J L, Phys Rev. B 49, 11272 (1994).

[8] Landin L, Pettersson H, Kleverman M, Borgström M, Zhang X, Seifert W and Samuelson L, J. Appl. Phys. 95, 8007 (2004).

[9] Nilsson H H, Zhang J Z, Galbraith I, Appl. Phys. Lett. 91, 161113 (2007).

[10] Borgström M, Pires M P, Bryllert T, Landi S M, Seifert W, Souza P L, Journal of Crystal Growth 252, 481 (2003).

[11] Souza P L, Gebhard T, Lopes A J, Pires M P, Villas-Boas J M, Unterrainer K, Guimarães P S S, Vieira G S and Studart N, Appl. Phys. Lett. 90, 173510 (2007).

[12] Vurgaftman I, Meyer J R and Ram-Mohan L R, J. Appl. Phys. 89, 5816 (2001).

[13] Müller T, Schrey F F, Strasser G, and Unterrainer K, Appl. Phys. Lett. 83, 3572 2003

Quantitative Scanning Capacitance Microscopy on Buried InAs Quantum Dots

J. Smoliner, W. Brezna, A.M. Andrews, G. Strasser

Institut für Festkörperelektronik, TU-Wien
Floragasse 7, A-1040 Wien, Austria

InAs self assembled quantum dots embedded in GaAs *n* − *i*−Schottky diodes were imaged by quantitative scanning capacitance microscopy. As these measurements are extremely sensitive to light, a modified AFM feedback procedure was developed, where the AFM laser can be turned off up to several seconds while the AFM feedback loop keeps running.

The InAs quantum dot samples we used for our capacitance studies were initially designed for photocurrent spectroscopy, and had the following layer structure: on a highly doped *n*-doped back contact, a 40 nm i-GaAs layer was grown. On top, 1.55 ML of InAs were deposited at 500 °C followed by 80 nm of *i*-GaAs, a 40 nm thick AlGaAs blocking barrier (Al concentration 30%), and a 10 nm GaAs capping layer. The nominal dot density was in the order of 500 μm^{-2}.

In the low frequency (f = 1 kHz) capacitance images, InAs dots are clearly visible. The dot size in the capacitance images is larger compared to what was expected for the geometrical size, which we attribute to the fact that the dots are located 130 nm below the sample surface. A contrast rich capacitance landscape is also revealed in between the dots, which we attribute to local thickness variations of the InAs wetting layer. We also find that the image contrast depends on sample bias. A systematical measurement yielded best contrast at a sample bias of –0.6 V, which approximately corresponds to flatband conditions.

In addition to the images, capacitance spectra were recorded at on-dot and off-dot positions, which exhibit a clearly different behavior. At off-dot positions, the capacitance increases monotonically in forward bias direction, as it is expected for the capacitance of a Schottky contact on semiconductors. On contrast to that, one clear minimum and a step-like feature is observed in the capacitance spectra at on-dot positions. Attributing these features to a sequential filling of the dot states, the level spacing can be determined. For our sample, we obtain an energy spacing of 46 meV between the lowest levels, which is in reasonably good agreement with previous results of optical measurements.

Characterization of Nanowires

M. Keplinger[1], D. Kriegner[1], B. Mandl[1, 2], J. Stangl[1], V. Chamard[3], E. Wintersberger[1], R.T. Lechner[1], D. Hufnagl[1], and G. Bauer[1]

[1] Institut für Halbleiter- und Festkörperphysik, Johannes Kepler Universität Linz, Altenbergerstrasse 69, 4040 Linz, Austria
[2] Solid State Physics, Lund University, Professorsgatan 1, 22100 Lund, Sweden.
[3] Université P. Cezanne Aix-Marseille III, CEDEX 20, 13397 Marseille, France.

Semiconductor nanowires have attracted attention in recent years due to their unique electronical and structural properties. Such structures provide one-dimensional electronic material and the possibility to connect single quantum dots, which are zero-dimensional electronic structures. In addition, nanowires exhibit interesting mechanical properties which make new, so far not studied combinations of materials possible. The most significant demonstration of this possibility is the growth of III-V nanowires on Si substrates [1], [2]. Since such structures are interesting for fundamental science as well as for applications, a thorough study of the material properties and the material quality is needed. We show x-ray techniques for nanowires analysis, to investigate epitaxial orientation of the wires, chemical composition, and crystal structure (zinc-blende, wurtzite) of nanowires.

Introduction

The nanowires are grown in a low pressure metal organic vapor phase epitaxy system, mainly using a gold-free nucleation process for $InAs_{1-x}P_x$, and a gold nucleation center for InP nanowires. In both cases, hexagonal wires grown in [111] direction perpendicular to the sample surface are obtained. Figure 1 gives an impression of the nanowire shape and arrangement from scanning electron microscopy. The results of x-ray characterization on these nanowires are presented in the following.

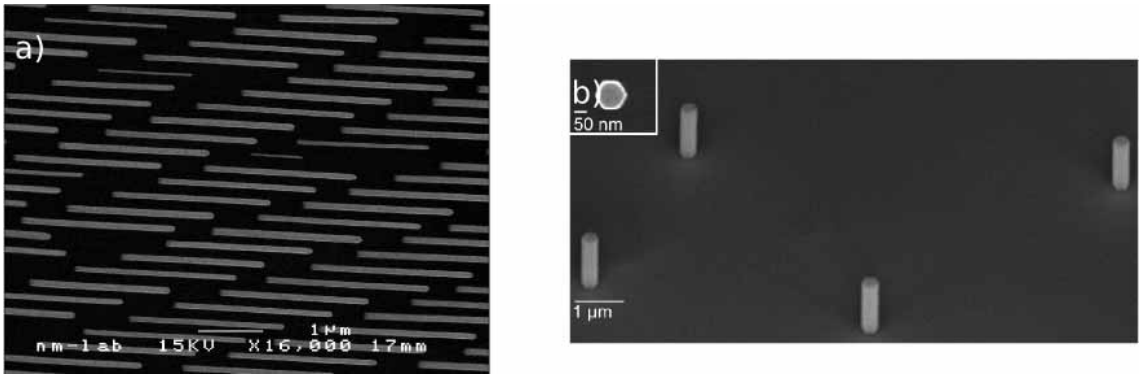

Fig. 1: (a) InAs nanowires grown on a pre-structured InP (111)B substrate. Image tilted by 45°. (b) InAs nanowires randomly nucleated on an InP (111)B substrate. Image tilted by 45°. Inset: top view of a nanowire, showing its hexagonal shape.

P Concentration of InAsP Wires from High Angle X-Ray Diffraction

InAsP nanowires were grown at constant PH flow and temperatures from 520 to 640 °C on an InP (111)B substrate. The wires grow in [111] direction and therefore perpendicular to the substrate surface.

Asymmetric high angle x-ray diffraction maps around the (224) peak of InP were measured to determine the As content and degree of relaxation of the wires. The measurements were performed at the Seifert XRD 3003 laboratory source. Reciprocal space maps (RSM) of two samples grown at different temperatures are shown in Fig. 2 (a) and (b). The reference sample in (a) was grown at zero PH flow.

For a series of samples the As content was determined and plotted against the growth temperature (c). From the RSM it is obvious that the grown wires are relaxed to their bulk lattice parameter. Furthermore, we see that the P content increases with increasing growth temperature. In this way a P content from 13% to 24% could be realized.

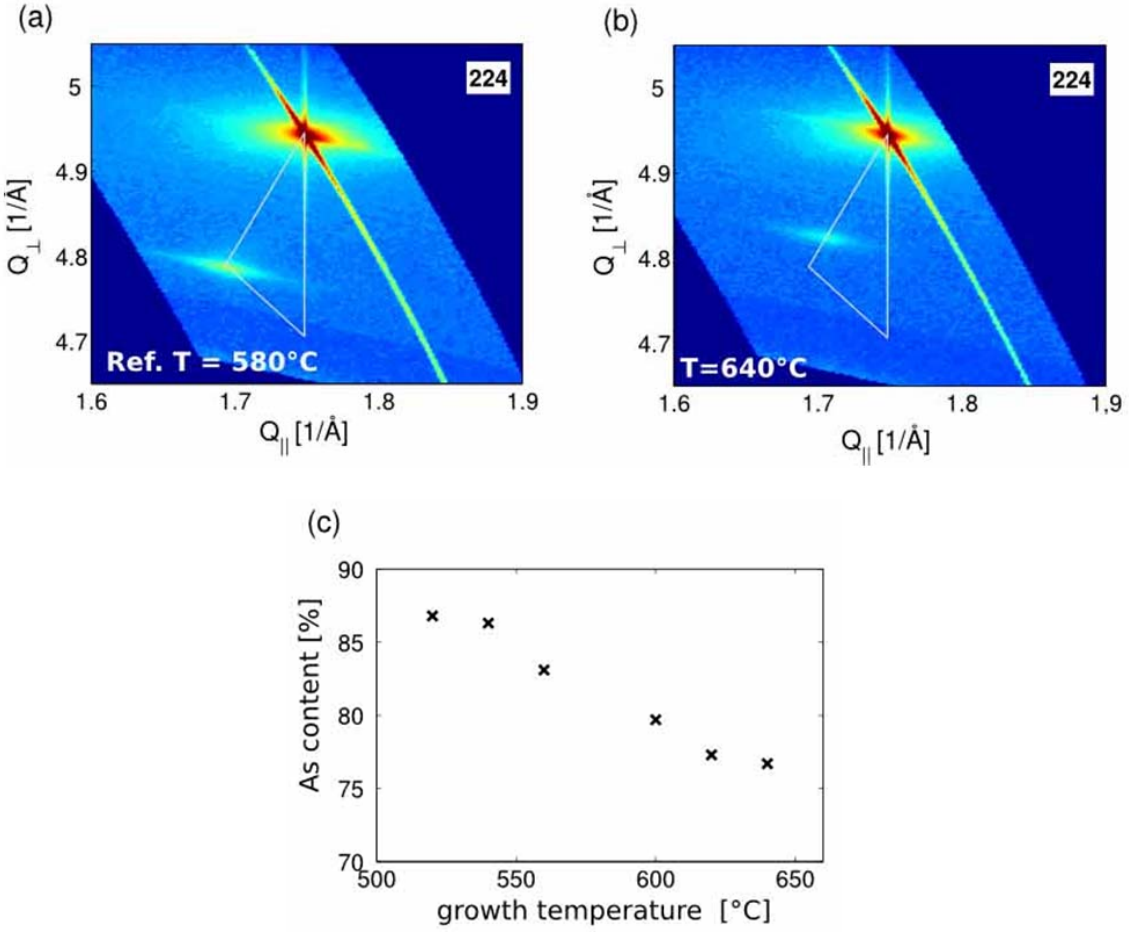

Fig. 2 (a) and (b): RSMs around the (224) Bragg peak of samples with different growth temperatures. (c): Deduced As content, plotted over different growth temperatures. The white triangle denotes possible peak position due to the InAsP wires, depending on P content and strain state.

Wurtzite to Zinc-Blende Ratio in Wire Ensembles

Although for the nanowire material in bulk form zinc-blende (ZB) is the stable crystal structure, in nanowires also wurtzite (WZ) lattice is observed. This differs from the zinc-blende only by a change of the stacking sequence along the growth direction from ABC to AB. To characterize the amount of WZ lattice, we used the fact that for x-ray diffraction some Bragg reflections are equivalent, i.e. occur at the same position in reciprocal space for both lattices, while others exist only in the WZ crystal structure. From the comparison of the integral intensities of several reflections with the theoretical values, and considering all experimental factors such as the change of illuminated area for different Bragg angles, we can derive the wurtzite concentration in a wire ensemble as sketched in Fig. 3.

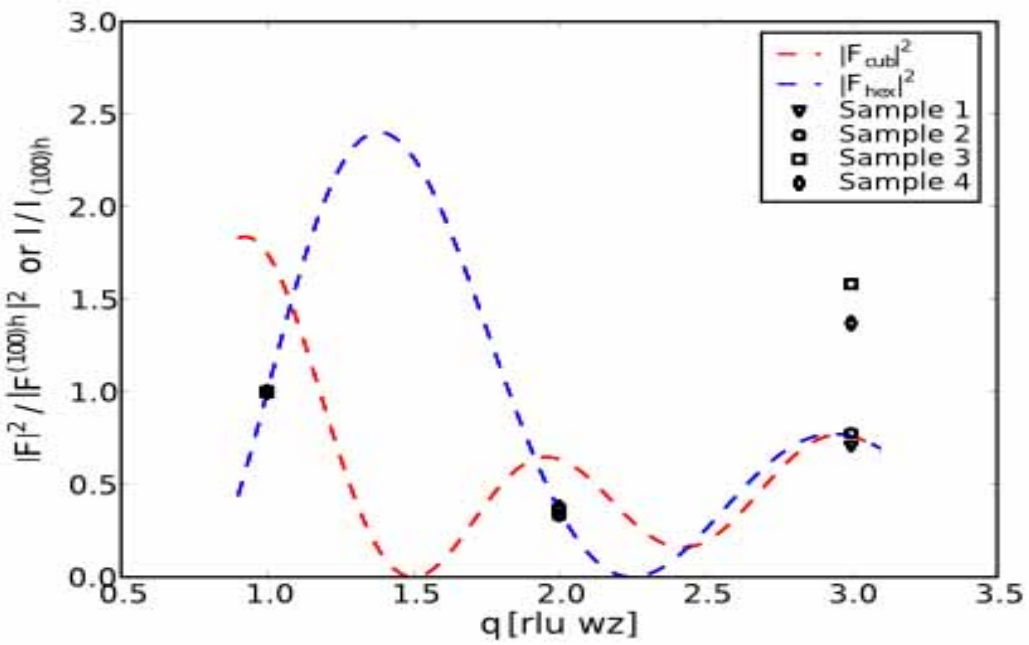

Fig. 3: Normalized intensities of (10-1.0), (20-2.0), and (30-3.0) WZ reflections. The lines between the peaks are continuous interpolations of the structure factor. (30-3.0) of WZ is equivalent to (22-4) of ZB, hence the additional intensity at the Bragg peak is due to the ZB part of the nanowires.

Single Wire Characterization

Since in the WZ/ZB ratio determination for a large nanowire ensemble illuminated by the x-ray beam it cannot be decided whether each wire contains ZB and WZ segments, or some wires are purely ZB while other grow purely in the WZ lattice, we used focused x-rays to illuminate only few nanowires with a focused, partly coherent beam. Measurements were performed at beamline ID01 at the ESRF, Grenoble [3]. The measurements shown in Fig. 4 exhibit a speckle pattern in the intensity distribution, due to the interference of the scattering amplitudes of individual WZ segments. From that the nanowire properties are inferred:

- Three almost isolated peaks are observed at the (30-3.0) reflection, where wurtzite and zinc-blende components are not distinguished, and a “large” structure (the whole nanowire) scatters.

- Broad features are observed at the (10-1.0) reflection, where only wurtzite parts scatter, indicating that the individual scattering objects are small.

To verify this result the intensity distribution was simulated using a model consisting of three basically zinc-blende nanowires, each with randomly distributed, on average 6 nm long wurtzite segments. From the simulation this segment-like wurtzite distribution along the wires can be proven, and the average wurtzite content and segment length determined.

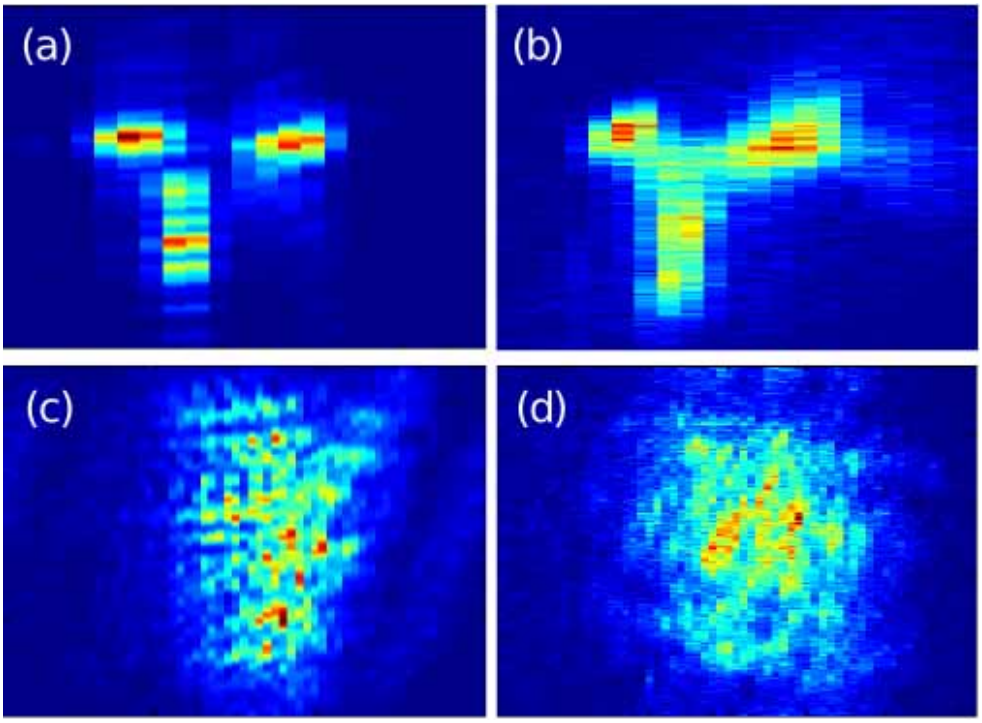

Fig. 6: (a) simulation, (b) measurement of the (30-3.0) peak; (c) simulation, (d) measurement of the (10-1.0) peak of three InAs nanowires

Acknowledgements

This work was supported by the EC (project SANDiE #500101), the FWF Vienna (SFB IR-On#2507). We acknowledge the staff at beamlines ID01 and ID10B (ESRF Grenoble) for assistance with the experiments.

References

[1] B. Mandl, J. Stangl, T. Martensson, A. Mikkelsen, J. Eriksson, L. S. Karisson, G. Bauer, L. Samuelson, and W. Seifert, Nano Letters **6**, 1817 (2006).

[2] T. Martensson, J. B. Wagner, E. Hilner, A. Mikkelsen, C. Thelander, J. Stangl, B. J. Ohlsson, A. Gustafsson, E. Lundgren, L. Samuelson, et al., Advanced Materials **19**, 1801 (2007).

[3] V. Chamard, J. Stangl, S. Labat, B. Mandl, R. T. Lechner, and T. H. Metzger, J. Appl. Cryst. **41**, 272 (2008).

Low Dimensional Nanostructures Grown by Molecular Beam Epitaxy

P. Klang, H. Detz, A.M. Andrews, B. Basnar, W. Schrenk, A. Lugstein, and G. Strasser

Center for Micro- and Nanostructures, Vienna University of Technology, Institute for Solid-State Electronics, Vienna University of Technology, Floragasse 7, Vienna, Austria

Introduction

Self-assembled semiconductor quantum dots (0-D system) have attracted researchers for more than 20 years, because of their unique electronic and optoelectronic properties based on reduced dimensionality. In the last several years, 1-D nanowires have entered the field of nanoscale devices. We present the growth and characterization of these low dimensional structures grown by a solid-source molecular beam epitaxy (MBE) system.

Quantum Dots

For the 0-D structures, we focus on the growth of high quality InAs quantum dots (QDs) in an $Al_xGa_{1-x}As$ matrix for prospective incorporation into intersubband devices like MIR detectors, THz detectors and quantum cascade lasers (QCLs). The growth temperature, growth rate and deposited InAs layer thickness are key parameters to control QD energy levels. For QCLs based on the $Al_xGa_{1-x}As$/GaAs material system, we need the QD ground state energy above GaAs conduction band edge and a narrow size distribution of the QDs.

Growth Parameters

To decouple the density and size of the QDs we use a low InAs growth rate, below 0.01 µm/h. At this low growth rate, the density depends mainly on the growth temperature, and the size of the QDs is controlled by the deposited InAs thickness. The Al content of the growth surface also influences the QD properties. For a higher Al concentration the QD density is increased while the QDs size is reduced. QDs grown on $Al_xGa_{1-x}As$ surfaces also have a greater inhomogeneous size distribution. The sample surface morphologies were analyzed by atomic force microscopy, where we obtained QD density, QD height and its standard deviation, and an estimate of the volume of InAs incorporated into the QDs and the remaining InAs volume in the wetting layer.

Calibrating InAs Growth Rate

The InAs deposition rate was calibrated by high-resolution x-ray diffraction (XRD) measurements of a strained $In_xGa_{1-x}As$/GaAs superlattice (see Fig. 1). The thickness

and therefore the growth rate of the GaAs and InAs can be independently determined using this technique.

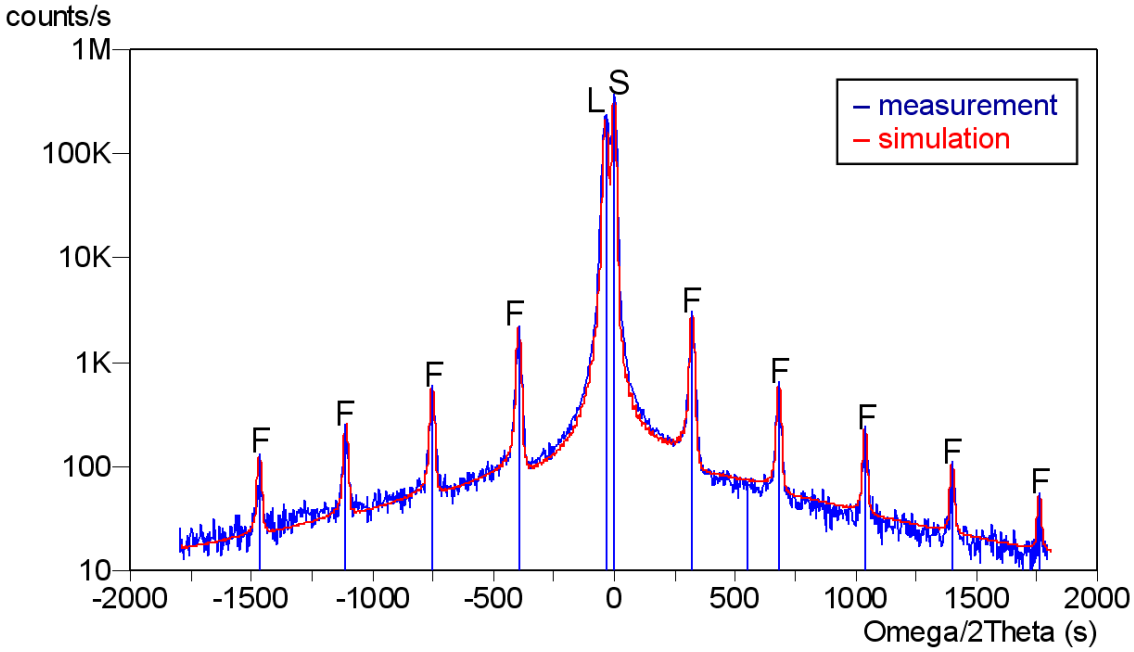

Fig. 1: Measured (blue) and simulated (red) rocking curve around the 004 diffraction for $In_xGa_{1-x}As/GaAs$ superlattice. The layer peak (L) is shifted to left from the substrate (S) GaAs peak, fringe peaks (F) are equidistantly spaced.

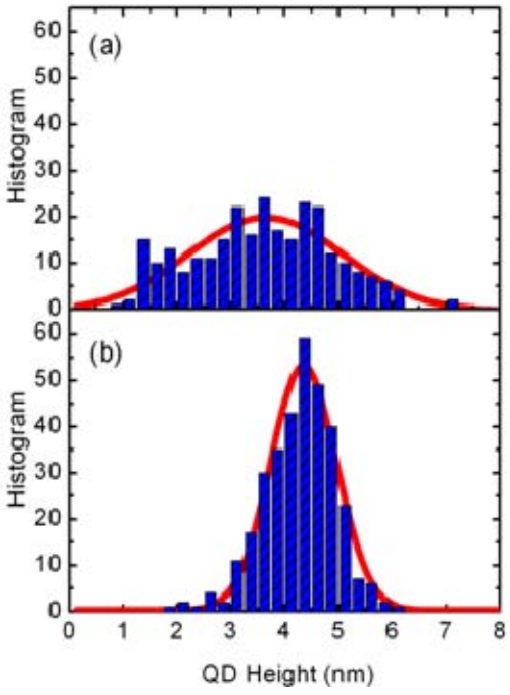

Fig. 2: QD size distribution for (a) standard and (b) new recipe with lowering the As_4 flux during the QDs growth. The standard deviation of the QDs height was reduced more than three times.

Improving Size Distribution

Lowering the As_4 flux during the QDs growth was found to dramatically improve the QD size distribution. For QDs grown on a 45% $Al_xGa_{1-x}As$ surface the standard deviation of the QDs height was reduced from 2.1 nm to 0.6 nm (Fig. 2).

III-V Self-Assembled One-Dimensional Nanowires

We study the MBE growth of III-V self-assembled one-dimensional nanowires on Si nanowires originally grown by low-pressure chemical vapor deposition. To understand the growth mechanism, GaAs growth rates were varied from 0.1–0.55 μm/h and various V/III ratios were used to deposit equivalent layer thicknesses ranging from 40 – 200 nm. Additionally, we investigated MBE growth of GaAs nanowires on different Si substrates with Au catalysts and with various pre-growth surface treatments using buffered HF. The samples were analyzed by scanning electron microscopy (SEM), photoluminescence measurements, high-resolution transmission electron microscopy (TEM) and XRD analysis.

XRD Spectra

There are both powder diffraction peaks and the monocrystalline peaks in the reciprocal space map of NWs measured by high-resolution x-ray diffraction. There are peaks from the monocrystalline Si substrate and also from the epitaxial Si NWs, and polycrystalline peaks from both zinc-blende and wurtzite GaAs, the Au catalyst, and the AuGa alloy (Fig. 3). There was no observed peak for the expected AuSi alloy at the tip of the Si NWs.

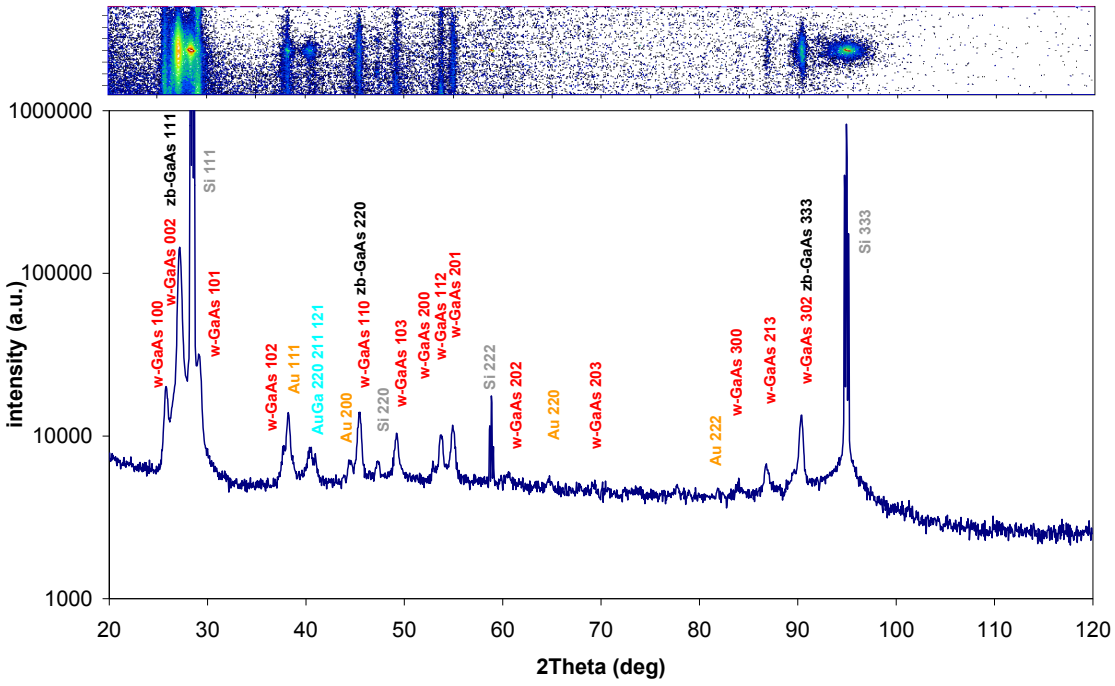

Fig. 3: XRD reciprocal space map and spectra measured on the tree-like structures of GaAs NWs on Si NWs.

SEM Results

Using SEM we can see GaAs nanowhiskers forming structures with a 6-fold symmetry on the Si NW. The length of the Si nanowire trunks are 2 µm. The diameter of the Si trunk is determined by the 80 nm diameter of the Au catalyst. The length of the nanowhiskers (100 nm – 5 µm) depends on the amount of deposited GaAs. GaAs nanowhiskers can be found at any position along the side of the Si-NW trunk (see Fig. 4).

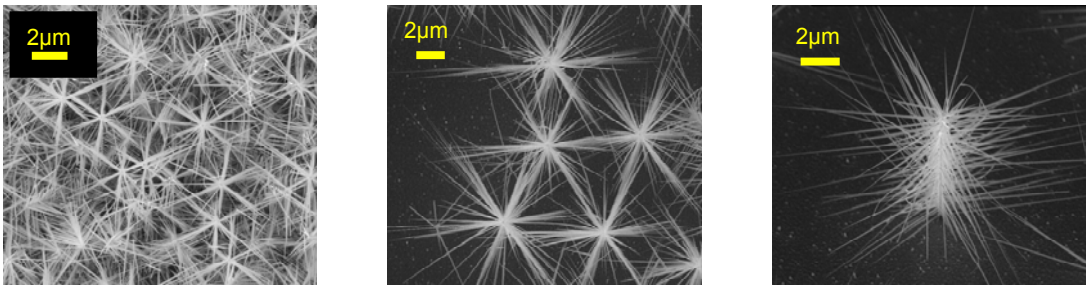

Fig. 4: SEM images of the GaAs nanowhiskers grown on Si NW trunks forming 6-fold tree-like structure.

GaAs NWs on Si Substrates

For a better understanding of crystal properties of the GaAs nanowhiskers, the growth of the GaAs nanowires on planar Si wafer with various pre-growth surface treatments was investigated. We observed high density oriented GaAs nanowires on Si (112) substrates which were exposed to HF after the deposition of the Au catalyst layer. From the SEM analysis of the cleaved edge these nanowires appear tilted under an angle of 19.5° from the substrate normal. This tilt corresponds to the angle between [112] and [111] direction. High-resolution TEM analysis confirmed that the GaAs [0001] nanowires were grown in the wurtzite crystal structure along the Si [111] direction.

Acknowledgements

We acknowledge partial support by the following projects and agencies next to GMe: IRON, MNA, PLATON, and SANDIE.

References

[1] A. Lugstein, A.M. Andrews, M. Steinmair, Y. Hyun, E. Bertagnolli, M. Weil, P. Ponratz, M. Schramböck, T. Roch, G. Strasser, *Nanotechnology*, **18**, (2007)

[2] H. Detz, P. Klang, A.M. Andrews, A. Lustein, M. Steinmair, Y.J. Hyun, E. Bertagnolli, W. Schrenk, G. Strasser, *Journal of Crystal Growth*, **311**, (2009)

Recent Improvements on InAlN/GaN MOS-HEMTs

G. Pozzovivo, J. Kuzmik, S. Abermann, C. Ostermaier, J.-F. Carlin, M. Gonschorek, E. Feltin, J. Liday, N. Grandjean, E. Bertagnolli, G. Strasser, and D. Pogany

Institute for Solid State Electronics, TU Wien, Floragasse 7, A-1040 Vienna, Austria

We present the technology and the performance of InAlN/GaN MOS-HEMTs with gate insulation and surface passivation by using ZrO_2 and HfO_2. 10-nm thick high-k dielectrics were deposited by MOCVD and by ALD before the ohmic contacts which were annealed at only 600 ºC. The passivation and the insulation of 2 µm gate-length MOS-HEMTs led to a gate leakage current reduction by four orders of magnitude and a 2,5x increase of the pulsed source drain current if compared to Schottky barrier (SB)-HEMTs when the high-k is deposited by MOCVD. Moreover, clear current collapse suppression is observed also when the ZrO_2 is deposited by ALD.

Introduction

Gallium Nitride (GaN) has become the superior material for high power devices in microwave applications due to its large bandgap, the high saturation velocity, the high thermal conductivity, and its high mobility in 2-dimensional electron gas (2DEG). This 2DEG is based on the strong ionic bonding of the GaN crystal structure causing large spontaneous and piezoelectric polarization fields at interfaces [1] as used in conventional AlGaN/GaN high mobility electron transistors (HEMTs). However, the stress at the interfaces limits the device performance. Heterostructure devices based on InAlN/GaN [2] have already shown superior results [3], [4] in comparison to conventional AlGaN/GaN HEMTs, due to their higher spontaneous polarization and the possibility of lattice-matched growth of InAlN on GaN at an indium composition of around 18%. Therefore, higher power operation and thermal stability are expected from such devices. However, RF dispersion defined as decreasing output power at large signal gate modulation is still an important issue to be solved. Preview results on AlGaN/GaN devices have shown that surface-related traps are causing transients that prevent the gate from opening after channel depletion [5], [6].

In this report we present our current improvements on InAlN/AlN/GaN MOS-HEMT devices with ZrO_2 or HfO_2 for gate insulation and surface passivation. Metal-Organic Vapor Deposition (MOCVD) and Atomic Layer Deposition (ALD) techniques have been used for the ZrO_2 deposition.

Experimental

The lattice-matched heterostructure was grown by MOCVD on a sapphire substrate. The 1.1 nm thick AlN interlayer was inserted in the conventional structure to increase the mobility in the 2DEG. The dielectric deposition was directly done after Ar-based mesa isolation, requiring that post processed steps are done at lower temperatures without dielectric degradation.

It was found that plasma pre-treatment with $SiCl_4$ before metal evaporation could decrease the ohmic resistance to 0.7 Ω/mm after annealing at only 600 °C. Investigating the surface by Auger Electron Spectroscopy (AES) showed that the total concentration of carbon impurities was reduced only after pre-treatment and for lower temperatures. For the rapid thermal annealing RTA at 600 °C without the RIE pretreatment the ohmic contact resistance R_C was shown to have an unacceptable value of 12 Ωmm. On the other hand $SiCl_4$-based plasma pretreatment led to a contact resistance R_C value as low as 1 Ωmm.

Consequently plasma pretreatment and RTA at 600 °C for 2 minutes was used for the MOS HEMT processing. The final gate processing was done by 2 μm wide Ni/Au contacts (Fig. 1).

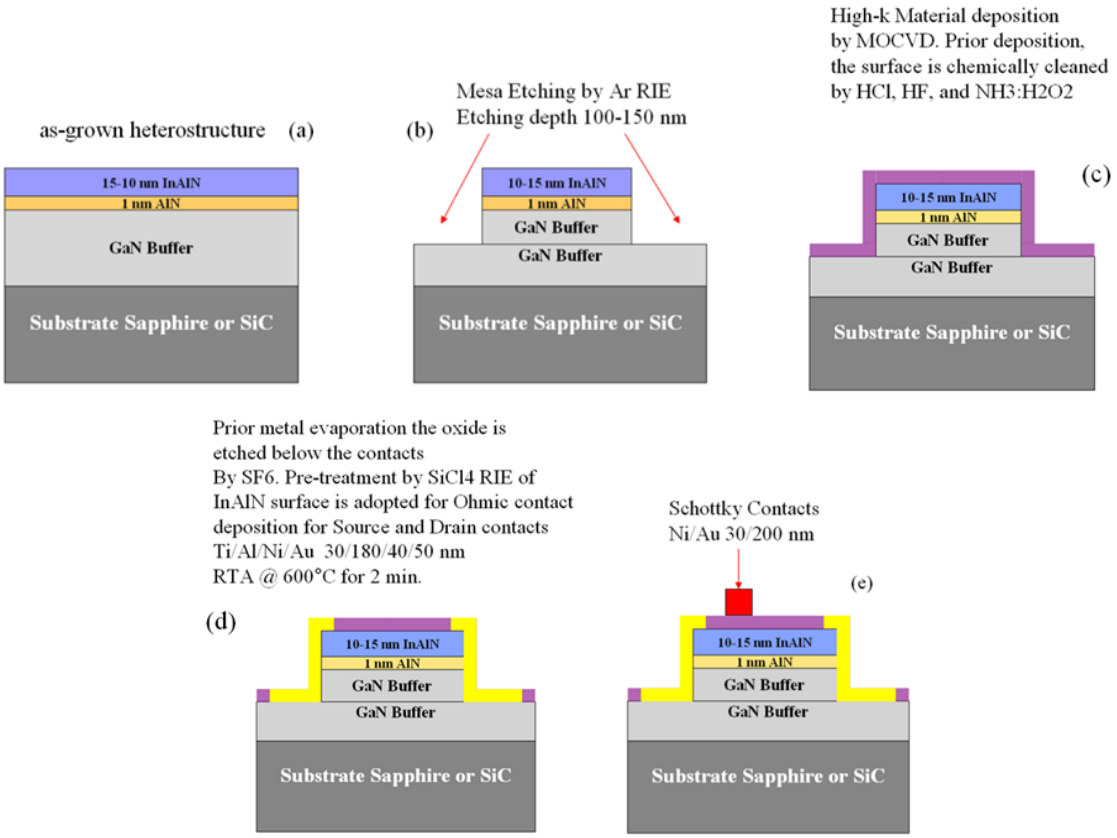

Fig. 1: Schematic illustration: technological steps for the fabrication of the MOS-HEMT structure. The oxide is deposited after the mesa fabrication and before the ohmic contacts metallization.

Figure 2 shows the gate *I*–*V* characteristics in the reverse and forward direction of InAlN/GaN HEMTs, and MOS-HEMTs. A strong reduction of about four orders of magnitude of the leakage current in MOS-HEMTs is observed in comparison to the HEMTs, whereas the ZrO_2-based HEMTs exhibit the same reduction of the leakage current as the HfO_2-based HEMTs. From the MOS *I*–*V* breakdown at about 4 V forward bias in the case of HfO_2 and ZrO_2 (current density $J = 5\times10^3$ mA cm^{-2}) we roughly estimate the oxide field strength to be about 4 MV cm^{-1}.

The output characteristic of the MOS-HEMT was not only improved by higher drain current at increased forward bias, possibly due to the gate insulation, but also showed slightly higher transconductance than the compared SB HEMT. This behavior was ex-

plained by improvement of the intrinsic mobility below the gate, which is more effective in long channel devices [7].

For the current collapse investigation we pulse the HEMT gate contact from the "off-state" level of –10 V to a chosen gate-source voltage V_{GS} value while the constant drain-source voltage V_{DS} is applied on the drain.

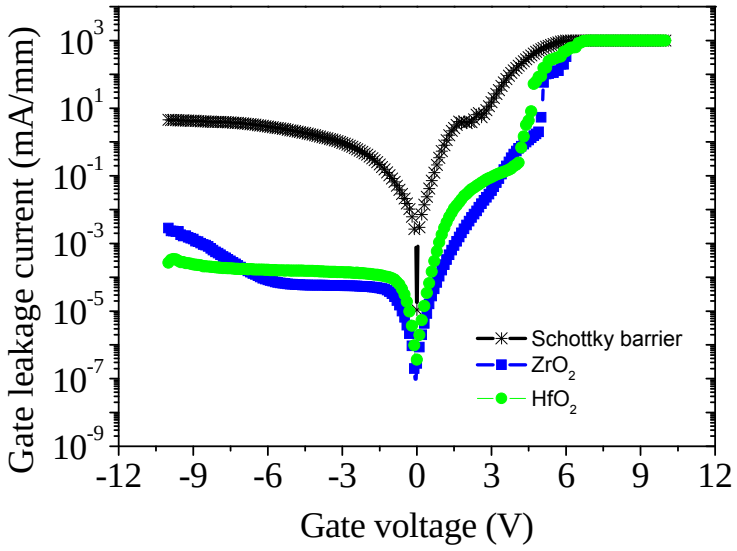

Fig. 2: *I-V* characteristics of the gate leakage current as function of the gate voltage of HfO_2 (ZrO_2)-based MOS-HEMTs (green and blue, respectively) and of a Schottky barrier HEMT (black curve).

Figure 3 (a) (SB-HEMT) confirms a clear lag of the drain transient current I_{DS} behind the *dc* values (for V_{GS} = 0 V) in the linear part of the characteristics.

For V_{GS} = 0 V the transients are shown at two different pulse durations (100 and 200 ns). Higher values obtained for 200 ns indicate gradual surface de-trapping in the SB-HEMTs.

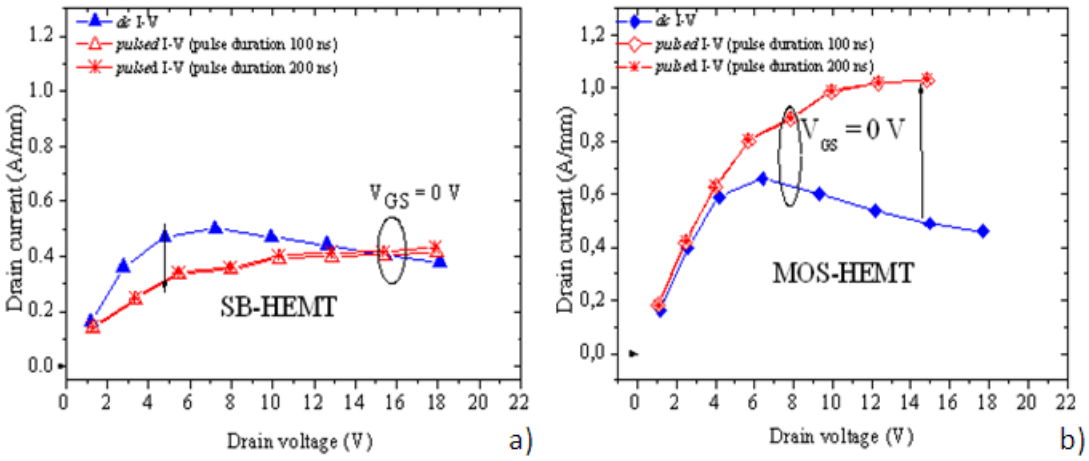

Fig. 3: *dc* and *pulsed* output characteristics of InAlN/GaN SB-HEMTs (a) and of ZrO_2-InAlN/GaN MOS-HEMTs (b). Gate contact is pulsed from –10 V to the set V_{GS}, V_{DS} is sequentially increased, the duration of the pulse is 100 ns and 200 ns

On the other hand, the linear part of the output characteristics of InAlN/GaN MOS HEMTs (see Fig. 3 (b)) show coincidence of the pulsed and the *dc* current characteristics suggesting a stable InAlN surface potential.

For low value of the drain-source voltage V_{DS} in the linear part of the output characteristics we can assume a minimal self-heating effect even in the *dc* mode of operation and thus the coincidence with the pulsed characteristics suggests an effective surface passivation.

In the *dc* mode of operation we observe a drain current enhancement only by about 20% in MOS-HEMTs if compared to SB-HEMTs (Fig. 3 (a) and (b)).

However the pulsed drain current I_{DS} at gate-source voltage V_{GS} = 0 V is up-to 2.5 times higher for MOS HEMTs if compared to SB HEMTs and that clearly demonstrates the superiority of the MOS-HEMT with the surface passivation by dielectrics. We note that the almost similar performance enhancement was observed for both ZrO_2- and HfO_2-based MOS HEMTs.

The low density of trapped electrons and low surface potential at the InAlN/dielectric interface was further validated by measuring the sheet resistance R_{ht} of the SB-HEMTs and MOS HEMTs (in the steady state). For the SB-HEMT we observed an increased value of $R_{sh} \sim 500$ Ω/square (compared with 237 Ω/square measured by Hall method just after the InAlN/GaN growth) probably because of a gradual oxidation and/or contamination of InAlN surface before and during the HEMT processing.

On the other hand an extremely low $R_{sh} \sim 110$ (135) Ω/square has been observed when the InAlN surface is thoroughly etched and subsequently passivated by ZrO_2 (HfO_2), indicating a low surface potential and/or high carrier mobility in the channel.

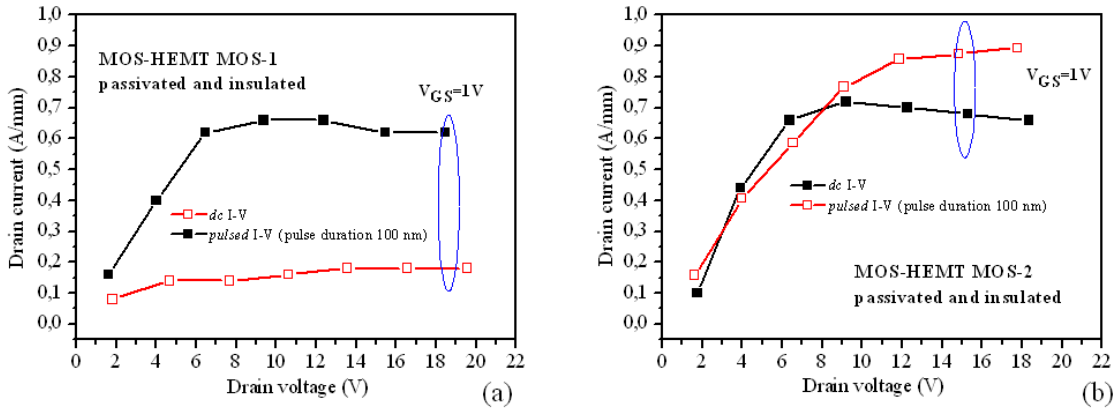

Fig. 4: *dc* and *pulsed* output characteristics of InAlN/GaN MOS-HEMTs. In MOS-1 the ZrO_2 is prepared starting with a single water pulse is passivated while in MOS-2 the ZrO_2 is prepared starting with 10 water pulses prior to the actual ALD process. Gate contact is pulsed from –10 V to the set V_{GS}, V_{DS} is sequentially increased, the duration of the pulse is 100 ns

By using ALD for the ZrO_2 deposition, an aggressive ex-situ chemical surface cleaning in combination with an increased hydroxylation of the InAlN surface by repetitive in-situ H_2O treatment is needful in order to guarantee a good and a stable oxide/semiconductor interface. Since we may believe that the InAlN-surface is not perfectly hydroxide-terminated after the initial chemical ex-situ cleaning procedure we vary the initial phase of the ALD process. By this method we try to improve the hydroxide-termination of the InAlN surface. This may in turn support the initial growth behavior of the ALD process

and improve the oxide/semiconductor interface. The actual ALD process consists of 150 cycles, which results in 10.5 – 11.0 nm thick ZrO_2. Figure 4 (b) shows a clear reduction of the current collapse thanks to an aggressive ex-situ chemical surface cleaning in combination with an increased hydroxylation of the InAlN surface by repetitive in-situ H_2O treatment.

Conclusion

We have shown that the optimized InAlN/GaN MOS-HEMTs exhibit reduced gate leakage currents of about 4 orders of magnitude as compared to SB-HEMTs and a significantly reduced current collapse effect by using high-k dielectrics deposited both by MOCVD and ALD. Moreover an aggressive ex-situ chemical surface cleaning in combination with an increased hydroxylation of the InAlN surface by repetitive in-situ H_2O treatment has to precede gate insulation and surface passivation. This in turn enhances the ALD growth of the ZrO_2 during the first ALD cycles leading to an improved ZrO_2/InAlN interface.

Acknowledgements

We acknowledge the support by the ULTRAGAN European project, the “Gesellschaft für Mikro und Nanoelektronik (GMe), and the MNA network.

References

[1] O. Ambacher et al., J. Appl. Phys., vol. 85, pp. 3222–3233, 1999

[2] J. Kuzmik, IEEE Electron Device Lett., vol. 22, no. 11, pp. 510–512, 2001.

[3] J. Kuzmik et al., IEEE Transactions on Electron Devices, vol. 55, no. 3, 2008

[4] F. Medjdoub et al., 2006 Int.Electron Devices Meeting (IEDM), 2006, Tech. Digest, 927

[5] R. Vetury, IEEE Transactions on Electron Devices, vol.. 48, no. 3, 2001

[6] E. Kohn et al., IEEE Trans. on Microwave Theory and Techniques, vol. 51, no. 2, 2003

[7] G. Pozzovivo et al., Applied Physics Letters, vol. 91 (4), 043509, 2007

Voltage Tunability of Intersubband Lifetimes in SiGe Quantum Well Structures

P. Rauter[1], T. Fromherz[1], G. Bauer[1], N.Q.Vinh[2], G. Mussler[3], D. Grützmacher[3]

[1] Institute for Semiconductor and Solid State Physics, Johannes-Kepler-University Linz, Austria

[2] FOM Institute for Plasma Physics Rijnhuizen, Nieuwegein, Netherlands

[3] Institut für Bio- und Nanosysteme, Forschungszentrum Jülich, Jülich, Germany

Time resolved experiments on biased quantum well structures provide insight into the dependence of intersubband dynamics on the externally applied electric field. The outcome of such experiments is central for understanding the physics of optoelectronic devices like quantum cascade lasers. We report on a direct determination of quantum well intersubband relaxation times for spatially direct and diagonal transitions and the resulting continuous voltage tunability of intersubband relaxation times. The results were obtained by picosecond resolved pump-pump photocurrent experiments on biased SiGe valence band quantum well structures using a free electron laser. By varying the applied voltage, the intersubband hole relaxation times for quantum well structures are increased by a factor of two.

Introduction

Driven by the strong need for Si-based optoelectronic devices for a wide range of applications considerable endeavors have been made to develop a laser in this material system. Silicon is an indirect semiconductor and therefore cannot be used for direct optical transitions over the bandgap. However, the concept of infrared emitters based on quantum cascade heterostructures, which is very successfully applied to III-V material systems, constitutes a promising approach towards a SiGe infrared laser. But while emission of infrared radiation of various wavelengths has been demonstrated for p-type SiGe quantum cascade structures [1] [2], lasing has yet to be achieved. One of the key issues for the achievement of lasing is the build up of population inversion, which is essentially dependent on the excited state's lifetime. As valence band structure calculations for SiGe heterostructures are of high complexity, it is crucial to acquire the key intersubband relaxation times experimentally. In previous works we reported the first direct determination of ultrashort HH2-HH1 relaxation times (550 fs) by pump-pump photocurrent experiments [3] and compared transmission pump-probe experiments with pump-probe PC measurements by determining SiGe LH1-HH1 relaxation times in the ps regime, pointing out the advantage of latter [4].

Experimental

The samples where grown pseudomorphically on a $Si_{0.8}Ge_{0.2}$ [100] pseudosubstrate. One period of the sample structure constitutes of a deep central QW separated symmetrically by Si barriers from two shallow side wells. The central $Si_{0.67}Ge_{0.33}$ QW has a

width of 40 Å and is separated by 10 Å thick barriers from 100 Å wide side wells. 100 Å wide barriers separate the $Si_{0.67}Ge_{0.33}$ side wells from the 300 Å wide $Si_{0.8}Ge_{0.2}$ spacers between the active regions. The central wells and adjacent Si barriers were Boron doped with a concentration of 10^{18} cm^{-3}. The sample consists of 15 periods of the described structures sandwiched between $Si_{0.8}Ge_{0.2}$ contact layers of doping concentration of $4x10^{18}$ cm^{-3}. For vertical PC measurements the samples were processed into mesas of 400 x 400 μm^2 and contacted by Al:Si metallization.

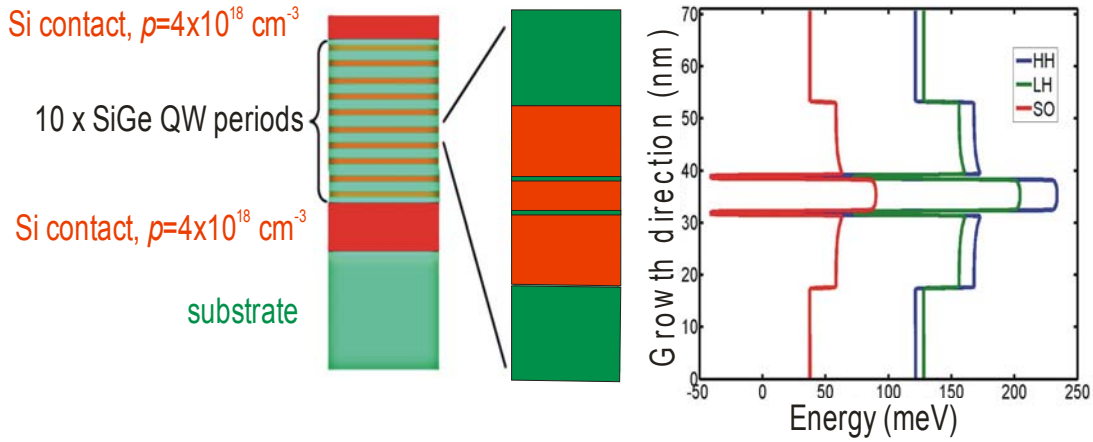

Fig. 1: Sketch of the molecular beam epitaxially grown structure on $Si_{0.8}Ge_{0.2}$ [100] pseudosubstrate. Also shown are the valence band edges as resulting from the growth profile.

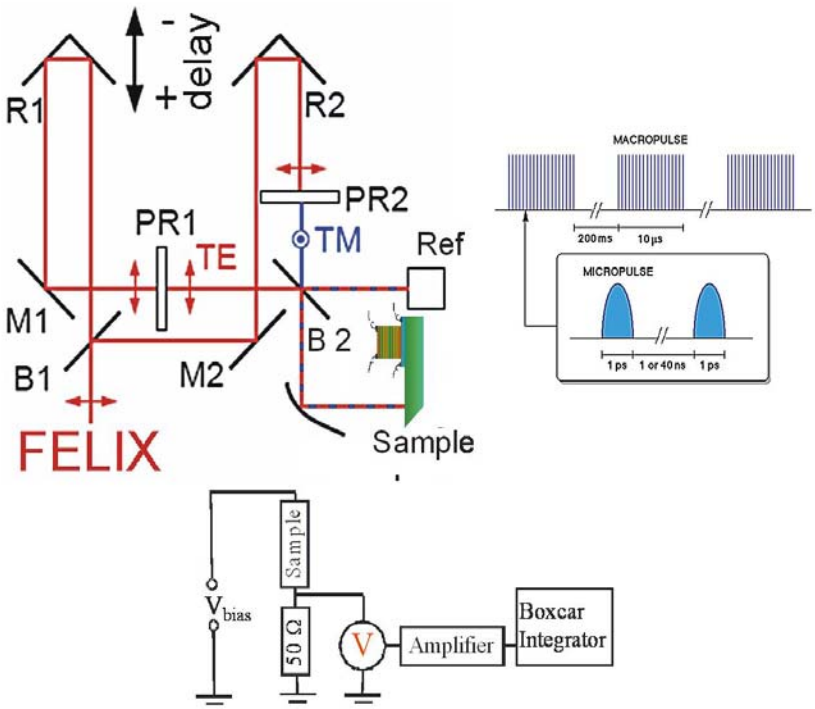

Fig. 2: Pump-pump measurement setup.

In order to determine the LH1-HH1 relaxation time PC pump-pump experiments were performed. The FEL beam was tuned to the respective HH1-LH1 resonance energy of the sample (29.5 meV). It enters the optical setup in TE polarization and is split by a beam splitter (Fig. 2). The polarization of beam 1 is turned by 90°. Beam 2 remains in purely TE polarization and is reflected by a movable mirror allowing to adjust the delay between TE and TM+TE pulse on a femtosecond scale. Before being coupled into the sample waveguide, the beams are made collinear again using a second beam splitter. The integral PC through the variably biased sample originating from the delayed TE and TM+TE micropulses is measured as a function of the delay.

Results

The results of the pump-pump measurements after subtracting backgrounds are presented in Fig. 3 for a series of voltages applied to the sample contacts. The curves show an asymmetry with respect to the sign of the delay, which is due to the polarization dependence of the transition involved. They further exhibit a systematic dependence of the PC decay behavior on the applied bias. The PC signal decays significantly slower with increasing voltage. The reason for the relaxation time tuning can be found in the sample's band structure.

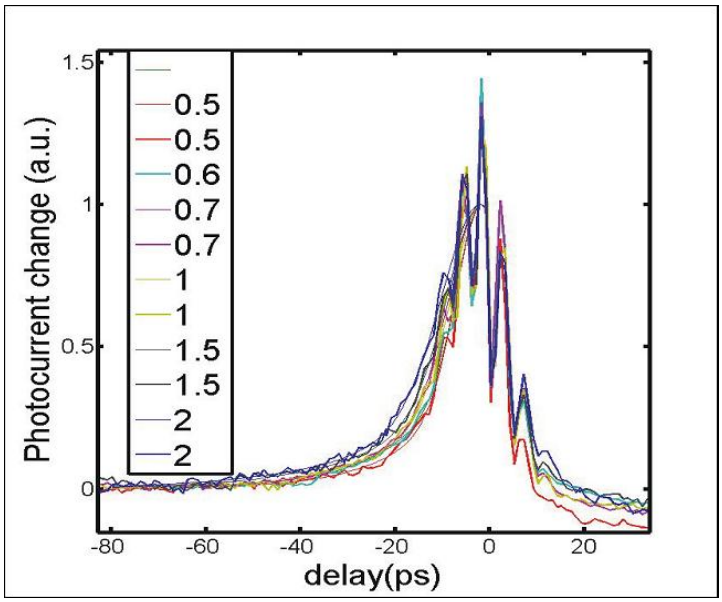

Fig. 3: Change in the decay of the additional photocurrent with the applied bias. The relaxation time increases by a factor of two when changing the bias between 0.5 and 2 V.

As the applied bias is increased, the investigated optical transition changes from a spatially direct into a spatially indirect transition, decreasing wavefunction overlap of the transition's ground and excited states and thus increasing the relaxation time.

Conclusion

In conclusion, we report a directly observed bias-tuning of intersubband relaxation times in QW structures. By continuously changing a spatially direct into an indirect transition, we were able to increase the monitored intersubband relaxation time by a factor of two.

References

[1] G. Dehlinger et al., Science **270**, 2277 (2000).

[2] S.A. Lynch et al., Material Science and Engineering B **89**, 10 (2002).

[3] P. Rauter et al., Applied Physics Letters **89**, 211111 (2006).

[4] P. Rauter et al., New Journal of Physics **9**, 128 (2007).

Si/Ge Growth on Stripe Patterned Si (001) Studied by Scanning Tunneling Microscopy

B. Sanduijav, D. Matei, G. Chen, and G. Springholz

Institut für Halbleiter- und Festkörperphysik, Universität Linz, A-4040 Linz, Austria

Si and Ge growth on stripe patterned Si(001) substrates is studied using scanning tunneling microscopy. During Si buffer growth, the stripe morphology rapidly evolves to multifaceted "U" or "V" shaped forms due to transitions between different low energy {11n} side facets. Depending of the side wall geometry, subsequent Ge islands nucleate either on the side walls or in the center of stripes. Thus, the control of pattern topography is crucial for effective control of the nucleation sites.

Introduction

Self-organized Stranski-Krastanow island growth on pre-patterned substrates has attracted tremendous interest because it provides a route for controlled positioning of quantum dots in nano-electronic devices as well as for realization of quantum dot arrays [1] – [4]. Site controlled growth requires a tight control over the pattern morphology and growth conditions [1] – [5] and to obtain quantum dots with excellent electronic properties, sufficiently thick buffer layers have to be deposited to remove the defects induced by the patterning process [2], [3]. Therefore, a detailed understanding of the surface evolution and dot nucleation is crucial for control of the self-organization process. Here, in situ scanning tunneling microscopy is employed to study Si/Ge growth on a stripe-patterned Si (001) substrate. It is shown that a characteristic morphological transition from multifaceted "U" to "V" shaped grooves occurs during buffer growth and that a well-defined alignment of Ge islands only occurs for "V" shaped grooves.

Experimental

The investigations were carried out in a multi-chamber Si/Ge molecular beam epitaxy and scanning tunneling microscopy (STM) system. Stripe patterned Si (001) substrates were prepared by electron beam lithography and CF_4 reactive ion etching. The stripes with an etch depth of 35 nm and 350 nm period were aligned along the [110] surface direction. By varying the exposure dose, different groove widths from w = 70 to 280 nm were obtained, corresponding to pattern filling factors (ratio of w to the 350 nm period) of δ = 0.2 to 0.8. After cleaning and HF dipping for oxide removal, the samples were introduced into the vacuum system and shortly annealed at 740 °C. Si and Ge growth were performed at substrate temperatures between 450 to 600 °C and growth rates of ~3 and ~1 Å/min. STM images were recorded after different stages of growth after rapid cooling to room temperature to preserve the epitaxial surface structure.

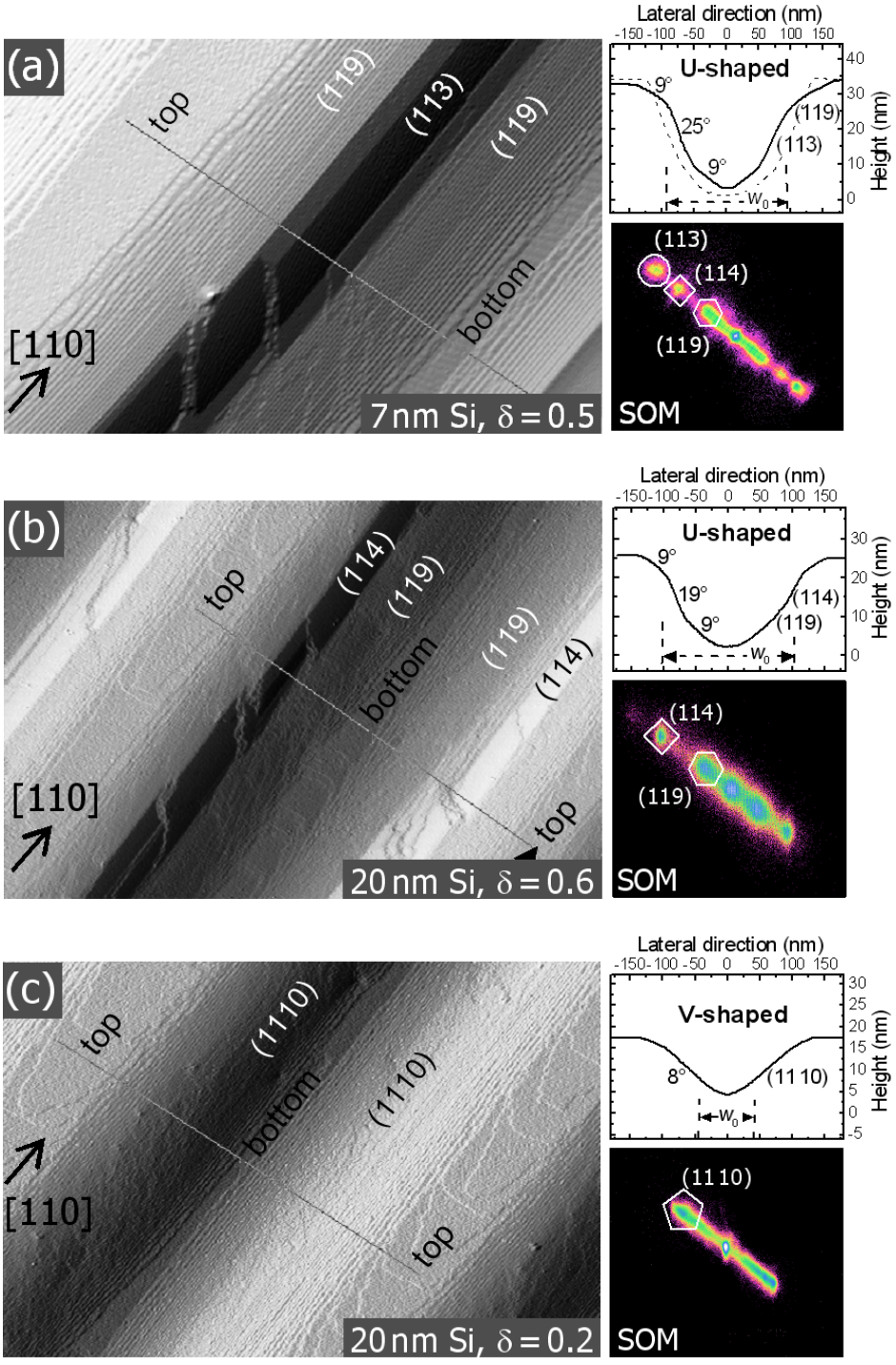

Fig. 1: STM images of stripe patterned Si (001) substrates after 520°C Si buffer growth: (a) “U” shaped grooves with {113} facets formed after 7 nm Si growth on stripes with δ = 0.5, (b) “U” shaped grooves with {114} facets after 20 nm Si on stripes with δ = 0.6, (c) “V” shaped grooves with {11 10} facets after 20 nm Si on stripes with δ = 0.2. STM image lateral size: (a) 0.35 µm, (b) and (c) 0.5 µm. The line profiles across the stripes as well as surface orientation density maps (SOM) of the STM images are shown on the right hand side and in (a) the stripe cross-section after low temperature buffer growth is additionally shown as dashed line.

Results

Usual Si buffer growth at temperatures above 600 °C leads to a complete pattern erasure within deposition of a few nm Si. Therefore, a two-step buffer growth was employed. First, 35 nm Si was deposited at a temperature of 450 °C to bury the residual carbon impurities on the surface. This leads to a rounding of the bottom of the grooves but their depth remains nearly unchanged. This was followed by Si growth at 520 °C for smoothening of the surface and further elimination of process defects. During the second buffer growth step the surface morphology rapidly evolves due to enhanced surface diffusion. This is illustrated by the sequence of STM images displayed in Fig. 1.

Already after 7 nm Si growth, the stripes assume a well defined multi facetted “U” shape as demonstrated by the STM image of Fig. 1 (a) for stripes with δ = 0.5. From the cross-sectional profile analysis shown on the right hand side, there exist two short sidewall segments with ~9° inclination at the top and bottom of the grooves, and a steeper middle segment with ~25° inclination. The middle segment is therefore composed of {113} and {114} facets which pass over to {119} segments with small inclination towards the top and the bottom of the grooves. The corresponding surface orientation map (SOM) of the STM image exhibits two bright spots for the {113} and {114} facet orientations and a broader maximum at {119}. The high resolution STM image of the sidewall depicted in Fig. 2 (b), reveals that the {119} areas are composed of D_B type double steps, indicating that this surface part resembles a vicinal (001) surface. On the contrary, the steeper side wall areas appear completely flat and step free in the STM image and display the characteristic atomic structure of {113} and {114} Si surfaces [6].

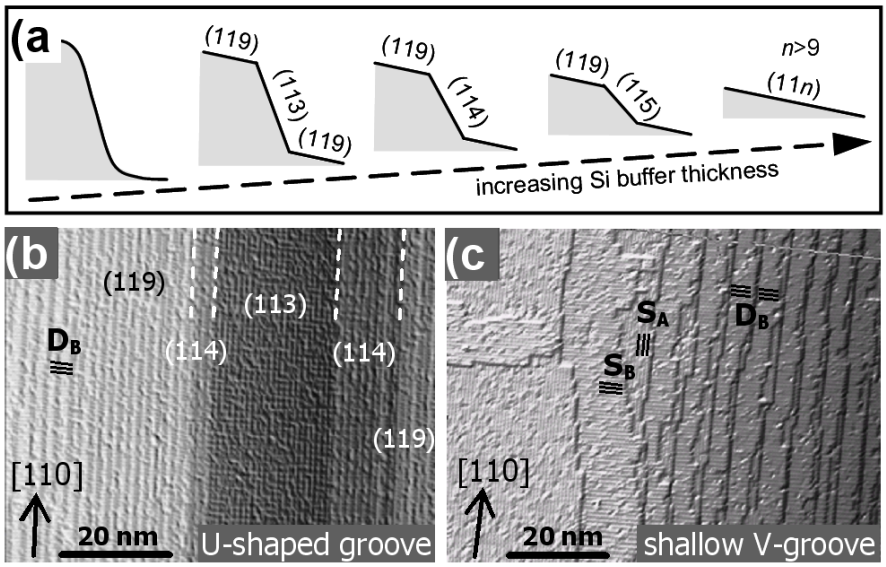

Fig. 2: (a) Schematic illustration of the evolution of the side wall profiles (b) High resolution STM image of the side wall of the multifaceted “U” groove shown in Fig. 1 (a) after 7 nm Si buffer growth. (c) STM image of a shallow “V” groove with about 4° side wall inclination. The triple lines indicate the directions of the Si dimer rows.

Continuing the Si buffer growth leads to a rapid shrinking of the steep middle sidewall segments and an expansion of the shallower {119} segments. This is demonstrated by the STM image of Fig. 1 (b) obtained after 20 nm Si deposition. The line profile analysis identifies inclinations of ~9° at the upper and lower part of the groove and of ~19° for the middle segment. Thus, the {113} area has been completely transformed to a {114}

facet. Accordingly, only the {114} and {119} spots appear in the SOM. With further increasing Si thickness the {114} segment continuously shrinks and is replaced by a shorter {115} segment, which eventually also disappears such that only one extended ~9° side wall surface remains. This is illustrated schematically in Fig. 2 (a). The speed of this transformation strongly depends on the width and depth of the grooves and is much faster for patterns with small filling factor δ. This is demonstrated in Fig. 1 (c) for a pattern with δ = 0.2 where already after 20 nm Si the surface been completely transformed to "V" shaped stripes with ~8° side walls as is indicated by the profile of Fig. 1 (c). The corresponding SOM shows a strongly elongated maximum around the {11 10} surface orientation. Thus, the side wall does not correspond to a unique stable facet orientation [6]. During further Si deposition the sidewall angle rapidly shrinks and a planar surface is reformed after about 30 nm. The high resolution STM image of such a shallow "V" groove is shown in Figs. 2 (c), where the average side wall inclination is only around 4°. As indicated, the side wall exhibits a D_B stepped terrace structure formed by merging of S_A and S_B single steps in the transition region at the edges of the grooves. This indicates that this region represents a vicinal surface.

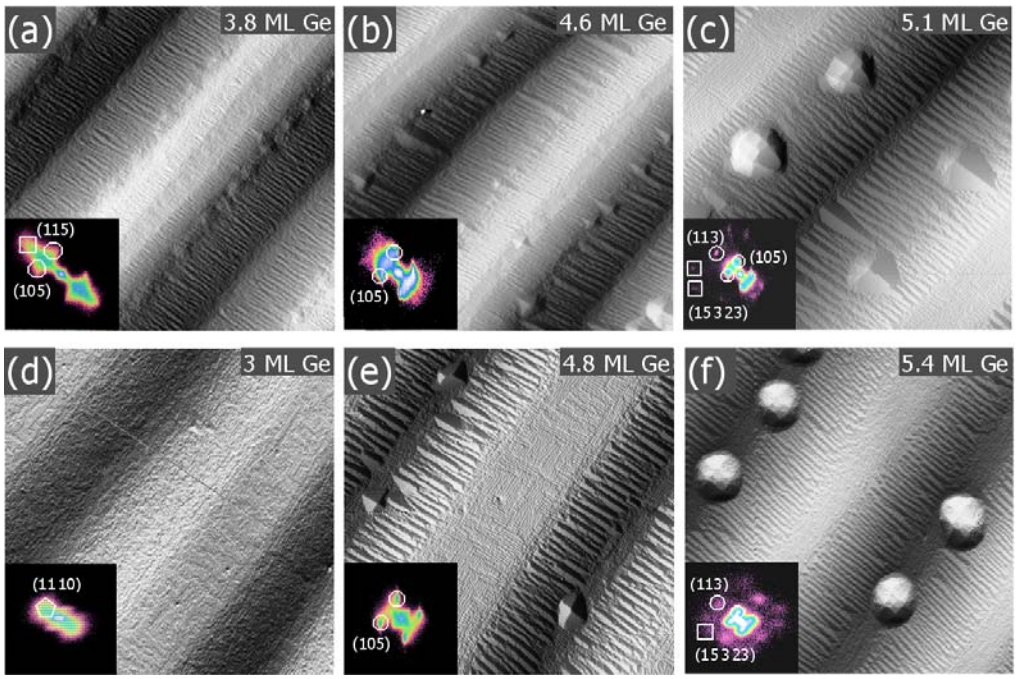

Fig. 3: STM images of Ge growth at 620 °C on stripe pattern Si surfaces after buffer growth. Top (a) – (c): Growth on "U" grooves with {119} and {115} sidewall facets and Ge thickness increasing from 3.8, 4.6 to 5.1 ML, respectively. Bottom (d) – (f): Growth on "V" grooves with {11 10} side faces and Ge thickness from 3, 4.8 to 5.4 ML, respectively. Ge first induces a {105} sidewall ripple structure and at higher coverages, pyramids and domes with characteristic {113} and {15 3 23} facets are formed, as indicated by the surface orientation maps (SOMs) depicted as insets. Image size: 0.5 × 0.5 μm^2.

To study the influence of the Si surface geometry on subsequent Ge island nucleation, Ge was deposited at 600 °C after buffer growth. The results for "U" shaped stripes with {115} sidewall segments are shown in Fig. 3 (a) – (c). During wetting layer growth, a distinct side wall ripple structure develops perpendicular to the stripes (Fig. 3 (a) after 3.8 ML Ge). The appearance of {105} spots in the SOM, indicates that these ripples consists of alternating {105} Ge micro-facets. On the steeper {115} side wall areas, no ripples but mounds with a few Å height are created, representing precursors for Ge

island formation. Adding 0.8 ML Ge induces their transformation to {105} facetted Ge pyramids as demonstrated by the STM image of Fig. 3 (b). Further Ge deposition leads to an increasing island size and transformation to dome islands with characteristic {113} and {15 3 23} facets as shown by Fig. 3 (c) after 5.1 ML Ge. Evidently, all Ge islands in the "U" grooves are located in middle of the side walls.

STM images of Ge growth on "V" shaped stripes are presented in Fig. 3 (d) – (f). At 3 ML coverage (Fig. 3 (d)), the Ge wetting layer shows the typical (2×8) surface reconstruction of {001} Ge surfaces. After 4.8 ML Ge deposition (Fig. 3 (e)) pronounced side wall ripples appear again, but now they extend all the way from the top to the bottom of the grooves. At 4.8ML also the first {105} Ge pyramids appear, but they nucleate at the bottom of the grooves. This is because downward diffusion of Ge adatoms is not hindered by a steeper facet barrier. Upon further Ge deposition, the pyramids are transformed again to dome islands as shown by Fig. 3 (f). Accordingly, the characteristic {113} and {15 3 23} facet spots appear in the SOM. Nucleation of Ge dots at particular surface sites is driven by the variation of the chemical potential across the pattern structure due to variation of the local surface curvature. This generates an increased adatom flux towards the concave surface areas. For "V" grooves, the only concave area is at the bottom of the grooves, where material accumulation leads to a preferential Ge island formation. For "U" shaped grooves, concave surface parts also exist at the intersections between the {119} and steeper {114} or {115} side wall facets. Ge adatoms diffusing downward into the grooves accumulate at these intersections and thus, island formation sets in at the middle of the side walls.

Conclusion

In conclusion, Si growth on patterned substrate templates produces a characteristic morphology evolution from multifaceted "U" to "V" shaped geometries due to transitions between distinct side wall facets. Depending on the resulting surface morphology, subsequent Ge islands form either on the side walls or the center of the grooves. Multilayer Si/Ge growth drastically improves the control of the pattern morphology. Therefore, site-controlled Ge island nucleation is readily achieved by this growth sequence.

Acknowledgements

This work was supported by the Austrian Science Funds (SFB IR-ON).

References

[1] G. Chen, H. Lichtenberger, G. Bauer, W. Jantsch, F. Schäffler, Phys. Rev. B, Vol. 74, 2006, pp. 035302-1-8.

[2] Z. Zhong, A. Halilovic, M. Mühlberger, F. Schäffler, and G. Bauer, J. Appl. Phys., Vol. 93, 2003, pp. 6258-6264.

[3] C. Dais, H.H. Solak, E. Müller, D. Gruetzmacher, Appl.Phys.Lett., Vol. 92, 2008, pp. 143102-1-3.

[4] G. Chen, G. Vastola, H. Lichtenberger, D. Pachinger, G. Bauer, W. Jantsch, F. Schäffler, and Leo Miglio, Appl. Phys. Lett., Vol. 92, 2008, pp. 113106-1-3.

[5] B. Sanduijav, D. Matei, G. Chen, F. Schäffler, G. Bauer and G. Springholz, Thin Solid Films, Vol. 517, 2008, pp. 293-296.

[6] A.A. Baski, S.C. Erwin, L. J. Whitman, Surf. Sci., Vol. 392, 1997, pp. 69-85.

Novel Materials (Posters)

Atomic Layer Deposition of High-*k* Gate Dielectrics on Germanium and Silicon Substrates

O. Bethge, S. Abermann, Ch. Henkel, and E. Bertagnolli

Institute for Solid State Electronics, Vienna University of Technology, Floragasse 7, 1040 Vienna, Austria

$Al_2O_3/ZrO_2/Al_2O_3$ high-k dielectric stacks are grown on Germanium and Silicon substrates by Atomic Layer Deposition at temperatures of 110 °C, 150 °C, 200 °C and 300 °C from trimethylaluminum (TMA) and tetrakis-(dimethylamino)zirconium (Zr(NEt2)4) precursors with water. The stacks are investigated and compared in terms of deposition temperature and Ge-substrate preparation. As a result, we show that in general the deposition of the stacks at lower temperatures (150 °C) leads to lower leakage currents in the range of several orders of magnitude. The deposition on GeOx-free Ge-substrates, obtained by HBr-etching, yields much higher breakdown voltage of the high-k oxide.

Introduction

Aside from silicon, germanium is an attractive material in downscaled Complementary-Metal-Oxide-Semiconductor (CMOS) devices due to its high electron mobility and its low dopant activation temperatures. The fact that Ge does not offer a stable natural oxide is no more a disadvantage over Si. For the extrinsic ultra thin dielectric layers envisaged for future CMOS-devices, Atomic Layer Deposition (ALD) is the favored deposition process for high-k dielectric materials like hafnium dioxide (HfO_2) or zirconium dioxide (ZrO_2). For the deposition process, alternative semiconductors as well as novel device architectures issues a lowering of the deposition temperature well below 300 °C.

Electrical and structural characterization of ALD triple stacks of $Al_2O_3/ZrO_2/Al_2O_3$ (AZA) on Si grown by a chlorine-based ($ZrCl_4$) chemistry for ZrO_2 deposition at temperatures of 300 °C have already been performed [1]. However, residual chlorine content in the ALD films leads to increased oxide charge concentrations and interface states, if deposited at lower temperatures [2]. Only a chlorine-free metal amide precursor seems to be favorable for a low temperature deposition with satisfactory electrical characteristics.

In this work AZA triple layers grown by ALD on Si and Ge from a chlorine-free precursor system at deposition temperatures ranging from 110 °C to 150 °C are compared with dielectrics deposited at the usual higher temperatures ranging from 200 °C to 300 °C in terms of their applicability in nanoscaled MOS devices. In order to explore the thermodynamical stability of the as-grown oxides, different Ge surface pretreatments and post deposition annealing steps are applied. The morphology is verified by High-Resolution Transmission Electron Microscopy (HR-TEM) analysis. MOS capacitors are used to characterize the electrical performance referred with film stack structure and morphology.

Experimental

Sample Preparation

Silicon

As substrates, boron (p)-doped, (100)-oriented Si wafers with 1 – 5 Ohm·cm sheet resistance have been used. After ultrasonically enhanced Piranha- and RCA-type cleaning, all substrates were exposed for 10 min to a 2% HF solution to remove the native SiO_2 layer from the substrates. Immediately prior to deposition, a short H_2O-rinse or a variable exposure of 10 min has been applied.

Germanium

Here, antimony-doped (100)-oriented n-Ge wafers with 6 – 10 Ω·cm sheet resistance have been used. All substrates were exposed for 3 min to one of the following wet chemical treatments to remove the instable native GeO_x:(i) 20-% HCl-solution with cyclic 35%-H_2O_2-rinse (HCl <—> H_2O_2), (ii) 20-% HCl solution with incorporated 1% H_2O_2 solution (HCl+H_2O_2) and (iii) 48-% HBr solution (HBr). A short H_2O rinse and a subsequent N_2 blow has been applied to remove chemical residuals.

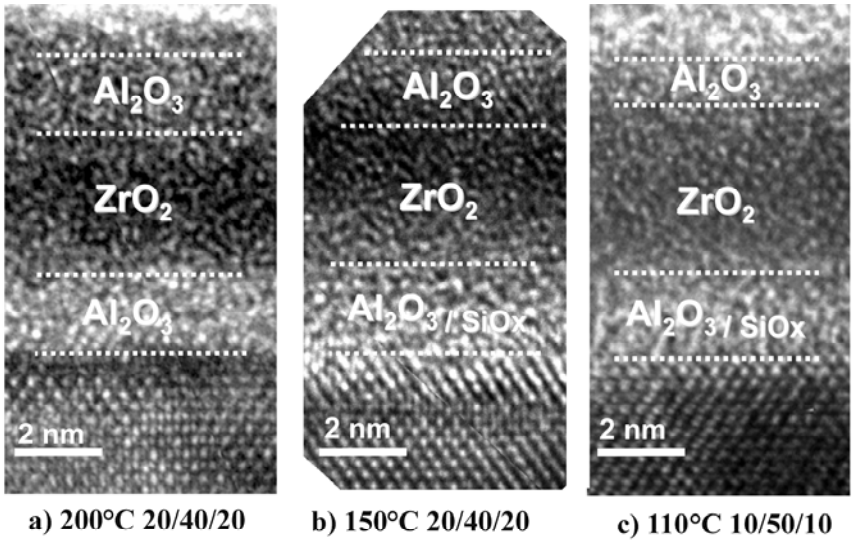

Fig. 1: HR-TEM of $Al_2O_3/ZrO_2/Al_2O_3$ stacks deposited at (a) 200 °C, (b) 150 °C and (c) 110 °C on Si substrates.

The high-*k* oxide stacks have been grown in a Savannah 100 ALD reactor from Cambridge NanoTech Inc. The substrate temperatures during ALD growth have been set to 110 °C, 150 °C, 200 °C, and 300 °C, respectively. In order to achieve a reliable layer by layer growth, we applied purging times from 3 seconds to 90 seconds. Three different dielectric stacks have been deposited: (i) 70 ALD-growth-cycles of pure ZrO_2 (0/70/0), (ii) stacks composed of a 10 ALD-growth-cycles Al_2O_3 at the bottom and at the top of a 50 ALD-growth-cycles ZrO_2, respectively (10/50/10), and (iii) stacks corresponding to 20 ALD-growth-cycles Al_2O_3 at the bottom and at the top of 40 ALD-growth-cycles ZrO_2, respectively (20/40/20). After oxide deposition, a Post Deposition Annealing (PDA) in inert, reductive, and oxidative atmospheres, respectively, has been applied for a duration of 5 min at 400 °C. In order to complete the MOS capacitors, circular aluminum (Al) electrodes with diameters of 100 µm have been fabricated by sputter deposition and patterned by photolithography involving a lift-off technique.

Measurements

Morphology

In Fig. 1 a morphological analysis from HR-TEM of 10/50/10 stacks deposited on Si at 110 °C and 20/40/20 stacks deposited at 150 °C and 200 °C with similar total thickness of about 6.9 nm to 7.0 nm is shown. The images indicate contiguous amorphous ZrO_2 and Al_2O_3 films even at deposition temperature of 200°C. Samples deposited at 200 °C exhibit no interfacial SiO_2 whereas samples deposited at 150 °C and at 110 °C most likely exhibit SiO_2 or mixtures of Al_2O_3 and SiO_2 at the oxide/semiconductor interface. These oxides may have two origins, (i) a partly fragmentary, not fully contiguous Al_2O_3 bottom layer, and/or (ii) much longer purge times during the ALD growth at lower deposition temperatures strongly increase the process time, and therefore enlarge possible diffusion times for oxygen, which may lead to a stronger SiO_2 growth at the Si/oxide interface. In both cases, oxygen may be able to diffuse through the ZrO_2 matrix during the oxide growth process and to oxidize the Si surface. In the case of the 10 ALD-growth-cycle process, the Al_2O_3 layer is most likely not contiguous due to the previously mentioned inhibited growth, and therefore the oxygen is able to diffuse easier to the dielectric/ Si interface to form an interfacial SiO_2 layer.

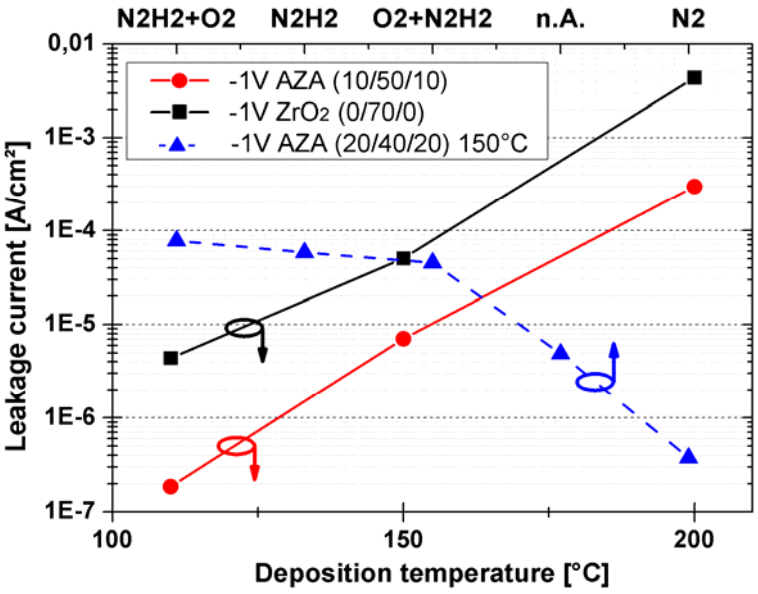

Fig. 2: Impact of the deposition temperature and PDA on the leakage current of the various high-*k* MOS-capacitors at -1 V gate bias.

Electrical characterization

As an important result on Si substrates, it can be seen that lowering of the deposition temperature from 200 °C to 110 °C yields lower gate leakage currents of about 3 orders of magnitude, as shown in Fig. 2. As mentioned above, this is most likely to longer purge times at lower deposition temperatures, which may lead to a stronger SiO_2 growth at the Si/oxide interface.

The *I-V* measurements of AZA stacks on Ge substrates, shown in Fig. 3, indicate that lowering of the deposition temperature from 300 °C to 150 °C yields lower gate leakage currents of about one order of magnitude. Here, similar explanations are presumably: Much longer purge times during the ALD growth at lower deposition temperatures enlarge possible diffusion times for oxygen, which may lead to a stronger GeO_x regrowth at the Ge interface. All dielectric stacks exhibit a breakdown in the range of 3 to

4 gate bias, except of the samples with HBr pre-treatment, where the breakdown occurs not until bias has been driven to ~6 V. We believe that this remarkable result is correlated with a complete removal of the sub-oxide through HBr, as reported. In the same way, it has been reported for Si that a thin interfacial SiO_2 layer is the origin of breakdown of high-k dielectric stacks [3].

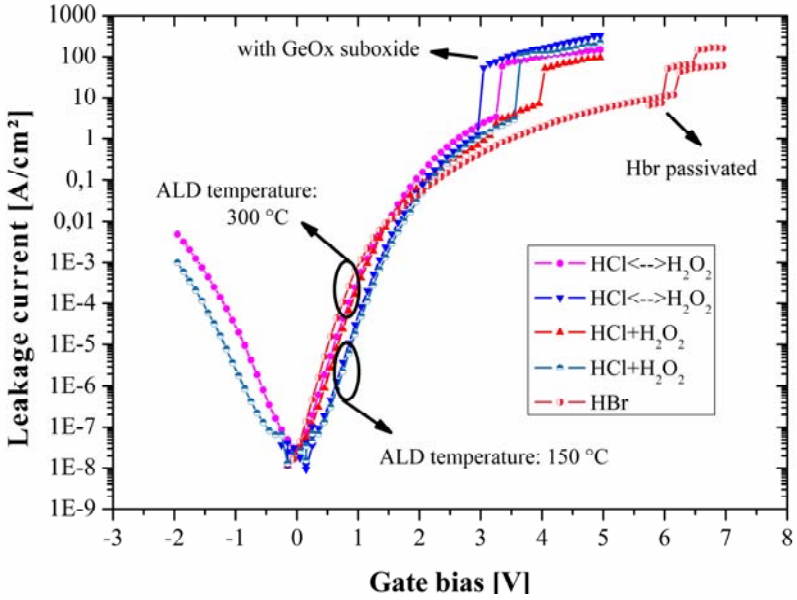

Fig. 3: Leakage current measurements of the Al/oxide/n-Ge MOS capacitors with AZA 20/40/20 dielectric stack as oxide, deposited at 150 °C and 300 °C.

Conclusion

In conclusion, dielectric stacks grown at low temperatures are suitable to design high performance MOS devices, exhibiting well-behaved electrical characteristics and low gate leakage currents. Therefore, the “low temperature” process appears applicable for lift-off processes involving resist polymers, or for the deposition on alloy heterostructures, making it potentially attractive for scaled CMOS device applications.

Acknowledgements

This work is funded by the Austrian Science Fund (FWF), project No. P19787-N14. The Gesellschaft für Mikro- und Nanoelektronik, GMe, as well as the Zentrum für Mikro- und Nanostrukturen, ZMNS, are gratefully acknowledged for support.

References

[1] D. Kil et al., Symposium on VLSI Technology Digest of Technical Papers, (2006)

[2] W. Chen, Q. Sun, M. Xu, S. Ding, D. Zhang, L. Wang, J. Phys. Chem. C 111, 6495 (2007)

[3] M. Rafik, G. Ribes, D. Roy, G. Ghibaudo, 15th Workshop on Dielectrics in Microelectronics, Berlin (2008)

Process Integration of Pt-Metal-Gate High-k ALD Dielectrics on sSOI

C. Henkel[1], S. Abermann[1], O. Bethge[1], M. Reiche[2], and E. Bertagnolli[1]

[1] Institute for Solid-State Electronics, TU-Vienna, Floragasse 7, A-1040 Vienna, Austria

[2] Max-Planck-Institute for Microstructure Physics, Weinberg 2, D-06120 Halle, Germany

In this presentation we focus on the electrical properties of high-k-dielectric gate stacks, namely aluminum-oxide (Al_2O_3) on strained silicon-on-insulator (sSOI). In order to get both, stoichiometry as well as atomic scale smoothness, these oxides are deposited by Atomic Layer Deposition. These properties are compared to those obtained for MOSFET devices on bulk silicon.

Introduction

The superior properties of the silicon-silicon dioxide combination are the key to the success and the opportunity to continuously shrink the device geometry of modern transistors. However, to keep the inversion channel in a quasi-2-dimensional arrangement, the silicon dioxide has to be shrunk accordingly to the lateral dimensions, thus modern devices approach the tunnel limit for the gate dielectric, giving rise to the onset of high gate leakage currents. Silicon dioxide has therefore to be replaced by proper high-κ-dielectrics, enabling larger tunnel barriers at approximately the same drive current. In industrial CMOS, such high-κ-dielectrics were introduced at and beyond the 45 nm technology node, often in combination with metal gates.

Further improvement of the device performance is addressed by the replacement of bulk silicon as substrate material. By this step, mobility constrains of the bulk silicon substrates should be overcome. Promising candidates for this purpose are high-carrier-mobility substrates like SiGe or Ge. Another approach is the use of engineered substrates like strained silicon, offering the opportunity of an enhancement of both, the electron and the hole mobility [1].

In this presentation we focus on the electrical properties of high-κ-dielectric gate stacks, namely aluminum-oxide (Al_2O_3) on strained silicon-on-insulator (sSOI). In order to get both, stoichiometry as well as atomic scale smoothness, this oxide is deposited by Atomic Layer Deposition (ALD) [2]. The electrical properties are compared to those obtained for MOSFET devices on bulk silicon. Suitable process temperature ranges for annealing post-treatments are determined.

Experimental

Process Flow and Sample Preparation

The process flow is schematically depicted in Fig. 1 (left). The high-κ dielectric Al_2O_3 is deposited at temperatures of 200 °C to sSOI substrates. A scheme of the final device is shown in Fig. 1 (right). The influence of different process parameters to the properties

of Bulk-Si MOSFETs is investigated. Different Post-Deposition and Post Metallization Annealing Treatments are applied.

In a final step the optimized process flow is applied to strained Silicon-on-Insulator substrates. Schottky-Barrier-MOSFET devices with PtSi source/drain regions were processed with the same deposition and pretreatment parameters (Fig. 4).

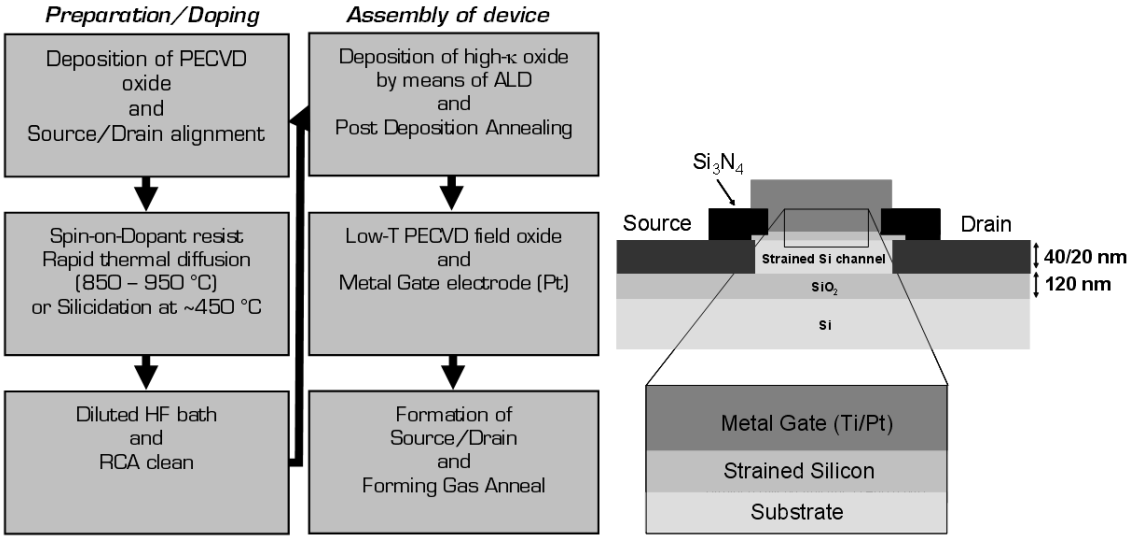

Fig. 1: Process Flow for MOSFET devices (left) and a schematic of the final MOSFET (right).

Results

Current-Voltage Characteristics

Optimized process conditions were found for the deposition of Al_2O_3. A Post Metallization Anneal was applied in Forming Gas atmosphere at 500 °C for 30 minutes. Figure 2 shows the resulting Transfer and Output characteristics of the Bulk-Si MOSFET.

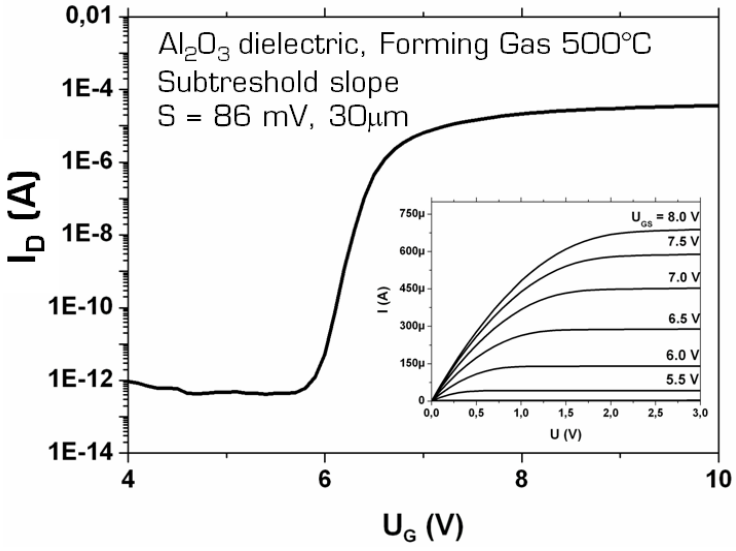

Fig. 2: Transfer-/Output characteristic for bulk-Si.

Applying the same process parameters to SB-MOSFETs on sSOI results in well behaved current characteristics. These can be seen in Fig. 3.

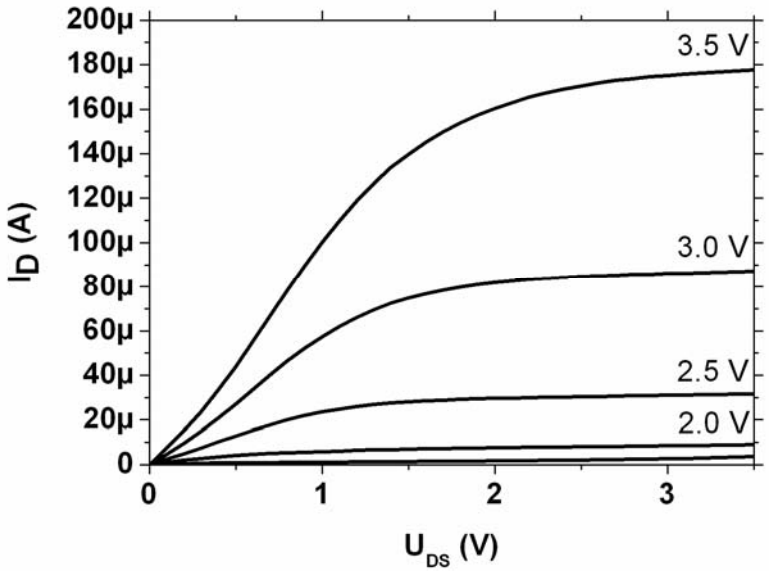

Fig. 3: Output characteristic for sSOI substrates. The strained silicon film thickness is 40 nm.

Split-CV Measurements for Mobility Determination

By means of split-capacitance-voltage measurements [3] the mobility of processed devices can be investigated. Thus, interface quality of the Si-channel to gate oxide is determined. An optimized deposition process was studied for bulk-Si and Al_2O_3 with the optimized process conditions. Here peak mobilities of 175 cm^2/Vs can be obtained (Fig. 4). These results can be compared to the results obtained for sSOI substrates with mobilities of 53 cm^2/Vs.

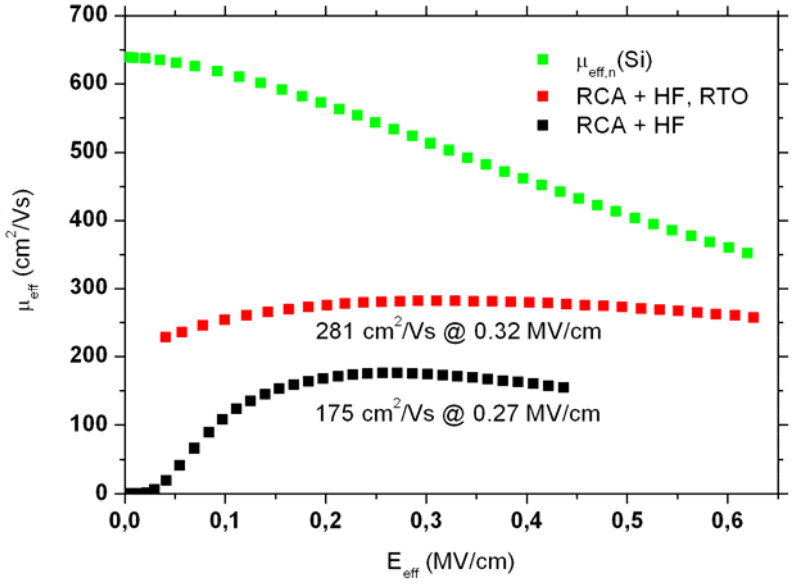

Fig. 4: Effective mobilities of n-MOSFET and the universal field mobility for n-Si/SiO_2.

Conclusion

Properties of metal gate high-κ dielectrics on strained Silicon-on-Insulator substrates (sSOI) have been investigated. A successful integration scheme of high-κ dielectrics on sSOI substrate is presented using metallic source-drain contacts processed by silicidation. The results are compared to those of bulk silicon substrates where MOSFET characteristics have been evaluated. Further studies will address the optimization of the deposition process in combination with the formation of the source/drain contacts on sSOI substrates.

Acknowledgements

This work is funded by the Austrian Science Fund (FWF), project No. P19787-N14. The Gesellschaft für Mikro- und Nanoelektronik, GMe, as well as the Zentrum für Mikro- und Nanostrukturen, ZMNS, are gratefully acknowledged for support.

References

[1] M. Reiche et al., *ECS Transactions*, **6**, 339 (2007).

[2] M. Leskelä and M. Ritala, *Angew. Chem. Int. Ed*., **42**, 1924 (2003).

[3] D. Schroder, Semiconductor and Device Characterization, Wiley & Sons (1998).

Para-Sexiphenyl Based OLED Devices Grown on Light Sensitive Polymer Substrates

C. Simbrunner[1], G. Hernandez-Sosa[1], T. Höfler[2], G.Trimmel[2], W. Kern[2,3], and H. Sitter[1]

[1] Institute for Semiconductors and Solid State Physics, Johannes Kepler University Linz, Altenbergerstrasse 69, 4040 Linz, Austria

[2] Institute for Chemistry and Technology of Organic Materials, Graz University of Technology, Stremayrgasse 16, A-8010 Graz

[3] Departement of Chemistry of Polymeric Materials, Franz-Josef-Straße 18, A-8700 Leoben

We report on OLEDs based on Para-sexiphenyl (PSP), which has been deposited by Hot Wall Epitaxy (HWE) on Polynorbornene, a photosensitive polymer. The used substrates have been pre-patterned by UV illumination leading to a changed surface polarity and consequently to an induced change of morphology and crystalline properties of the grown PHP. In particular we report on the optical properties of the devices which can be tuned by UV illumination of the polynorborene substrates.

Introduction

Morphology and crystalline order is determining for improving the electrical and optical properties of organic films. Therefore it is of great importance to study the growth kinetics of organic materials on substrate surfaces with well controlled properties. Para-sexiphenyl (PSP) ($C_{36}H_{26}$), a six units oligomer of para-phenylene, is a promising candidate as an electro active layer in organic LED displays due to its blue luminescence with high quantum yield [1], [2]. Moreover, it is classified as a wide gap organic semiconductor with an electronic band gap of 3.1 eV with photoluminescence in the blue visible range and polarized absorption and emission when provided in well ordered films [3].

The Hot-wall epitaxy (HWE) technique offers the advantage that it works close to thermodynamic equilibrium. Therefore it allows organic molecules to find the most suitable arrangement into the crystal lattice and as a consequence, highly ordered organic thin films can be obtained [3], [4]. Organic thin films grown by HWE have shown outstanding optical and electrical properties [5], [6]. Extensive morphological and structural characterization has been already performed on HWE grown PSP films deposited on various substrates such as KCl and muscovite mica, showing that the nature of the substrate and the growth conditions are ruling parameters for the molecular packing of the films [7].

In the presented work, an amorphous polymer poly(diphenyl bicyclo[2.2.1]hept-5-ene-2,3-dicarboxylate) (PPNB) containing photoreactive aryl-ester groups was chosen as substrate. Upon illumination with UV-light of $\lambda < 280$ nm these ester groups isomerize to the corresponding hydroxyketones in the so-called photo-Fries reaction [8], [9]. Recently, we have shown that the photoreaction in PPNB yields up to 21 % hydroxyketones as photoproducts [10]. The UV-induced reaction leads to a large increase of the

refractive index as well as of the surface polarity. This enhanced polarity and the generated new functional groups can be used for selective post-modification reactions [11]. In particular we report on the optical properties of the devices which can be tuned by UV illumination of the polynorborene substrates.

Experimental Methods

Sample Preparation

The procedure to synthesize PPNB is reported by T. Höfler et al [10]. For the substrate preparation a 10 mg/ml solution of PPNB in $CHCl_3$ was prepared and stirred for 12 h. Then the solution was spin cast onto Glass/ITO/PEDOT:PSS-substrates resulting in 80 nm film thickness (see Fig. 1). In order to provide equivalent growth conditions for UV-exposed and non-irradiated surfaces, each substrate was divided in two regions. One half of the substrate was exposed for 20 min to UV light (254 nm) while the other half was protected from UV illumination. The unfiltered light of an ozone-free mercury low pressure UV lamp (Heraeus Noblelight; 254 nm) was used. The illumination-process was done in inert gas atmosphere (nitrogen with a purity >99.95%) in order to avoid unwanted oxidation reactions.

After the illumination process the substrates were transferred via a load lock to a HWE growth chamber working at a dynamic vacuum of $9x10^{-6}$ mbar. A 15 min in-situ pre-heating procedure was applied in order to reduce surface contaminations. The substrate temperature during preheating is chosen the same as the growth temperature in order to allow constant thermal conditions during the whole deposition process. The working principles of a HWE system can be found elsewhere [12].

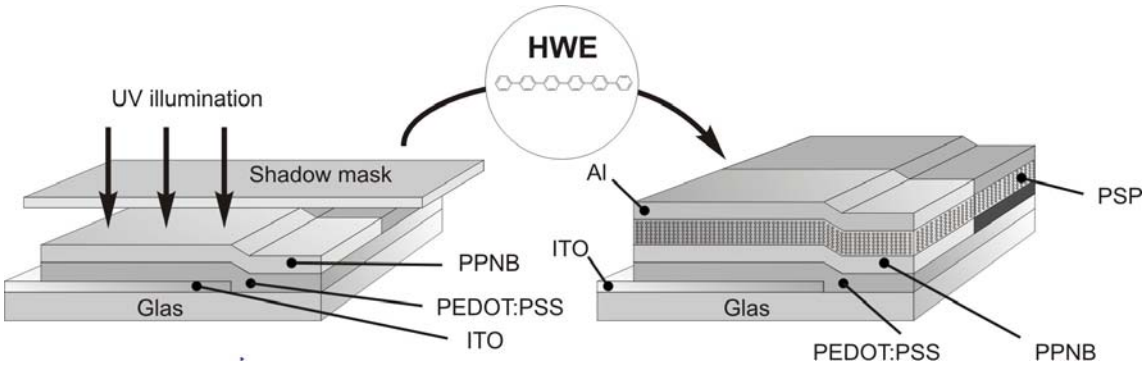

Fig. 1: Schematic of the sample preparation. After UV illumination process the sample is transferred to the HWE system where PSP is evaporated. Finally Al contacts are created by thermal evaporation

After the deposition of PSP on top of the described sample structure Al contacts were deposited by thermal evaporation. Contacts were structured by using a shadow mask providing contact pads on the illuminated, non-illuminated and at the interface in between the two domains.

In order to provide electrical contact to the sample, gold wires were indium-soldered to the contact pads. The whole structure was then mounted on a chip carrier, providing a flexible solution for the next measurement steps.

Measurements

All samples were measured using a Keithley 2400 I-V-Source unit which is synchronized with an Avantes fiber spectrometer. Consequently I-V characteristics of the OLED´s can be acquired parallel to electroluminescence emission spectra. In that way the CIE color-coordinates, the spectral response as a function of applied current and the I-V characteristic can be determined. A detailed analysis of the spectral response is reported elsewhere [13].

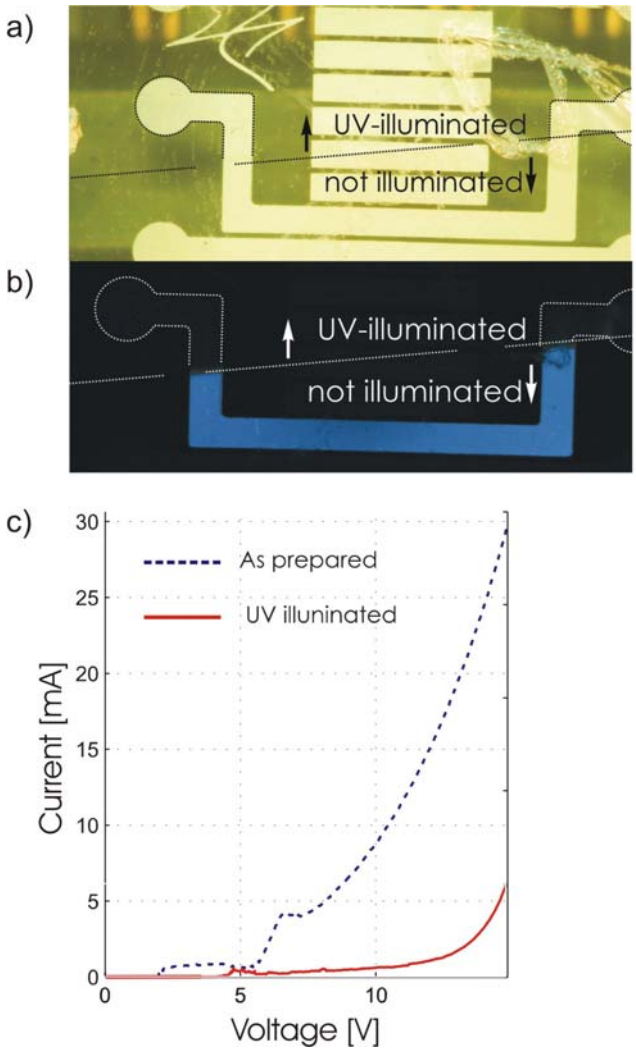

Fig. 2: Optical photograph of a PPNB-PSP-OLED structure showing the device without applied voltage (a) and during operation (b). The line indicates the border between illuminated and non-illuminated substrate regions. In section (c) typical IV curves for both domains are depicted.

In order to provide optical images of the fabricated device an optical microscope equipped with a standard digital camera was used. Typical results are depicted in Fig. 2 showing an OLED device without applied voltage (a) and during operation (b). Striking seems that no obvious structural difference is noticed between illuminated and non-illuminated part of the samples as depicted in Fig. 2 (a). The border line of the two regions is indicated by a black line splitting the tested contact pad in two parts. Nevertheless during operation a huge effect is visible showing a clear blue emission of the not illuminated part, whereas the UV treated region stays dark. A more detailed analysis of

the effect is given by electrical measurements, using two geometrical identical contact pads situated on the illuminated and the non-illuminated part of the sample. Typical results are shown in Fig. 3 (c) indicating a change in conductivity due to the UV-illumination by a factor of 5 – 10.

Conclusion

In conclusion the presented structuring method represents a powerful tool in order to provide structured OLED devices. It was demonstrated that by UV illumination of the substrate the optical properties of a device can be controlled opening new perspectives for OLED pre-structuring processes. Nevertheless more detailed investigations have to be done to explain the presented effect in more detail.

Acknowledgements

This work was supported by the Gesellschaft für Mikroelektronik (GMe) and the Austrian Science Foundation projects NFN-S9702, NFN-S9706 and NFN-S9708.

References

[1] S. Tasch, C. Brandstatter, F. Meghdadi, G. Leising, G. Froyer, L.Athouel, Advanced Materials, Vol. 9,33,1997.

[2] G.Leising, S. Tasch, W. Graupner, Fundamentals of Electroluminescence in Paraphenylene-type Conjugated Polymers and Oligomers, in Handbook of Conducting Polymers, Edited by T. Skothem, R. Elsenbaumer, J. Reynolds, 2nd ed., New York 1997.

[3] A.Y. Andreev, G. Matt, C.J. Brabec, H. Sitter, D.Badt, H. Seyringer, N.S. Sariciftci, Advanced Materials ,Vol. 12 , 629, 2000.

[4] D. Stifter and H. Sitter, Applied Physics Letters, 66, 679, 1995.

[5] Th. B. Singh, N. Marjanovic, G. J. Matt, S. Gunes, N. S. Sariciftci, A. M.Ramil, A. Andreev, H. Sitter, R. Schwodiauer, and S. Bauer, Organic.Electronics. Vol. 6, 105, 2005.

[6] F. Quochi, F. Cordella, R. Orru, J. E. Communal, P. Verzeroli, A. Mura, and G. Bongiovanni A. Andreev, H. Sitter, and N. S. Sariciftci Applied Physics Letters, vol. 84, 4454, 2004.

[7] T. Haber, A. Andreev, A. Thierry, H. Sitter, M. Oehzelt, R. Resel, Journal of Crystal Growth, Vol. 284, 209, 2005.

[8] J.C. Anderson, C.B Reese, Proceedings of the Chemical. Society, 217, 1960.

[9] D. Bellus, Advances in Photochemistry, Vol. 8, 109, 1981.

[10] T. Höfler, T. Griesser, X. Gstrein, G. Trimmel, G. Jakopic, W. Kern, Polymer, Vol. 48, 1930, 2007.

[11] T. Griesser, T. Höfler, S. Temmel, W. Kern, G. Trimmel, Chemistry of Materials, Vol. 19, 3011, 2007

[12] A. Lopez-Otero, Thin Solid Films, Vol. 3, 4, 1978.

[13] C. Simbrunner, G. Hernandez-Sosa, T.Höfler, G.Trimmel, W. Kern, H. Sitter, submitted

Sensors (Posters)

A Sensor Concept for Label-Free Cell Analysis

S. van den Driesche[1], W. Witarski[2], S. Armenta[3], M.J. Vellekoop[1]

[1] Institute of Sensor and Actuator Systems, Vienna University of Technology, Vienna / Austria

[2] Institute of Virology/Slovak Academy of Sciences, Bratislava / Slovakia

[3] Institute of Chemical Technologies and Analytics/ Vienna University of Technology, Vienna / Austria

Based on IR absorbance spectra of healthy and malignant breast [1] and blood cells [2] found in literature we investigated the possibility of disease stage cell discrimination by comparing only a few absorbance peaks. This way no expensive FTIR spectroscope or time consuming expensive staining/labeling steps are required. Absorbance differences between healthy and malignant cells at wavelengths 3.42 and 3.51 µm (corresponding to lipid CH_2-anti-symmetric and CH_2-symmetric stretch respectively), showed a possible disease stage discrimination basis. To test the few wavelengths hypothesis the absorbance spectra of healthy and carcinoma epithelial kidney cell lines were recorded with an FTIR-spectroscope and compared. The results showed a significant difference between the three cell lines which have led to the development and realization of a novel sensor system.

Introduction

Distinguishing healthy from malignant cell types by means of labeling and staining is time consuming and expensive. Also highly trained personnel are necessary to interpret the obtained data. Infrared spectroscopy, IR absorbance due to specific molecular vibrations, is an interesting diagnostic tool without the need of added labels. Instead of recording the whole IR spectra between 2 and 20 µm with a Fourier transform infrared (FTIR) spectroscope a few wavelengths in the lipid absorption region (between 3 and 4 µm) could be sufficient to distinguish healthy from tumor cells. This way, a smaller and cheaper sensor system based on LED light sources, narrow bandpass filters and a room temperature operable photodiode detector could be used for label-free cell analysis. By comparing the IR absorbance spectra of healthy and malignant cells, published in literature, we hypothesized a few wavelength based cell type discrimination concept. The concept is based on the absorbance ratio between lipid CH_2 antisymmetric and symmetric stretch (respectively at 3.42 and 3.51 µm). To test the few wavelength hypothesis and get better understanding how the IR absorbance spectra are recorded and compared we made our own data set of healthy (MDCK) and carcinoma (A-498 and Caki-1) epithelial kidney cell lines.

Experimental

Few Wavelength Concept

The investigated cell lines were all grown under the same conditions in monolayer on IR transparent calcium-fluoride (CaF_2) slides. Just before the absorbance recordings the cells were vacuum dried. In Fig. 1 (a) the averaged absorbance spectra of four

MDCK, A-498 and five Caki-1 sample spots are shown. Due to artifacts such as differences in water concentration and sample thickness, normalization and baseline correction are needed when sample comparison is required. Figure 1 (b) depicts how the ratio (CH_2 symmetric / antisymmetric stretch) can be extracted for sample comparison with baseline correction.

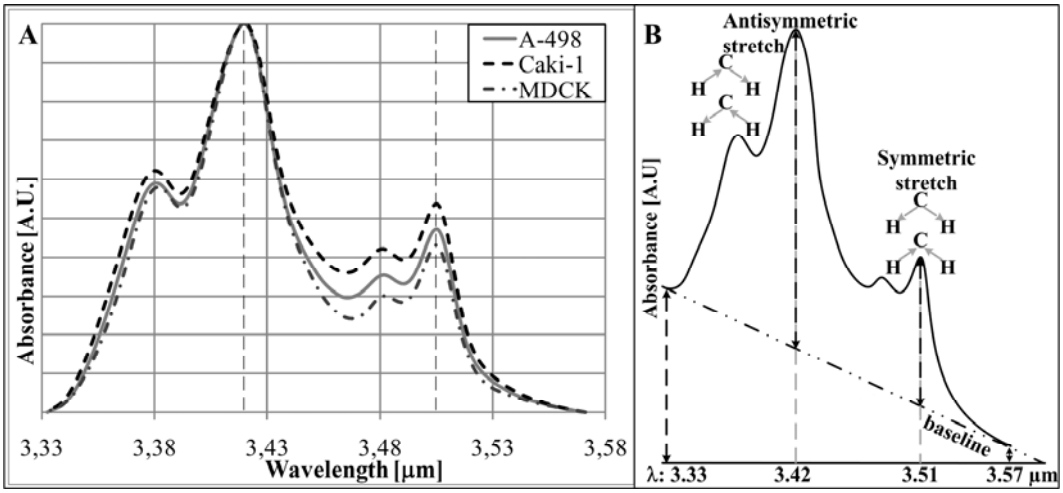

Fig. 1: (a) Normalized and baseline corrected IR Absorbance spectra comparison of epithelial kidney cells MDCK, A-498 and Caki-1 between wavelengths 3.33 and 3.57 µm recorded with a Bruker Equinox 55 spectrometer (240 scans per spectrum, 4 cm^{-1} resolution and 1 mm beam diameter). The absorbance peak at 3.51 µm is increased in the two carcinoma cell lines (10% A-498 and 25% Caki-1) compared to the healthy MDCK cell line. (b) Ratio determination. From each sample the absorbance at 3.33 and 3.57 µm is used for the base line (dashed black arrows) calculating the absorbance ratio 3.51/3.42 µm (dashed black grey arrows).

The measured differences in absorbance ratio (10% and 25% increase compared to MDCK for A-498 and Caki-1 respectively) confirms the hypothesis that cell types can be distinguished by means of the few wavelength concept. The next step is to design a sensor system.

Sensor Concept

To cover the four wavelengths two LEDs are used in combination with two narrow bandpass filters (NBP) each. The transmittance spectra are shown in Fig. 2. Figure 3 (a) shows a sensor concept consisting of two LED IR sources, four NBPs, a beam-splitter to focus both beams at the same spot, and a detector.

Compared to liquid nitrogen cooled detectors used in FTIR spectroscopes, for the 3.3 to 3.6 µm wavelength range there is a room temperature operable photodiode (PD) based detector available. A sensor setup in early development stage is shown in Fig. 3 (b). With this setup absorbance ratio measurements of yeast samples have been made.

First Sensor Measurement

Dried baker's yeast was resuspended in phosphate buffered saline (PBS). A 2 µl sample was pipetted on a CaF_2 slide. Before measuring the absorbance ratio the sample was dried for 2 hours above a heated plate at 50 °C. The IR beams of both LEDs were

focused on a 1.5 mm diameter aperture. The CaF_2 slide was positioned right after this aperture. To determine the absorbance ratio first the 100% transmittance voltages (PD output current converted to a voltage, amplifier) were measured by using an empty CaF_2 slide. The next step was to measure and calculate the % absorbed values of the yeast sample at the four wavelengths (Fig. 4) and subtract the baseline at 3.42 and 3.51 µm.

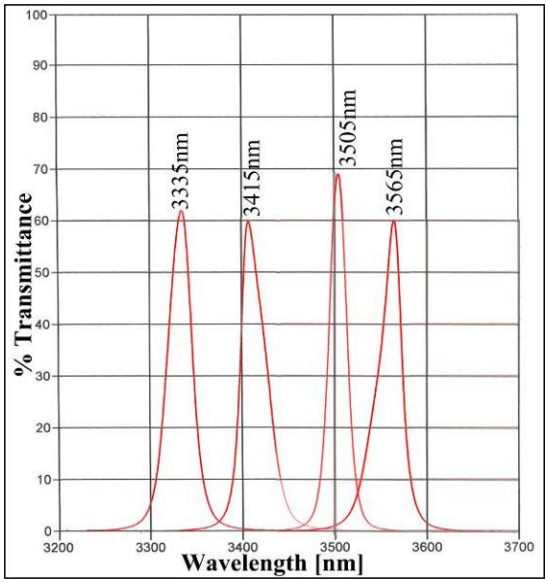

Fig. 2: Transmittance spectra of the four used NBP filters.

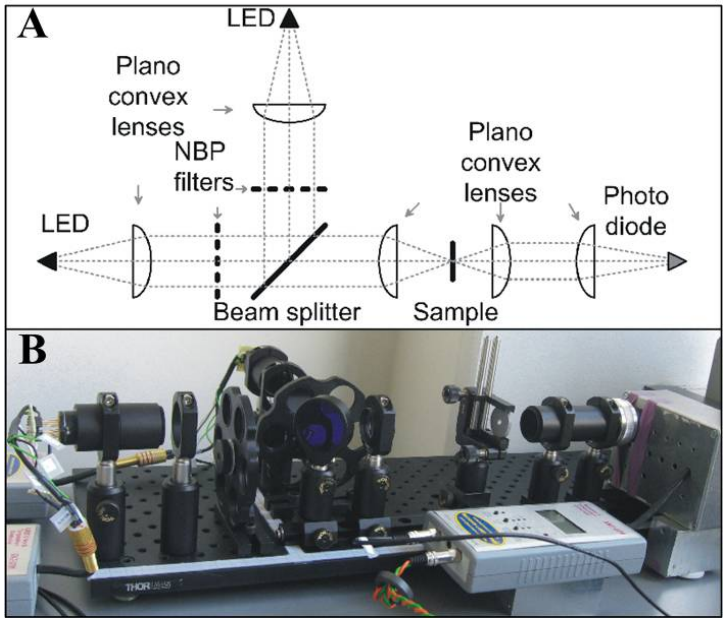

Fig. 3: (a) Sensor concept. Two LEDs operated in alternating pulse mode both emitting in a broad range so that with changeable narrow band pass filters (NBP) two wavelengths can be used (3.33 and 3.42 µm for LED1 and 3.51 and 3.57 µm for LED2). A beam-splitter is used to focus the two beams on the same spot of the sample. The photodiode (PD) is used as detector and can be operated at room temperature. (b) First realized sensor setup.

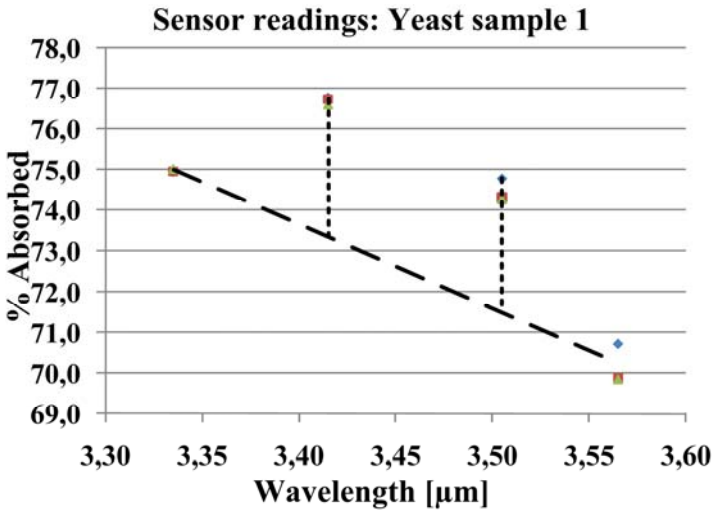

Fig. 4: IR absorbance sensor data of a yeast sample measured three times. The average measured absorbance ratio (3.51/3.42 µm) is 0.89.

The absorbance ratio of a 2 hours dried yeast sample, calculated as previously described, was 0.89. One wavelength absorbance value consists of the averaged value of 1000 measurements. Of each 8 µs LED pulse, 12 samples were recorded; due to background noise, rise and fall time the four second highest values were averaged to get one measurement value (one "% absorbed/wavelength" point shown in Fig. 4 is an averaged measurement value of 1000 times 4 sample values). The same sample measured again 24 hours later showed a lower absorbance ratio 0.64.

Discussion

The difference between the measured yeast IR absorbance ratios after 2h and 24h drying is most likely due to a higher fraction of evaporated water. A ratio of 0.65 was measured earlier of a vacuum dried yeast sample with an FTIR spectroscope. When the absorbance ratios of different samples have to be compared, constant sample preparation conditions are of importance.

Conclusions

The IR absorbance ratio (3.51/3.42 µm) measurements with a FTIR spectroscope of healthy MDCK and carcinoma A-498 and Caki-1 epithelial kidney cell lines, confirm that it is possible to discriminate between cell types by using the few wavelength concept. First sensor measurements showed detectable peaks of interest.

Outlook

The next step to test the sensor setup is to measure and compare the IR absorbance ratio of MDCK, A-498 and Caki-1.

Acknowledgements

This project is a part of a joined EU Marie Curie Research Training Network (MRTN) "On-Chip Cell Handling and Analysis" CellCheck. Project no. MRTN-CT-2006-035854.

References

[1] H.Fabian et.al.: “Diagnosing Benign and Malignant Lesions in Breast Tissue Sections by using IR-microspectroscopy”, Biophys. Acta., Vol. 1758,2006, pp. 874-882.

[2] C.P.Schultz et.al.: “Study of Chronic Lymphocytic Leukemia Cells by FT-IR Spectroscopy and Cluster Analysis”, Leukemia Research, Vol.20,1996, pp. 649-655.

Contactless Conductivity Detection in Ceramic Technology for On-Chip Electrophoresis

G. Fercher[1,2], W. Smetana[1], M. J. Vellekoop[1]

[1] Institute of Sensor and Actuator Systems, TU Wien, Austria

[2] IMA GmbH, Wiener Neustadt, Austria

A capacitively coupled contactless conductivity detector produced in Low Temperature Co-fired Ceramic (LTCC) technology for microchip capillary electrophoresis (CE) is reported in this work. Electrodes located outside the measurement channel are used to sense impedance variations caused by conductive ions. The application of LTCC in combination with contactless conductivity detection is very promising because of its high dielectric constant compared to glass or plastics. This enhances the coupling of the excitation signal into the microfluidic channel and thus results in increased detection sensitivities. Successful separations of three inorganic ions confirm the feasibility of LTCC as a material for on-chip CE when used with contactless conductivity detection.

Introduction

Capacitively coupled contactless conductivity detection is a versatile detection method for bioanalytical applications and has been widely used e.g. for on-chip capillary electrophoresis (CE) devices [1] – [5]. Small dimensions of both the detector and read-out electronics make it an attractive alternative to fluorescence- or optical absorbance-based systems since conductive compounds such as inorganic ions can be sensed without prior chemical modification. The measurement electrodes are located outside the fluidic channel, avoiding direct contact with the buffer solution. Bubble formation impeding the electrophoretic separation process does therefore not occur, increasing the life time of the device.

Low Temperature Co-fired Ceramics (LTCC) as a high-performance material for the fabrication of microfluidic devices is attaining increased attention [6] – [7]. It is based on a mixture of ceramics and a certain proportion of glass which affects physical properties such as material permittivity. In its pre-fired state, LTCC is a flexible tape that can be easily structured using stamping, cutting, embossing or laser micromachining techniques. Once fired, electroosmotic flow properties of LTCC are similar to those of glass, making this material interesting for capillary electrophoresis (CE) chips.

Thick-film pastes made from gold, silver or copper can be used to print conducting paths onto the substrate. This enables the placement of electronic circuit components in surface mount technology directly on the ceramics, minimizing the influence of noise.

LTCC-tapes are available with very high values of material permittivity as compared to plastics or glass. This enhances the measurement signal coupling into the microfluidic channel and leads to higher detection sensitivities.

This paper reports on the fabrication of a CE module with an integrated contactless conductivity detector build up entirely in LTCC technology. Successful CE separations of three inorganic ions were carried out in less than 1 minute.

Device Description

The CE module is built up by five layers of LTCC tapes (Heratape 707). Each of these layers has a thickness of 138 µm in the unfired state. Microchannels, alignment and via holes as well as liquid inlet and outlet ports were micromachined with a diode pumped NdYAG laser. Figure 1 depicts an exploded view (a) and a cross-sectional photograph (b) of the LTCC-CE module. The separation channel embedded in the device has a width of 100 µm and a total length of 125 mm. For testing purposes a dummy channel is integrated on the same device. It was not used for the experiments.

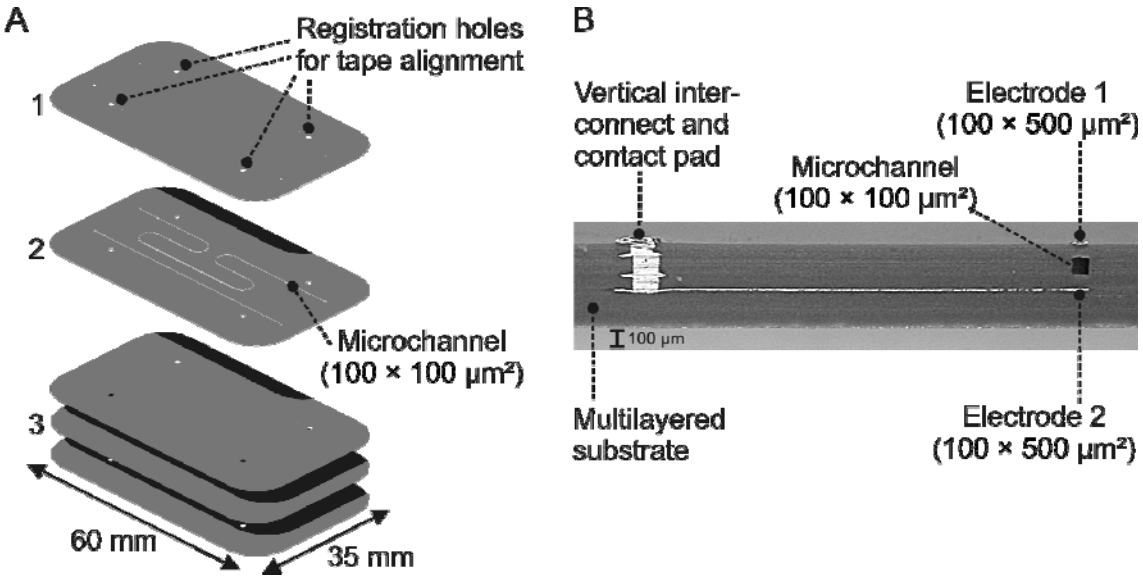

Fig. 1: Exploded view (a) and cross-sectional photograph (b) of the fabricated CE-module. (1) cover layer with electrode contact pads, fluid inlet/outlet ports and registering holes; (2) middle layer comprising separation channels; (3) three bottom layers for mechanical support.

The detection area encompasses two electrodes facing each other, located at opposite sides of the device and separated from the microchannel by a single ceramic layer. Electrodes and conductor metallization were realized by screen printing a silver conductor paste (Heraeus TC 7304A). Via holes filling was conducted by a stencil printing process using the silver paste Heraeus TC 7601. The via provides the vertical electrical connection between the buried bottom electrode and the contact pads on the top layer of the device (Fig. 1 (b)). It was placed in a distance of 3 mm from the channel in order to minimize stray capacitances. The metalized tapes were collated to a stack which was exposed to a lamination process in an isostatic press at a pressure of 100 bar and a temperature of 70 °C for 3 minutes. Firing of the laminated stack was conducted in a conventional belt furnace with a peak temperature of 850 °C and a total cycle time of 90 minutes where the dwell time at peak temperature was 15 minutes. Details and dimensions of the detector are shown in Fig. 1 (b). Inlet and outlet reservoirs are formed by gluing silicon rings on the inlet and outlet ports, which enables fluid-tight filling of the channel using syringes.

Experimental

Fluid Handling and Measurement Setup

Sample and buffer solutions were degassed for 5 minutes and filtered through 0.2 µm syringe filters to eliminate gas bubbles and particles. Micro-dispensing needles and syringes were used to fill the sample into the inlet reservoirs. Samples were electrokinetically injected into the microchannel. Between runs the microchannel was rinsed with 10 channel-volumes of run buffer to ensure reproducibility of the experiments. Platinum wires were used as high-voltage electrodes which were positioned in the inlet and outlet ports.

The optimum measurement frequency where the detector shows maximum response depends on the value of the liquid conductivity. In the case of the buffer used in the experiments (10mmol/l MES/Histidine), maximum sensitivity was found at a frequency of 2.25 MHz. A current-to-voltage converter placed directly on the CE module and connected to a lock-in amplifier (Stanford Research Systems, model SR844) was used to reduce the influence of parasitic stray capacitances on the small changes of the output signal. The data was recorded using a laptop connected to the lock-in amplifier via the IEEE-488 bus.

Results and Discussion

Successful CE separations of three different inorganic ions are depicted in Fig. 2 (a). The peak heights decrease in the order K^+>Na^+>Li^+. This is related to the different ionic conductivities; however, it is also a result of the applied electrokinetic injection procedure: Ions of higher electrophoretic mobility get loaded into the channel to a greater extend than slower ones.

The linearity of the detector is demonstrated in Fig. 2 (b). From the electropherograms the peak area of the separated samples containing potassium at concentrations from 0.2 to 2 mmol/l was extracted. The correlation coefficient of the linear fit is 99.7 %, which confirms that the measurement signal is a linear function of the liquid conductivity.

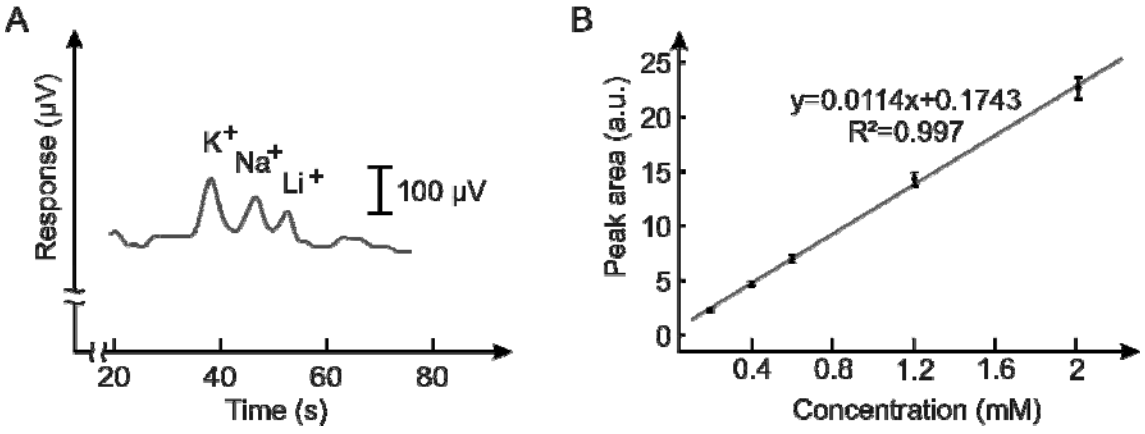

Fig. 2: Electropherograms of a mixture of inorganic cations at concentrations of 200 µmol/l (a) and linear fit of potassium samples at different concentrations (b). Separation parameters: 10 mmol/l MES/Histidine at pH 5.8; separation field strength 300 Vcm^{-1}; injection time 10 s at 50 Vcm^{-1}; effective separation length 11.5 cm.

Conclusion

In this work the integration of a contactless conductivity detector on a miniaturized CE-module fully assembled in LTCC-technology is demonstrated. The successful separations of inorganic ions are promising for the adoption of LTCC as a novel and versatile low-cost microchip material for miniaturized analytical devices.

The significant advantage of LTCC is its availability with high values of electric permittivity. Currently tapes with dielectric constants of 7 are used. It is planned to use tapes with values up to 200 to further improve detection sensitivity. In future the introduction of a double-T injector for volume-defined sample filling will be investigated to further improve the separation efficiency.

Acknowledgements

The authors would like to thank Franz Kohl and Franz Keplinger for valuable input regarding the measurement setup. Special thanks go to Heinz Homolka, Edeltraud Svasek and Peter Svasek for their support in the realization of the device. The authors are very grateful to Dr. Annette Kipka and Christina Modes (Heraeus) for the supply of the ceramic tapes. This work has been partly integrated within the EU 4M Project (Contract Number NMP2-CT-2004-500274).

References

[1] F. Laugere, G.W. Lubking, A. Berthold, J. Bastemeijer, M.J. Vellekoop: “Downscaling aspects of a conductivity detector for application in on-chip capillary electrophoresis”, *Sensors and Actuators A*, **92**, 2001, pp. 109-114.

[2] F. Laugere, R.M. Guijt, J. Bastemeijer, G. van der Steen, A. Berthold, E. Baltussen, P. Sarro, G.W.K. van Dedem, M.J. Vellekoop, A. Bossche: “On-Chip Contactless Four-Electrode Conductivity Detection for Capillary Electrophoresis Devices”, *Anal. Chem.*, **75**, 2003, pp. 306-312.

[3] J. Lichtenberg, N.F. de Rooij, E. Verpoorte: “A microchip electrophoresis system with integrated in-plane electrodes for contactless conductivity detection”, *Electrophoresis*, **23,** 2002, pp. 3769-3780.

[4] M. Pumera, J. Wang, F. Opekar, I. Jelinek, J. Feldman, H. Löwe, S. Hardt: “Contactless Conductivity Detector for Microchip Capillary Electrophoresis”, *Anal. Chem.*, **74,** 2002, pp. 1968-1971.

[5] J. Tanyanyiwa, P.C. Hauser: “High-Voltage Capacitively Coupled Contactless Conductivity Detection for Microchip Capillary Electrophoresis”, *Anal. Chem.*, **74,** 2002, pp. 6378-6382.

[6] M. Goldbach, H. Axthelm, M. Keusgen: “LTCC-based microchips for the electrochemical detection of phenolic compounds”, *Sensors and Actuators B*, **120,** 2006, pp. 346-351.

[7] C.S. Henry, M. Zhong, S.M. Lunte, M. Kim, H. Bau, J.J. Santiago: “Ceramic microchips for capillary electrophoresis-electrochemistry”, Anal. Commun., **36,** 1999, pp. 305-307.

Optofluidic Elements for On-Chip Sample Analysis

M. Rosenauer, M. J. Vellekoop

Institute of Sensor and Actuator Systems, Vienna University of Technology, Gusshausstraße 27-29, 1040 Vienna, Austria

The benefits of the integration of novel optofluidic elements, e.g., fluidic lenses and liquid-core / liquid-cladding (L2) waveguides, for on-chip optical sample analysis are discussed. Using properly designed microfluidic channels, pre-calculated flow rate ratios and transparent fluids with different refractive indices but similar viscosity novel fluidic optical elements can be created. In this contribution we present a dynamically reconfigurable fluidic lens which can focus light three-dimensionally and a L2 waveguide concept which can couple the incident laser beam in the analysis channel. The optofluidic system is fabricated on a glass substrate in a photosensitive polymer by fast laser micro-stereolithography.

Introduction

The combination of optics and microfluidics generates a new field of research called optofluidics. By using transparent fluids with different refractive indices in the laminar flow regime of the microchannels novel functionalities of optical elements can be created. Changing the flow condition in the channel by manipulating the flow rates or simply replacing the fluids alters optical properties like shape, focal length and guiding modes which is almost impossible to obtain with the fabricated solid equivalent. When using miscible fluids a smooth interface with a defined refractive index gradient due to diffusive mixing parameters (Reynolds number, diffusion coefficient) is created. Based on these conditions multiple sensor applications with increased optical functionality can be found [1].

Optofluidic systems can be divided into three main categories: Solid/Liquid-Devices – structured solid chip and pressure driven liquid define the optical properties, Liquid/Liquid-Devices – optical functionality is created only by manipulation of certain liquids, Colloidal/Liquid – Dissolved particles in a buffer solution provide the desired optical quality. In this contribution the focus lies on liquid/liquid flow systems generating stable adjustable optofluidic components.

In conventional optical miniaturized sensor systems the required measurement sensitivity is achieved by applying extensive and costly source and detection instruments. Fluidic elements like lenses, mirrors and waveguides can be integrated to decrease costs, simplify the setup and enhance the functionality. As examples electrowetting lenses, liquid crystal displays and oil immersion microscopes should be mentioned.

The integration of fluidic sensor systems, e.g., to measure the fluorescent characteristics of an analyte, often needs the implementation of optical elements (lenses, waveguides) to ensure a well-defined reconfigurable light propagation. In this contribution we present the design, fabrication and measurement results of a novel hydrodynamically adjustable lens chip for 3D light focusing and a liquid-core-cladding waveguide concept fabricated by rapid prototyping.

Device Description

We present two chip designs for the integration of optofluidic components fabricated by single-layer micro-stereolithographic prototyping in a transparent photoresin to improve the optical performance of liquid-based analysis systems in terms of excitation light guiding and focusing. 2D light focusing fluidic lenses have been published [2], [3]. Our novel chip design is illustrated in Fig. 1, left. We show how standard fluid manipulation (altering fluidic inlet flow rates) enables the formation of a fluidic lens with adjustable three-dimensional light focusing ability.

The biconvex fluidic lens shape is generated in two steps. The center of the microchannel has the highest flow velocity because of the parabolic velocity profile due to the laminar flow regime (Re ≤ 1). By using the centrifugal effect at both 90° bends of the divided channels the interface between lens body and cladding fluid arches from a straight to a convex form [3] (Fig. 1, right). After bringing the two streams together a single biconvex form in the vertical channel direction originates. The following expansion chamber causes a deceleration of the stream developing a biconvex shape of the microfluidic lens in the horizontal direction. In this light focusing area we achieve the formation of a 3D curvature adjustable convex lens by choosing fluids with different refractive indices (lens body fluid = $CaCl_2$ 5mol/l, cladding fluid = DI-water).

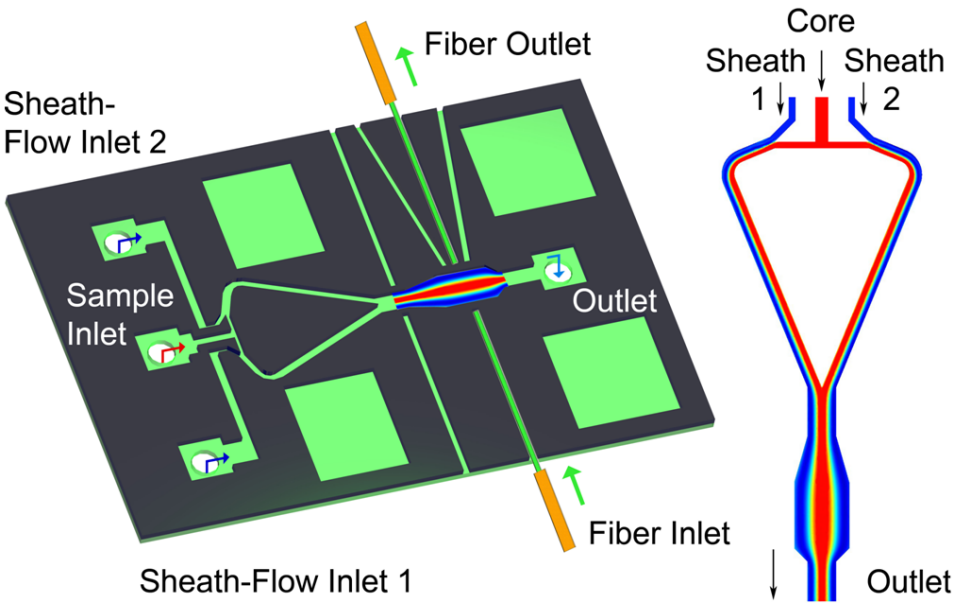

Fig. 1: Left: Schematic design of the optofluidic lens chip with three fluidic inlets and one outlet. For multi-angle light intensity measurements trenches were designed for the insertion of glass fibers. Right: Top view of the computational fluid dynamics (CFD) simulation (COMSOL Multiphysics).

The second design, a liquid-core / liquid-cladding (L2) waveguide chip, is created by using a core fluid with a higher refractive index than the cladding fluid and the microfluidic chip material (PDMS, glass substrate). The core fluid is introduced over a core inlet and bordered by the cladding fluid with the hydrodynamically focusing principle [4]. Under these conditions total internal reflection between the fluids occurs. This is achieved by using Benzothiazole as core fluid and DI-water as cladding fluid. The L2 waveguide allows laser light guidance on the chip for illumination purposes (sample excitation for fluorescence detection or absorption measurements) in a sample analysis channel. Therefore, it is not necessary to fabricate optical smooth microchannel walls in order to reduce manufacturing efforts significantly. With additional fluidic sideports it

is also possible to direct the light path continuously by shifting the fluids in the channel. The incident laser light is coupled in the L2 waveguide with an inserted glass fiber.

Device Fabrication

Long production durations and expensive fabrication steps of conventional techniques like silicon micromachining make rapid prototyping schemes attractive for various research areas. To introduce novel functionalities on a chip it is often helpful that each innovation is tested independently to prove the underlying concept and measure specific process parameters uninfluenced. As proposed in [5] the optofluidic chips were fabricated by micro-stereolithographic production (Fig. 2, left) without masking and complex developing steps. Based on a glass substrate the microchannel structure was manufactured in a transparent photoresin (Renshape SL-7570) to obtain low light absorption in the visible range. After this one-layer procedure the fluidic connection holes were drilled through the substrate. The written structure was then capped with a thin layer of PDMS (Polydimethylsiloxan). To simplify the insertion of the glass fibers for measurements the structured photoresin height is 170 µm.

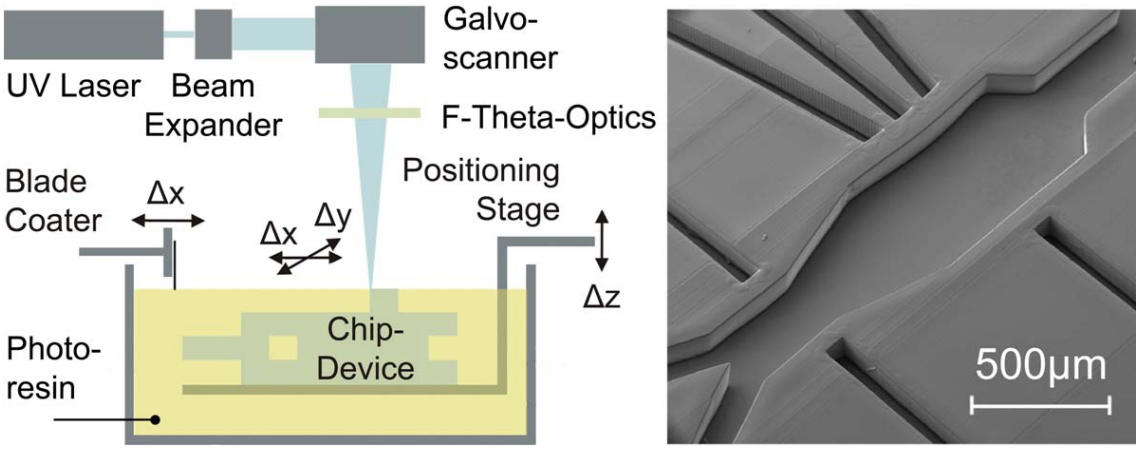

Fig. 2: Left: Functional diagram of the Micro-Stereolithography setup (MIPRO) for the fabrication of 3D fluidic sensor prototypes. The fluidic photoresin is polymerized by a deflected UV laser beam. Right: SEM image of the flow expansion chamber with multiple fiber trenches to measure the performance of the fluidic lens.

Results and Discussion

For reproducible stable fluid conditions (flow rates) the fabricated optical microfluidic devices are attached to a fluidic supply unit (kdScientific syringe pumps). The chips are mounted on a custom made plastic holder with supply tubes. As optical setup we used a free-space solid-state laser (λ = 532 nm, P_{CW} = 5 mW) coupled to a glass fiber (50 / 150 µm). The fiber end was cleaved and inserted into the fiber trench. A fiber-coupled Si-photodiode (FC-PC / pigtailed-ending) was applied to measure the focused light intensity. After calibration of the sensor we have measured the focused light intensity propagating through the optofluidic lens (Fig. 3, left). The results show that we are able to focus light three-dimensionally in the channel and that an adjustment of the flow rates alters the lens shape, which adequately confirms the CFD simulations. The occurring difference between measurement and simulation results arises from a variation of the channel dimensions caused by the prototyping resolution and from the non-continuous flow rates of the syringe pumps used for the measurements. Figure 3, right

depicts the design of the waveguide structure for the illumination of the analysis channel. The graph demonstrates the refractive index gradient due to the diffusive mixing over the length of the microchannel. Further research is planned to integrate both designs and advantages into one optofluidic system.

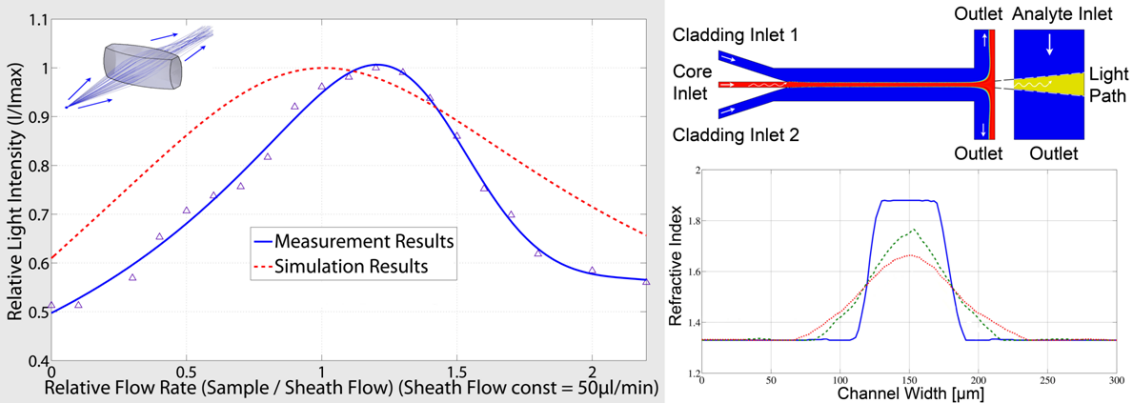

Fig. 3: Left: Normalized light intensity measurements and ray-tracing simulations (ZEMAX EE). A light focusing optimum in transversal direction is reached at the following flow rates; core = 60 µl/min, cladding$_{1,2}$ = 50 µl/min. Right: Schematic design of the waveguide chip directing the coupled light from the core inlet to fluidic analysis channel. The refractive index step decreases due to diffusive mixing as a function of the distance from the inlet.

Conclusion

We have developed two novel microfluidic devices with light focusing and guiding characteristics fabricated by fast high quality micro-stereolithography. The first fluid channel design introduces a three-dimensional microlens, the second a liquid-core-cladding waveguide which both enables new areas of microfluidic optical applications.

Acknowledgements

For the technical support we thank M. Spitzbart (Department of Micro- and Nanosystems, University of Applied Sciences Wr. Neustadt), E. Svasek and P. Svasek (ISAS Technology Lab and ZMNS, Center of Micro- and Nanostructures, Vienna University of Technology). The SEM image analysis was carried out using facilities at the University Service Centre for Transmission Electron Microscopy (USTEM, Vienna University of Technology). This work was partially supported by the Austrian Research Promotion Agency (FFG) Project No. 811442.

References

[1] D. Psaltis, S. R. Quake, C. Yang: “Developing optofluidic technology through the fusion of microfluidics and optics”, Nature, Vol. 442, 2006, pp. 381 – 386.

[2] S. K. Y. Tang, C. A. Stan, G. M. Whitesides: “Dynamically reconfigurable liquid-core liquid-cladding lens in a microfluidic channel”, Lab Chip, Vol. 8, 2008, pp. 395 – 401.

[3] X. Mao, J. R. Waldeisen, B. K. Juluri, T. J. Huang: “Hydrodynamically tunable optofluidic cylindrical microlens”, Lab Chip, Vol. 7, 2007, pp. 1303 – 1308.

[4] D. B. Wolfe et al.: “Dynamic control of liquid-core liquid-cladding optical waveguides”, PNAS, Vol. 101, No. 34, 2004, pp. 12434 – 12438

[5] M. Rosenauer, M. Spitzbart, S. Zoppel, M. J. Vellekoop: “Ultra Rapid High Quality Prototyping for Optical Microfluidic Analysis Devices”, Proc. Eurosensors XXII, 2008, pp. 785 – 788.

Novel Design and Signal Transduction Concepts of Micromachined Flow Sensors

A. Talić[1], S. Ćerimović[1], F. Kohl[1], F. Keplinger[2], A. Jachimowicz[2]

[1] Research Unit for Integrated Sensor Systems, Austrian Academy of Sciences, A-2700 Wr. Neustadt, Austria

[2] Institute of Sensor and Actuator Systems, Vienna University of Technology, A-1040 Vienna, Austria

In this work we investigate a novel design approach and signal transduction concepts for micromachined calorimetric flow sensors. Maintaining a constant average excess temperature of the membrane by means of a simple two-state electronic controller, a pulse modulated actuation signal is obtained. The sensitivity of the output signal can be influenced by altering the amplitude of the heating pulse. The proposed novel sensor design offers three different operating modes. Beside the conventional calorimetric transduction, such sensors are also operable in a mixed calorimetric-anemometric mode featuring low power consumption, high flow sensitivity, and an unambiguous transduction characteristic over a wide flow range.

Introduction

Commonly used micromachined calorimetric flow sensors feature heat source(s) and spatially separated temperature sensors, both embedded in a thin membrane [1]. These sensors exploit the flow dependent heat transfer altering the temperature distribution near the heater. Operating the flow sensor at a constant heating voltage, tantamount to a constant heating power, a high sensitivity is feasible only within a limited flow range. Due to efficient convective cooling at higher flow rates the output characteristic becomes ambiguous. For a wider measurement range, a constant temperature difference between the membrane and the fluid is necessary. This operational mode can be achieved using an electronic controller. Applying a standard PI-controller results in an unambiguous characteristic with moderate sensitivity at higher flow rates. In order to achieve better sensitivity, we investigated a novel signal transduction concept for the existing sensor layout as well as an improved sensor design.

Common Sensor Design

Figure 1 illustrates the membrane arrangement of the utilized flow sensor. Two thermistors (MT1, MT2) measure the local temperature at a position upstream and downstream of the heat source (thin-film heating resistor H). Without the flow, the generated temperature profile inside the membrane is symmetrical and both thermistors measure the same value. The convective heat transfer induced by the media flowing across the sensor surface disturbs the thermal symmetry. This change can be converted into an output voltage and evaluated for the determination of essential flow parameters such as flow velocity or mass flow.

The fluid temperature, which is typically close to the substrate temperature, can be measured with two additional thermistors arranged at the rim of the silicon chip (not shown in Fig. 1). The membrane consists of a SiO_2-Si_3N_4-SiN_x-sandwich with an overall thickness of 1.6 µm. The chip dimensions are 2 x 4 mm² (membrane area:

0.5 x 1 mm²). Further details of the technology and key specifications of such sensors can be found in [2], [3].

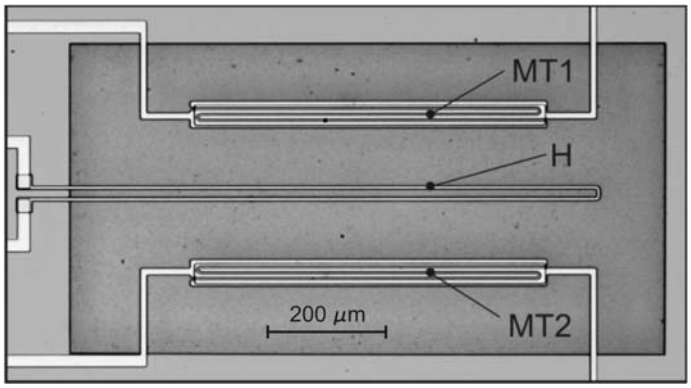

Fig. 1: Sensor layout with two temperature sensors (MT1, MT2) and a heater (H).

In the constant temperature excess mode, a constant difference between the temperature mean of the two membrane thermistors and the temperature mean of both substrate thermistors is maintained using an electronic controller. Instead of the commonly applied analogue controller we investigated the application of a two-state controller. For the design and optimization of the control loop a comprehensive SPICE model of the sensor's thermal system capable to fully cover its static and dynamic behavior was developed. This approach has proved to be a convenient method to investigate the interaction of the sensor and its evaluation/controlling circuit.

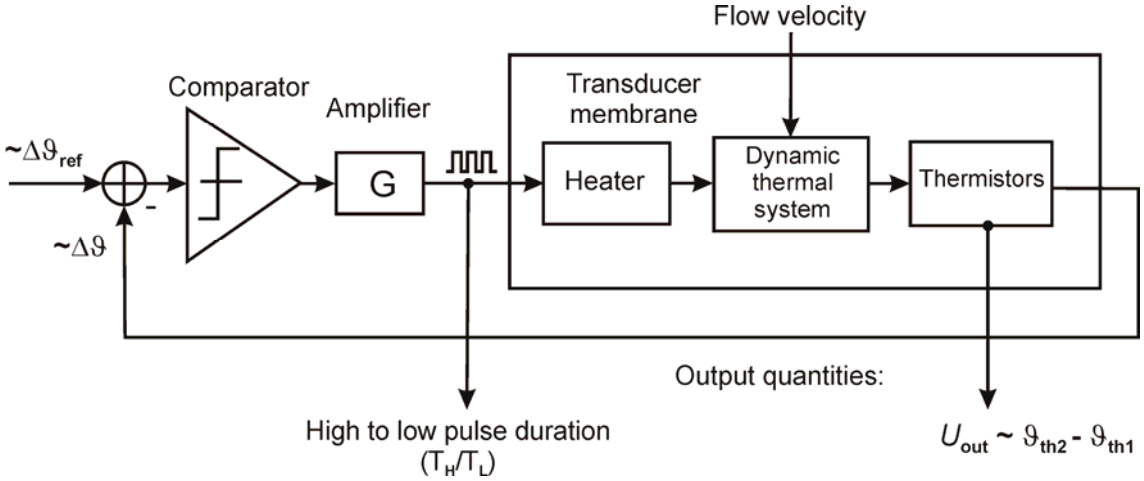

Fig. 2: Scheme of the novel operational mode using two-state closed loop controller which keeps the average excess temperature ($\Delta\vartheta$) of the membrane constant.

Implementation of a Two-State Controller

Figure 2 shows the scheme of the novel sensor operational mode based on a comparator operating in a negative-feedback closed-loop configuration. A constant bias of 0.5 V is applied to all germanium thermistors and each thermistor current is converted into a temperature-proportional signal by means of a current-to-voltage converter. The difference between the mean membrane temperature and the mean bulk temperature

is compared with the equivalent of the excess temperature set point. The two-state controller establishes a train of voltage pulses at the heater. The pulse duration and repetition rate are determined by the selected amplitude and the dynamic characteristics of the thermal system, which in turn depend on flow velocity [4].

This approach offers the ratio of high to low pulse duration (T_H/T_L) as an output quantity in addition to the temperature difference signal (U_{out}). The basic properties of this flow dependent oscillator have been successfully modeled using PSpice. Related measurement results are depicted in Fig. 3 (left). The sensor is flush mounted into the wall of a rectangular flow channel (cross section 1.2 x 0.5 mm²). Due to convective cooling, the pulse duration increases and the pulse gap becomes smaller with increasing flow velocity. On the other hand, reducing the amplitude of the heating pulses at constant velocity evokes the same effect. In order to keep the average excess temperature ($\Delta\vartheta$) of the membrane constant, the controller must increase the average heating power and hence the ratio of high to low pulse duration (T_H/T_L) increases too. Thus, by altering the amplitude of the heating pulses one can influence the slope of the output characteristic in order to achieve better sensitivity.

In addition to the ratio of high to low pulse duration (T_H/T_L), the temperature difference signal (U_{out}) can also be used. For low flow velocities, this signal provides the highest sensitivity whereas the ratio T_H/T_L becomes the preferable output quantity at higher flow rates (Fig. 3, right).

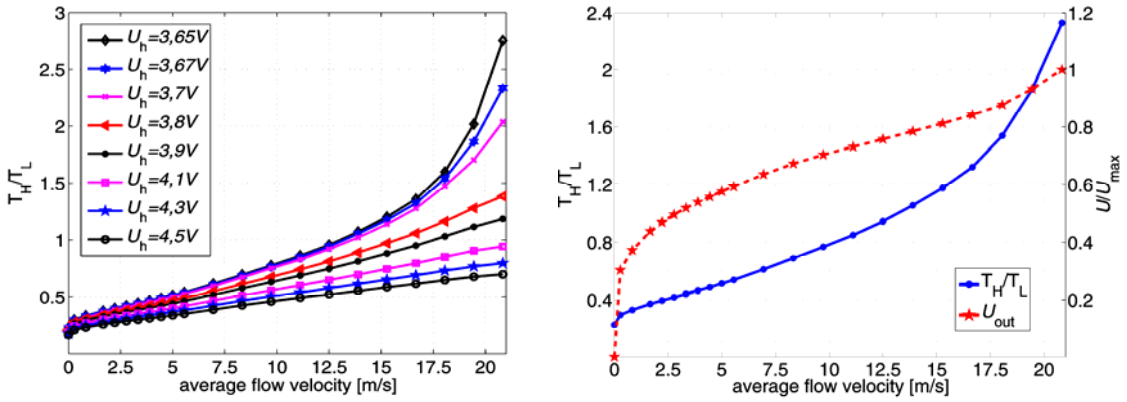

Fig. 3: Measured output characteristic for different amplitudes of the heating pulse (U_h). The ratio T_H/T_L serves as output signal. The average excess temperature amounts $\Delta\vartheta_{ref}$ ~ 5 °C (left). The comparison of two output quantities in case of an amplitude of heating voltage U_h = 3.67 V (right).

Novel Design Approach

A novel sensor design approach was first investigated by means of finite element simulations (COMSOL). This FE analysis is based on the schematic cross section indicated in Fig. 4 (left). A two dimensional model seems reasonable since all thin-film components on the membrane exhibit a large extension perpendicular to the flow direction. Two pairs of high-resolution thermistors are placed symmetrically to a thin-film heater on the sensor membrane. Additional substrate thermistors (ST) measure the fluid temperature. The air flow channel above the senor membrane is 1 mm high with a parabolic flow profile [5]. This novel design offers three different operating modes.

The first operating mode features the thin-film chromium resistor as a heat source and the pair of inner or, alternatively, outer thermistors as temperature sensors. The simulated output characteristic for constant heater voltage is depicted in Fig. 5 (left). For lower flow velocities, an excellent sensitivity is found. For higher velocities, however, the output characteristic saturates or it even becomes ambiguous. To solve this problem the heater voltage must be controlled to compensate for convective heat transfer, as described in the first paragraph. In this case the two substrate thermistors provide reference values of the fluid temperature.

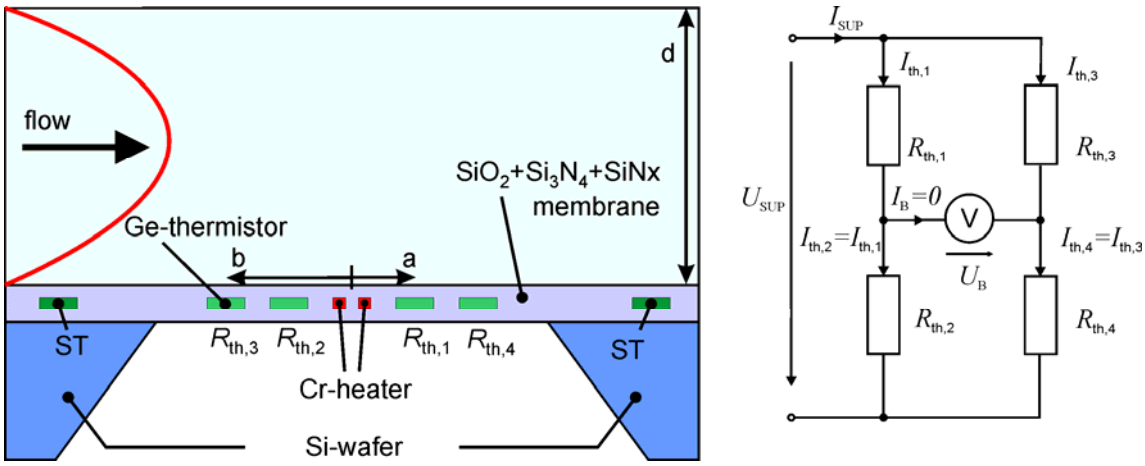

Fig. 4: Schematic cross section of the novel flow sensor design comprising four membrane thermistors, which can be connected to form a Wheatstone bridge.

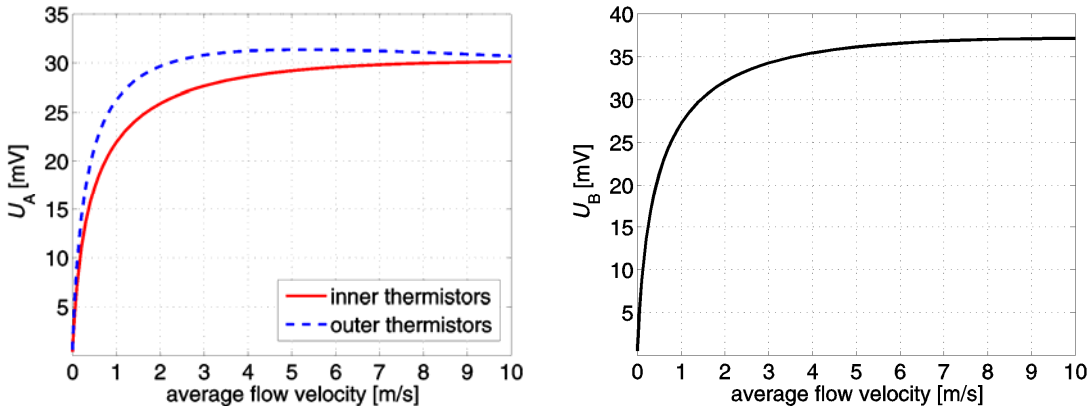

Fig. 5: Simulated output characteristics for the first (left) and second operating mode (right). In the first case, the output signal is proportional to the temperature difference of the membrane thermistor pair. In the second case, the voltage across the bridge U_B is used as an output quantity.

In the second operating mode the four membrane thermistors are connected to form a Wheatstone bridge (Fig. 4, right). The chromium resistor remains as the heat source. The simulated output characteristic is similar with the previous one (Fig. 5, right). The bridge is supplied with low voltage (1 V) in order to reduce the self-heating effect of the thermistors. The main advantage of this mode is that the Wheatstone bridge can be easily read-out, e.g., with a high-impedance galvanometer, without any need for complicated subsequent evaluation circuits. Moreover the calculations showed that this

arrangement is insensitive to ambient temperature changes. Thus, the second mode does not need pre-calibration with respect to fluid and ambient temperatures.

Finally, the third operating mode (mixed calorimetric-anemometric mode) utilizes the self-heating effect of the membrane thermistors as a heat source. The chromium heater is switched off. In order to avoid the self-destruction of the thermistors due to their NTC characteristics the bridge is supplied with a constant current I_{SUP}= 50 µA, rather than with a constant voltage as it was the case in the second mode. The bridge voltage U_B as well as the voltage at the bridge supply terminals U_{SUP} depend on the thermistor resistance values and hence on the flow velocity

$$U_B = I_{SUP}\frac{R_{th2}R_{th3} - R_{th1}R_{th4}}{R_{th1}+R_{th2}+R_{th3}+R_{th4}},\quad U_{SUP} = I_{SUP}\frac{(R_{th1}+R_{th2})(R_{th3}+R_{th4})}{R_{th1}+R_{th2}+R_{th3}+R_{th4}}. \tag{1}$$

The simulated output characteristics for both quantities are shown in Fig. 6. Evaluating the bridge voltage, an excellent sensitivity for flow velocities below 2 m/s is found. However, for higher velocities, the output characteristic becomes ambiguous as in the previous modes. Therefore the use of U_{SUP} as an output quantity is desired, resulting in a wider measurement range but moderate sensitivity for lower flow velocities.

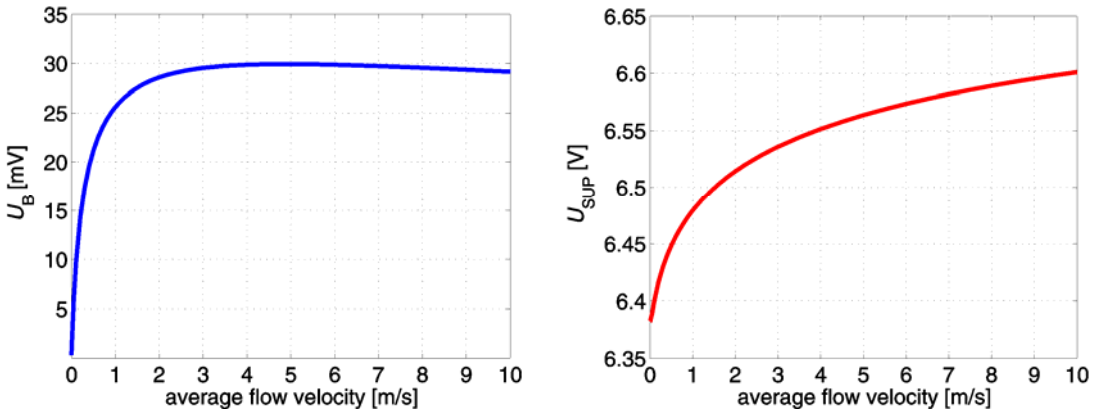

Fig. 6: Simulated output characteristics of the flow sensor using the bridge voltage U_B (left) and the voltage at the bridge supply terminals U_{SUP} (right) as an output quantity.

The power consumption in the first two modes amounts to approximately 3 mW, mainly dissipated in a chromium heater. In the third mode, however, the rated supply current limits the power consumption of all bridge thermistors to only ~ 0.3 mW. Thus, the third mode combines very low power consumption with high flow sensitivity or an unambiguous transduction characteristic.

Conclusion

We investigated novel design ideas and signal transduction concepts for micromachined calorimetric flow sensors. Maintaining a constant average excess membrane temperature by means of a simple two-state electronic controller, a pulse modulated actuation signal is obtained. This approach offers the ratio of high to low pulse duration as an output quantity in addition to the temperature difference signal. The sensitivity of the output signal can be optimized for specific applications by altering the amplitude of the heating pulse.

The proposed novel sensor design offers three different operating modes. Comprehensive finite element analyses revealed that beside the conventional calorimetric transduction such sensors are also operable in a mixed calorimetric-anemometric mode. Based on the self heating effect of the employed high resolution thermistors, this operational mode combines extremely low power consumption with high flow sensitivity or, alternatively, an unambiguous transduction characteristic over a wide flow range.

Acknowledgements

We gratefully acknowledge partial financial support by the Austrian Science Fund FWF.

References

[1] N. Sabaté, J. Santander, L. Fonseca, I. Gràcia, C. Cané: “Multirange silicon micromachined flow sensor”, Sensors and Actuators A. Vol. 110, 2004, pp 282–288.

[2] A. Glaninger, A. Jachimowicz, F. Kohl, R. Chabicovsky, G. Urban: “Wide range semiconductor flow sensors”, Sensors and Actuators A, Vol. 85, 2000, pp 139–146.

[3] F. Kohl, R. Fasching, F. Keplinger, R. Chabicovsky, A. Jachimowicz, G. Urban: “Development of miniaturized semiconductor flow sensors”, Measurement, Vol. 33, 2003, pp 109–119.

[4] S. Ćerimović, A. Talić, R. Beigelbeck, F. Kohl, J. Schalko, A. Jachimowicz: “Novel Flow Sensors Based on a Two-State Controller Scheme”. In Proceedings of the 7th IEEE Conference on Sensors, Lecce, Italy, October 2008, pp. 1163–1166.

[5] H. Schlichting, K. Gersten: “Grenzschicht-Theorie”, Springer Press (Berlin, Heidelberg, New York), 1997, pp 110-111.

ISBN: 978-3-901578-20-5